NANOCOMPOSITES OF SINGLE-WALLED CARBON NANOTUBES

by

SHIUNCHIN CHRIS WANG

A dissertation submitted to the Graduate Faculty in Chemistry in partial fulfillment of the requirements for the degree of Doctor of Philosophy, The City University of New York

2007

UMI Number: 3287142

ProQuest Information and Learning Company
300 North Zeeb Road
P.O. Box 1346
Ann Arbor, MI 48106-1346

This manuscript has been read and accepted for the
Graduate Faculty in Chemistry in satisfaction of the
dissertation requirement for the degree of Doctor of Philosophy.

Daniel L. Akins

Date — Chair of Examining Committee

Gerald W. Koeppl

Date — Executive Officer

John R. Lombardi

Hiroshi Matsui

Glen R. Kowach
Supervisory Committee

THE CITY UNIVERSITY OF NEW YORK

Abstract

NANOCOMPOSITES OF SINGLE-WALLED CARBON NANOTUBES

by

Shiunchin Chris Wang

Adviser: Professor Daniel L. Akins

Single-walled carbon nanotubes (SWNTs) have marshaled in a phenomenal era of nanoscience and nanotechnology since their discovery in 1993. Synthetic approach in general, results in a range of undesired products whose removal represents a fundamental problem for device development. The present dissertation focuses on three sub-projects which contain three categories of chemicals: SWNTs, surfactants/polymer, and nanoparticles. The first sub-project is designed to surmount the insolubility of SWNTs. It is the best way for the formation of SWNTs composites. Therefore, resolving the solubilization of SWNTs is the primary concentration in my project. Surfactants and polymers, as dispersion agents, were used to solubilize SWNTs. The selection for these solubilization agents were focus on potential biological applications. Therefore, an anionic surfactant, sodium bis(2-ethylhexyl) sulfosuccinate (Aerosol OT or AOT), and a polymeric chitosan were used as a dispersing agent to solubilize SWNTs. Sonication were the mechanism to enhance the solubility of SWNTs in dispersing solution, and centrifugation can be used to obtain individual or small bundled (2-5 tubes) nanotubes. In this study, AOT showed special protection to prevent the breakdown of the tubes through

sonication. Therefore, it was used for the investigation in field-effect transistor devices using AC dieletorphoretic alignment. The second subproject was designed to synthesis controllable nanoparticle sizes, especially focusing on quantum dots (QDs). Nanoparticles were prepared for the composite with SWNTs. The microemulsion system was used to encapsulate nanoparticles with desired sizes, and the AOT reverse micelles, water-in-oil or w/o, was designed to form a microemulsion system. It produced sizable quantum dots. The last subproject and the ultimate goal were to form composites of SWNTs with varieties of nanoparticles and polymers. Different nanoparticles (e.g., CdS, ZnS) were used, and polymeric poly-L-lysine was used for composite also. Probing the properties of SWNTs nanocomposites is a necessity for future developments of carbon nanotubes.

Preface

Carbon nanotubes (CNTs) were one of the new nanotechnology materials since 1991. Evolution of CNTs can be separated into a few stages from the investigation of CNTs properties, searching for better protocols, to the production of CNTs, functionalization of CNTs to interact with other materials, and leading toward the development of applications which is on-going.

CNTs are carbon based materials and have many extraordinary properties that will be explained in Chapter 1. The optical spectroscopes, UV-Vis-NIR and Raman, are introduced in Chapter 2. They are the first step to investigating the electronic properties of SWNTs. Different mechanical setups can be used to synthesize CNTs; these include arc discharge, laser ablation, high pressure carbon monoxide conversion (HiPco), and chemical vapor deposition (CVD). Chapter 3 briefly introduces the different methods for growing SWNTs, and the experimental data of CVD grown CNTs are presented. SWNTs are bundled and tangled together and insoluble in most solvents after synthesis. To surmount this insolubility, Chapter 4 introduces many different methods to improve and overcome the insolubility of SWNTs. Acid purification can remove amorphous carbon and improve solubility; it can also be used to functionalize sidewalls of tubes with the added benefit of producing covalent interactions with other materials. However, purified SWNTs can be damaged severely through harsh acid treatment, and acid purified SWNTs will alter the intrinsic electronic properties of tubes. Therefore, dispersion of SWNTs is a better method to improve its solubility. SWNTs dispersions were investigated in polymer (Chitosan) and surfactant (Aerosol OT) solutions here.

Chapter 5 introduces a variety of nanoparticles (NPs). The purpose of this non-carbon nanotubes related chapter is to search for materials for SWNTs nanocomposites discussed in Chapter 6. Nanoparticles can have many attractive potential for biomedical applications. Consequently, different methods of synthesizing NPs are introduced in Chapter 5. An ultimate goal is to achieve SWNT composites. Many CNT composites have the potential for applications development; these are briefly introduced in Chapter 6.

The setup of this dissertation is based on the evolution of single-walled carbon nanotubes (SWNTs). Experiments were conducted from producing carbon nanotubes to SWNTs nanocomposites. Every chapter is relevant to the next chapter, but they can also stand alone as individual chapters/sections.

Acknowledgments

Almost all of our major attainments require the assistance of others. This is especially true, in my case, for the acquisition of a Ph.D. degree.

My gratitude goes to my mentor who not only supported me financially, but also gave me the freedom to define my project. He also made it possible for me to attend important conferences; he was especially helpful in pushing me to improve my presentation skills, by patiently correcting my misuse of vocabulary and malapropisms. I (王薰卿) am also fortunate to have had great colleagues who were willing to share their research experiences with me. I would like to acknowledge Dr. Jean-Mary Fleumingue (a recent graduate from my laboratory) who taught me on my first day of this journey about how to maintain a clean and effective work environment; he continues to encourage me and is aiding me in my search for employment. I further acknowledge Dr. Xiaoming Zhang and Dr. Haiquan Guo (both former students in my laboratory) who aided me in expanding my efforts to include approaches that they developed. I acknowledge Dr. Hui Yang, a visiting professor in my laboratory from the Shanghai Institute of Microsystem and Information Technology of Chinese Academy of Science in China, who gave extensive advice to me in developing my first project; and also patiently shared his career experiences with me. I want to also thank two other associates in my group, Dr. Huijun Jiang (a visiting postdoctoral associate) and Ms. Diane Beckford (program coordinator of the Center in which I worked). Both of these latter two individuals cheered me up as I struggled with putting my dissertation together.

Thanks also are extended to my committee members, Dr. John Lombardi (The City College (CCNY)), Dr. Hiroshi Matsui (Hunter College), and Dr. Glen Kowach (CCNY).

Furthermore, I would like to thank several research collaborators who facilitated my efforts. These include Dr. Chenghui Lui (CCNY), Dr. John Berriman (New York Structural Biology Center (NYSBC)), Dr. Michael Huang (New Jersey Institute of Technology (NJIT)), and Dr. Xueyan Zhang (NJIT), for providing access to their instrumentation. Above all, I would like to give special thanks to Dr. Sarbajit Banerjit (Assistant Prof. at SUNY Buffalo) for providing invaluable proofreading and concept development assistance in regards to both manuscripts as well as my dissertation.

As regards the funding agencies, I wish to thank the National Science Foundation (NSF) for support under its Integrative Graduate Education and Research Traineeship (IGERT, 2002-2006) that my mentor received; the Department of Defense (DoD) for support to my mentor under its Science, Mathematics and Engineering Education (SMEE, 2006-2007) Graduate Fellowship award; and for support under a subcontract from the Columbia University Nanoscale Science and Engineering Center (NSEC) project funded by the NSF.

Finally, I would like to acknowledge how important family support has been for me. Indeed, my family is the source of my strength and has sustained and propelled me toward completion of my doctorate. My mother, Judy 楊綉目, is my inspirational source. Whenever she sees me getting tired of my work, she cheers me through humor. She is also a philosopher who always tells me to think positively and laugh at my problems. My father always provided me with many research ideas. He was the one who told me that I

should concentrate in nanotechnology before I got into the Ph.D. program. He was a true scientist, and he gave me suggestions as to specific chemical to use in my project (indeed, the use of Chitosan as a wrapping polymer was his idea). Unfortunately, I lost my best teacher and advisor, and the world a true scientist on Nov 20, 2006. I want to thank my two younger brothers (Solomon 王禎祥 and Abraham 王禎邦) who provided me strength during the tough times following my father's passing. They are my spiritual support, without them I would not be able to successfully attain what I know my family wants for me. I also want to give gratitude to my best friend, Julie (a molecular biologist), who proofread all my writings.

I am a scientist and also believe in God. Thanks to my church members of Taiwan Union Christian Church in New York (TUCCNY) who prayed for me. Above all, I give praise and thanks to God for pointing the way.

In memory of

My father, 王世宏 Sehong Wang

(a.k.a. Seiko Oong)

Table of Contents

List of Tables

List of Figures

1
Introduction

In the twenty-first century, carbon nanotubes (CNTs) are promising nanomaterials for a wide range of applications and have attracted much attention due to their unique properties. Carbon nanotubes exist in single- or multi- walled structures. CNTs have a fundamental backbone structure, but exhibit considerable complexity in their electronic and mechanical properties. In the last decade, CNTs have generated a new field of research in materials science focusing especially on "single-walled" carbon nanotubes (SWNTs). The availability of state-of-the-art instrumentations has made it possible to extensively characterize CNTs. In this Chapter, the history and development of CNTs are described to provide a background for the work discussed in subsequent chapters. The following section is a discussion about carbon in different electronic configurations and their different structures. The extraordinary electronic properties of carbon nanotubes are explained in detail. The last section of this chapter introduced ideas related to electronic and mechanical properties of CNT.

1.1 History and Development of SWNTs

Multi-walled carbon nanotubes (MWNTs) were first discovered by Sumio Iijima in 1991 [1], while conducting a project involving the arc-discharge evaporation synthesis of fullerenes (C_{60}) at the NEC Laboratories in Japan. In fact, however, carbon nanotubes had been synthesized a few decades before in the 1950s, as indicated in Figure 1-1.

Graphite filaments (later known as carbon fibers) were discovered in 1960 by Roger Bacon [2]; Bacon observed straight filaments while studying various carbon structures. In the absence of sophisticated instruments to characterize the products, Bacon was unable to properly describe this new configuration of carbons as hollow tubes. Carbon fibers with a similar structure were also reported by Morinobu Endo at Shinshu University, Japan, in 1976 [3]. Endo was using a mixture of benzene and hydrogen to grow carbon filaments on substrate surfaces using transition metal catalysts to enhance the dissociation of gas mixture; the diameters of the obtained carbon fibers ranged from 2-100 nm. Despite the fact that high-resolution electron microscope (HREM) had been acquired by S. Iijima in 1971, Endo was unable to identify the carbon fibers as multi-walled carbon nanotubes, even after using a Philips EM300 high resolution electron microscope (HREM) to characterize the products. MWNTs did not generate much attention until the evolution of the high-resolution electron microscopy (HREM) into a more advanced technique called high resolution transmission electron microscope (HRTEM). In 1993, single-walled carbon nanotubes were discovered by S. Iijima [4] at NEC in Japan and Bethune et al. [5] at the IBM Research Division of Almaden Laboratory located in San Jose, California, USA. Both groups used the arc discharge technique to synthesize SWNTs; details of which will be described in Chapter 3. SWNTs have turned out to be especially important for fundamental and theoretical studies. The timeline of development for carbon nanotubes is shown in Figure 1-1. Due to their unique structures (zigzag, armchair and chiral configurations), small sizes (0.7 nm to about 10 nm in diameter), low density, high stiffness, high strength (the outer-most shell of MWNTs is approximately 100 times stronger than aluminum), and excellent electronic, mechanical, optical, and chemical

properties, CNTs have been employed in many research fields and are promising candidates for a wide range of applications. Possible and realized applications include material reinforcement (NASA space applications), field emission panel displays (television screens by Samsung and NEC), chemical sensors, drug delivery (chemotherapy), biomedical devices (bone reconstruction), and nanoelectronics (circuitry development). In the development of CNTs applications, it is essential to investigate the electronic, optical, and mechanical properties of CNTs as described in the following sections.

1.2 Allotropes of Carbon

A single-walled carbon nanotube can be treated as a rolled-up graphene sheet. In order to understand properties of SWNTs, it is important to understand the different bonding structures. Carbon is one of the most abundant elements on earth. In the periodic table, carbon is the sixth element (atomic number: 6), and is in group IVB; a nonmetal. Every carbon atom possesses six electrons and the electronic ground state configuration is $1s^2 2s^2 2p^2$. Consequently, it can form many different structures resulting in different properties. The allotropes of carbon include one of the hardest materials in nature (diamond), one of the softest materials (graphite), and also a soccer-ball-like form called buckminsterfullerene, C_{60} (Figure 1-2) [6, 7].

The diamond structure is formed from carbon crystallized with a tetrahedral sp^3 bonding configuration in a face-centered cubic (fcc) unit cell with the Lonsdaleite (aka hexagonal diamond) arrangement. A fcc unit cell is divisible into eight small cubes. In

addition to 8 carbon atoms ate the corner of single large cube, 4 additional carbon atoms can be viewed as inserted in the center of the four small cubes that are not adjacent to each other, and four tetrahedral structures are formed. In the tetrahedral coordination, the center carbon atom has four sp^3 hybrid valence electrons, and can link with four other carbons and form four equivalent σ covalent bonds. The four tetrahedral structures in a fcc unit cell form the hexagonal diamond configuration. Diamond is the hardest mineral (Mohs scale of hardness is 10) and because of its mechanical properties can be used to score or nick most other materials. Diamond also has the highest atomic density (3.52 gm/cc) and exhibits an energy gap of 5.46 – 5.6 eV.

Graphene is a carbon structure that consists of three in-plane sp^2 σ covalent bonds and a delocalized out-of-plane π bond forming a hexagonal layered structure. The distance of the nearest-neighbor C-C σ bond (a_{cc}) in the same layer is ca. 1.421 Å. Configurations of graphite exist in alpha (hexagonal ABAB stacking of graphene sheets as in Figure 1-2) and beta (rhombohedral ABCABC stacking of graphene sheets, figure not shown) forms that can be identified through their crystal structure, although the alpha and beta forms of graphite have identical physical properties. In alpha graphite, the distance between each A-B interlayer is ca. 0.335 nm, and the distance between each A-A parallel layer (c-axis) is ca. 0.67 nm. The in-plane bonds of graphene are stronger than diamond. However, the layers in graphite are held together by very weak Van der Waals interactions, making graphite one of the softest materials in nature. This weak interaction allows the easily gliding of sheets, and leads to graphite being a good lubricant.

The structure of buckminsterfullerene (abbr. fullerenes or buckyball, C_{60}), named after the American architect Richard Buckminster Fuller, is a truncated icosahedron, and

was discovered by Kroto and Smalley in 1985 [8]. Fullerene has a deformed sp^2 mixed with sp^3 atomic bonding, resulting from the curvature of C_{60}; the structure consists of 20 hexagons and 12 pentagons. When the number of hexagons is increased to 25, buckyball begins to loose its roundness, and thus spheroid network of C_{60} buckyball becomes the rugby ball shaped, C_{70}. The lack of roundness in the rugby ball shape reduces the stability of its structure.

Further refining techniques for the preparation of fullerene, MWNTs and SWNTs have been synthesized. It is to be noted that SWNTs are sometimes referred to as fullerene nanotubes since the fabrication methods, structures, and bonding of SWNTs and fullerenes are very similar. The structures of carbon nanotubes can also be described as elongated fullerenes with the tubes capped with different types of hemispherical fullerenes.

1.3 Structures of SWNTs

The basic dimensional unit in nanotechnology is the nanometer, which corresponds to a length of 10^{-9} meter. Structures with at least one dimension less than 100 nm can be classified as nanostructures. When materials are nanometer sized, their properties, such as their color, can be very much different from the same material in the bulk form. At nanometer length scales, computational nanotechnology is especially important in predicting structures and methods for the synthesis and manipulation of materials.

CNTs are one of the best examples of a well-defined nanostructure. CNTs have a simple chemical composition and bonding configuration, yet depending on the details of their structures, they exhibit incredible diversity in terms of electronic properties.

CNTs have remarkable quantum effects with special electronic, magnetic, and mechanical properties. The electronic properties of a SWNT depend on its diameter and chirality. Since a SWNT [9] can be reviewed as a rolled up 2D graphene sheet (Figure 1-2), it is possible to theoretically address the electronic properties of a SWNT through the study of a single layer of graphite (graphene).

SWNTs can be classified into three kinds of geometries based on the chiral angle with which the graphene sheet is conceived to wrap: zigzag ($\theta = 0°$), chiral ($0° < \theta < 30°$), and armchair ($\theta = 30°$). In Figure 1-3, zigzag, chiral and armchair tube topographies [10] are shown. The electronic properties of SWNTs, either metallic or semiconducting, also depend on the direction of rolling of the chiral vector $\mathbf{C_h}$ of the graphene sheet which when rolled becomes the circumference of the nanotube, as shown in Figure 1-4 [11, 12]. Every individual SWNT has a specified chiral vector $\mathbf{C}_h$, which is defined by pair of indices (n, m) corresponding to the number of the unit cell vectors, $\mathbf{u_1}$ and $\mathbf{u_2}$, that define the chiral vector [13]. Specifically, the chiral vector is defined as:

$$\mathbf{C}_h = n\mathbf{u_1} + m\mathbf{u_2} \equiv (n, m) \qquad (1.1)$$

SWNTs are also classified into three different electronic classes [14] according to the value of 2n+m (equivalent to n-m) divided by 3, i.e., MOD(2n+m, 3). If 2n+m divided by 3 leaves a remainder of either 1 or 2 (MOD1 or MOD2), tubes are semiconducting nanotubes, whereas MOD0 can be either metallic or quasi-metallic (semi-metallic). For MOD0 and n = m (armchair structure), the SWNT is intrinsically

metallic. While if MOD0 and n ≠ m, then the SWNT will display metallic properties only at room temperature, and exhibit semiconducting property with a small energy (meV) gap at lower temperatures; which is the reason nanotubes with MOD0 and n ≠ m are called quasi-metallic (or semi-metallic) tubes. Nevertheless, neither metallic (n = m) nor semimetallic (n ≠ m) SWNTs show bandgap or fluorescence.

As for the nanotube′s geometry, the diameter of the nanotube (d_T) can also be calculated from the circumference L of a tube, where the length L is ($\sqrt{3}$ a_{cc} $\sqrt{n^2 + nm + m^2}$), where a_{cc} is the nearest-neighbor C-C distance. The optical spectrum of a nanotube depends sensitively on its diameter, reflecting the dependence of the band gap of a semiconducting nanotube on the diameter.

$$d_T = \frac{L}{\pi}; \qquad L = |\mathbf{C}_h| = (\sqrt{3}\, a_{cc}\, \sqrt{n^2 + nm + m^2}\,)\ (\text{Å}) \qquad (1.2)$$

In this equation, the length of a_{cc} may be taken to be the same as in graphite (1.421Å). Hence, the diameter of carbon nanotubes, d_T, can be calculated as $0.783\sqrt{n^2 + nm + m^2}$ Å.

In Figure 1-4, the hexagonal unit vectors of the graphite sheet, $\mathbf{u_1}$ and $\mathbf{u_2}$, have angle of 30° with respect to each other. The unit vectors, $\mathbf{u_1}$ and $\mathbf{u_2}$, can be expressed by the following equations with the lattice constant a, for an x, y coordinate system.

$$\mathbf{u_1} = \left(\frac{\sqrt{3}}{2}a, \frac{a}{2}\right), \qquad \mathbf{u_2} = \left(\frac{\sqrt{3}}{2}a, -\frac{a}{2}\right); \qquad a^2 = \mathbf{u_1}\cdot\mathbf{u_1} = \mathbf{u_2}\cdot\mathbf{u_2} \qquad (1.3)$$

The length of the unit cell $a = |\mathbf{u_1}| = |\mathbf{u_2}| = 2.46$ Å, where the lattice constant, a, as mentioned earlier, equals $\sqrt{3}\, a_{cc}$. The translational vector **T**, parallel to the tube axis and perpendicular to the chiral vector $\mathbf{C_h}$ where $\mathbf{C_h} \cdot \mathbf{T} = 0$, is given by

$$\mathbf{T} = t_1\mathbf{u_1} + t_2\mathbf{u_2} \equiv (t_1, t_2) = \left(\frac{2m+n}{d_R}, -\frac{2n+m}{d_R} \right) \quad (1.4)$$

The parameter d_R is related to the greatest common divisor, d, of (n, m), i.e., gcd(n, m). When n-m is a multiple of 3d, then d_R can be set to 3d. On the other hand, if n-m is not a multiple of 3d, then d_R = d. d_R can also be calculated as the greatest common divisor of (2n+m, 2m+n). Using the example of $\mathbf{C_h}$(n, m) shown in Figure 1-4, where the chiral vector indices are n=8 and m=4, one notes that since n-m = 4 is not a multiple of 3d, d_R will be equal to d = 4, and length of the translation vector can be calculated by

$$T = |\mathbf{T}| = \frac{\sqrt{3}L}{d_R} = \left(\frac{3a_{cc}}{d_R}\sqrt{n^2 + nm + m^2} \right) \quad (1.5)$$

The circumference L of the nanotube is given by equation 1.2, where for (8, 4), L = 2.6 nm. Therefore, the length of the translation vector for a (8, 4) nanotube is 1.13 nm, and **T** is defined as (4, -5), note that the unit cell of a carbon nanotube, shown in the pink rectangle of Figure 1-4, is defined by the chiral vector ($\mathbf{C_h}$) and the translational vector (**T**). The number of hexagons per unit cell in a nanotube, **N,** can be calculated by dividing the area of the unit cell of the nanotube $|\mathbf{C_h} \times \mathbf{T}|$ by the area of hexagons $|\mathbf{u_1} \times \mathbf{u_2}|$. The equation that results is:

$$N = \frac{|C_h \times T|}{|u_1 \times u_2|} = \frac{2(n^2 + nm + m^2)}{d_R} = \frac{2L^2}{a^2 d_R} \quad (1.6)$$

In the case of a (8, 4) tube, the value of N indicates that 56 hexagons areas can be fit inside the area of the nanotube's unit cell.

Another parameter of interest is the chiral angle, θ. This angle is defined as the angle between the chiral vector $\mathbf{C}_h$ and the unit vector $\mathbf{u_1}$, and can be formed from the expression:

$$\cos\theta = \frac{C_h \bullet u_1}{|C_h||u_1|} = \frac{2n+m}{2\sqrt{n^2+nm+m^2}} \qquad 0 \le |\theta| \le 30°$$

as well as equally from two other expressions

$$\sin\theta = \frac{\sqrt{3}m}{2\sqrt{n^2+nm+m^2}}, \text{ and}$$

$$\tan\theta = \frac{\sqrt{3}m}{2n+m} \qquad (1.7)$$

Given the (n, m) indices, it is possible to predict the bandgap and the electronic transition properties, which are very useful in assigning optical electronic absorption and vibrations spectra. According to R. Saito et al. [11], SWNTs demonstrate either metallic or semiconducting behavior depending on the diameter and chirality of the tubes which can be determined from the (n, m) indices [15–17]. Electrons in the π band of graphite that is close to the Fermi level, can be easily excited into conduction antibonding π* bands more easily than the π electrons in in-plane covalent bonds. The π and π* energy bands in a graphene can be used to predict electronic structure of SWNTs by zone folding the 2D energy dispersion of graphene into the 1D Brillouin zone [18, 19]. The 2D energy dispersion of graphene has a bandgap that vanishes at six points (Fermi points, k_F) coinciding with the corners of the hexagonal first Brillouin zone: the π and π* bands touch at the K and K' points (Figure 1-5). The first Brillouin zone is the reciprocal lattice [20] of the primitive cell (smallest unit cell) in 2D graphite, where $\mathbf{Z_1}$ and $\mathbf{Z_2}$ can be expressed as reciprocal vectors of $2\pi(\mathbf{u_2} \times \mathbf{u_3})/V$ and $2\pi(\mathbf{u_3} \times \mathbf{u_1})/V$, respectively. $\mathbf{u_3}$ is the unit vector in *z* direction, and can be assigned as (0, 0, 1). V is a real space volume, and its magnitude can calculate as $(u_1 \bullet u_2 \times u_3) = (u_2 \bullet u_3 \times u_1) = (u_3 \bullet u_1 \times u_2) = (-\sqrt{3})a^2/2$.

$$\mathbf{Z_1} = \frac{2\pi}{V}(\mathbf{u_2} \text{ x } \mathbf{u_3}) = (\frac{1}{\sqrt{3}},1)\frac{2\pi}{a} = (\frac{1}{2},\frac{\sqrt{3}}{2})\frac{4\pi}{\sqrt{3}a}$$

$$\mathbf{Z_2} = \frac{2\pi}{V}(\mathbf{u_3} \text{ x } \mathbf{u_1}) = (\frac{1}{\sqrt{3}},-1)\frac{2\pi}{a} = (\frac{1}{2},-\frac{\sqrt{3}}{2})\frac{4\pi}{\sqrt{3}a} \qquad (1.8)$$

In Figure 5, the Brillouin zone of the carbon nanotube, $\mathbf{C}_h$ (4, 2), is shown as the line segment WW' which is parallel to $\mathbf{K_2}$ and perpendicular to $\mathbf{K_1}$. $\mathbf{K_1}$ and $\mathbf{K_2}$ are reciprocal lattice vectors and can be expressed as:

$$\mathbf{K_1} = \frac{1}{N}\left(-t_2 Z_1 + t_1 Z_2\right), \qquad \mathbf{K_2} = \frac{1}{N}\left(mZ_1 - nZ_2\right) \qquad (1.9)$$

For the tube with chiral vector $\mathbf{C}_h$ = (4, 2), the number of hexagon in the nanotubes unit cell (N) is equal to 28, and the translational vector elements (t_1, t_2) are (4, -5). The 2D Brillouin zone calculations can be further developed to obtain the energy dispersion in the 1D Brillouin zone [18]. The three symmetry points, Γ, K and M, are the center, the corner, and the center of the edge, respectively, in the Brillouin zone of a 2D graphene. The K points of Brillouin zone (K_B) are at the six points where the valence and conduction bands touch each other (Figure 1-5b). For the two types of semiconducting nanotubes, MOD1 and MOD2, there is no k vector (i.e. discrete vectors of N) that can cross a K point. For MOD0, only armchair (n=m) SWNTs are truly metallic, and a subband line (discrete k vector) crosses the K point with zero band gap. For other MOD0 ($n \neq m$, but n-m is a multiple of 3), a small band gap is obtained at lower temperature due to the breaking of symmetry, and can be well explained through the Kataura plot [21].

This brief explanation of the relationship between the SWNT unit cell and Brillouin zone can help in understanding the transitions obtained by optical spectral techniques. The electronic valence and conduction bands transition energies are discussed

further in Chapter 2. A summary of parameters is presented in Table 1. The comparisons of three topologies of nanotubes, armchair, zigzag, and chiral, are categorized in Table 2.

1.4 Electronic and mechanical properties of SWNTs

As mentioned earlier, because of their unique structural, optical [22], mechanical, and electrical properties [23, 24], SWNTs are ideal candidates for components in electronic and/or optoelectronic nanodevices. Most of these devices are generally prepared either by assembling SWNTs on surfaces or by the direct growth of SWNTs on substrates. The remarkable electronic properties of SWNTs, such as the diameter and chirality dependent semiconducting and metallic properties have been confirmed by experimental measurements [25]. The 2D energy dispersion (Equation 1.10) of a CNT was derived from the relationships of π bands of a graphene sheet [6, 11] using the tight binding approximation:

$$E(k_x, k_y) = \pm\gamma\{1 + 4\cos(\frac{\sqrt{3}k_x a}{2})\cos(\frac{k_y a}{2}) + 4\cos^2(\frac{k_y a}{2})\}^{1/2} \qquad (1.10)$$

The γ is the nearest-neighbor interaction parameter taken as (2.9 ± 0.5 eV), and k_x and k_y are wave vectors of a graphene sheet. The simplest form that Eq. 1.10 takes occurs for highly symmetric carbon nanotubes (i.e., achiral). For the (n, n) armchair CNT, the wave vectors in the circumferential direction can be defined as $k_x = 2\pi q/(na\sqrt{3})$ where (q

= 1, …, 2n), and $k_y = k$ ($-\pi<ka<\pi$). For the (n, 0) zigzag CNT, the wave vectors can be defined as $k_x = k$ ($-\pi<\sqrt{3}\,ka<\pi$), and $k_y = 2\pi q/(na)$ where (q = 1, …, 2n).

Extensive theoretical studies have been incredibly helpful for experimental scientists in understanding the electronic properties of the SWNTs, in order to design and further functionalize tubes. The accurate assignment of nanotubes chiralities based on various optical properties is the subject of ongoing research in this field. Chapter 2 will use these formulas and theories as a prelude to categorize, identify, and help in understanding the unusual properties of SWNTs.

Table 1 Summary of parameters for carbon nanotubes

Symbol	Name	Formula and value
a_{cc}	C-C nearest-neighbor distance	1.421 Å
a	Length of unit vector	$a = \sqrt{3}\, a_{cc} = 2.46$ Å
$\mathbf{u_1}$, $\mathbf{u_2}$	Unit vector	$\mathbf{u_1} = \left(\frac{\sqrt{3}}{2}a, \frac{a}{2}\right)$; $\mathbf{u_2} = \left(\frac{\sqrt{3}}{2}a, -\frac{a}{2}\right)$
$\mathbf{Z_1}$, $\mathbf{Z_2}$	Reciprocal lattice vectors	$\mathbf{Z_1} = (\frac{1}{2}, \frac{\sqrt{3}}{2})\frac{4\pi}{\sqrt{3}a}$; $\mathbf{Z_2} = (\frac{1}{2}, -\frac{\sqrt{3}}{2})\frac{4\pi}{\sqrt{3}a}$
$\mathbf{C_h}$	Chiral vector	$\mathbf{C}_h = n\mathbf{u_1} + m\mathbf{u_2} \equiv (n, m)$
L	Length of $\mathbf{C_h}$	$L = \lvert\mathbf{C}_h\rvert = (a\sqrt{n^2 + nm + m^2})$ (Å)
d_T	Tube diameter (circumference)	$d_T = \frac{L}{\pi}$
θ	Chiral angle	$\cos\theta = \frac{2n+m}{2\sqrt{n^2+nm+m^2}}$, $0 \le \lvert\theta\rvert \le 30°$ $\sin\theta = \frac{\sqrt{3}m}{2\sqrt{n^2+nm+m^2}}$ $\tan\theta = \frac{\sqrt{3}m}{2n+m}$
d	gcd(n, m)	d_R = d, if (n-m) is not divisible by 3
d_R	gcd(2n+m, 2m+n)	d_R = 3d, if (n-m) is divisible by 3
T	Translational vector	$\mathbf{T} = t_1\mathbf{u_1} + t_2\mathbf{u_2} \equiv (t_1, t_2)$ $(t_1, t_2) = \left(\frac{2m+n}{d_R}, -\frac{2n+m}{d_R}\right)$
T	Length of **T**	$T = \lvert\mathbf{T}\rvert = \frac{\sqrt{3}L}{d_R}$
N	Number of hexagons in the unit cell of a nanotube	$N = \frac{2(n^2+nm+m^2)}{d_R} = \frac{2L^2}{a^2 d_R}$

Table 2 Comparison of armchair, zigzag, and chiral carbon nanotubes

Structure	Armchair	Zigzag	Chiral
Structure			mixture
parameter	(n, n)	(n, 0)	(n, m)
Chiral vector, $\mathbf{C_h}$	n($\mathbf{u_1} + \mathbf{u_2}$)	n$\mathbf{u_1}$	n$\mathbf{u_1}$ + m$\mathbf{u_2}$
Chiral angle, θ	30°	0°	$\theta = \operatorname{atan}\frac{\sqrt{3}m}{2n+m}$
Diameter, d_T (Å)	1.357n	0.783n	$(a\sqrt{n^2+nm+m^2})/\pi$
d	n	n	gcd(n, m)
d_R	3n	n	gcd(2n+m, 2m+n)
T	(1, -1)	(1, -2)	$\left(\frac{2m+n}{d_R}, -\frac{2n+m}{d_R}\right)$
T	a	$\sqrt{3}$ a	$\frac{\sqrt{3}L}{d_R}$
N	2n	2n	$\frac{2(n^2+nm+m^2)}{d_R}$

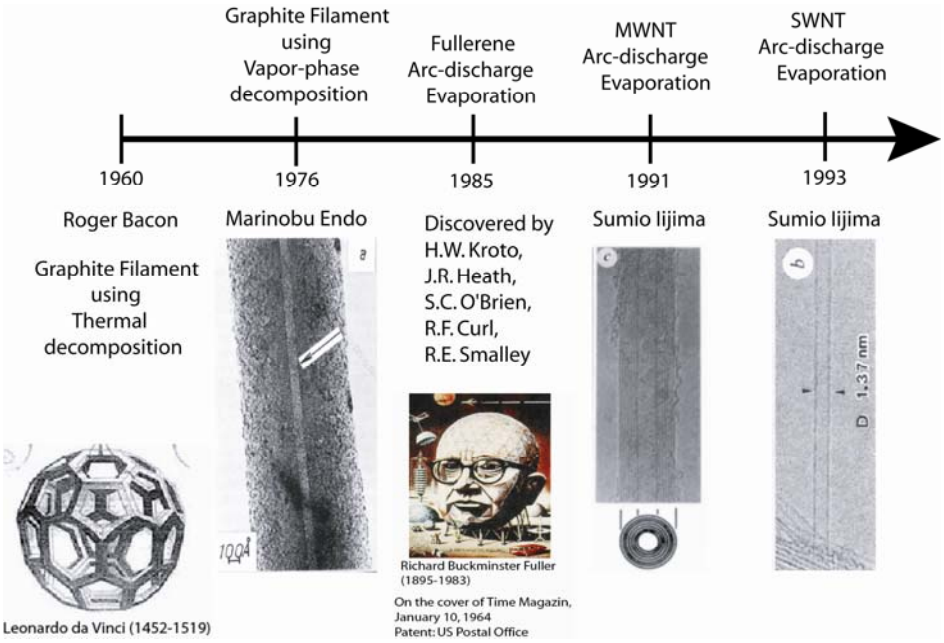

Figure 1-1 Timeline for development of carbon nanotubes. High-resolution electron microscopy images are reproduced [1, 3, 4]. Two inserts display fullerene structures. The first insert was drawn by Leonardo da Vinci in the book *De Divina Proportione* ("On Divine Proportion") by Fra' Luca Pacioli which was published around 1498. The name of Fullerene was given in honor of Buckminster Fuller - an architect who designed the Geodesic Dome in the 1950s. In 2004, the U.S. Postal Office patented a picture drawn by Boris Artzybasheff in 1964 which showed R. Fullerene's photo and the dome structure, and issued a commemorative stamp. Information was obtained from www.fkf.mpg.de/andersen/fullerene/vatican.html and en.wikipedia.org.

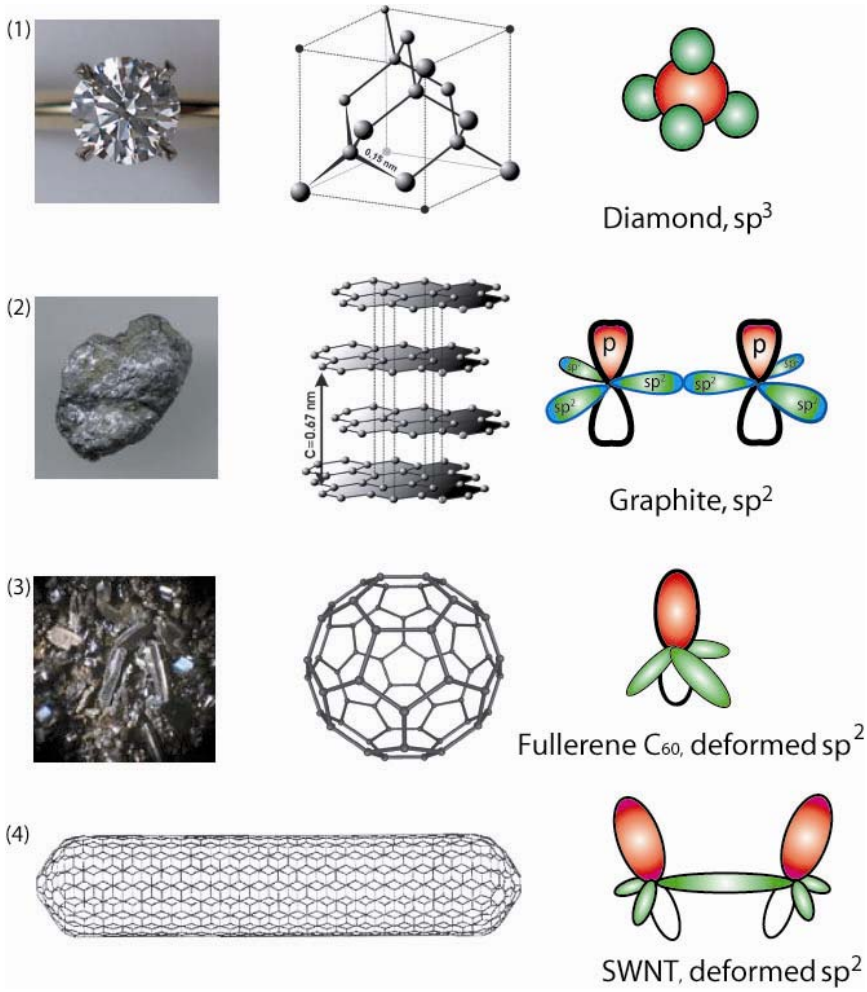

Figure 1-2 Diamond (sp^3), Graphite (sp^2), and Fullerene (deformed sp^2) are displayed in their natural forms (left), atomic structures (middle), and orbital bonding schemes (right), respectively. Permission was granted to copy under GNU General Public License from the Wikipedia Commons. (4) (10, 10). SWNT schematic was reproduced from doi:10.1006/spmi.2000.0883 [9].

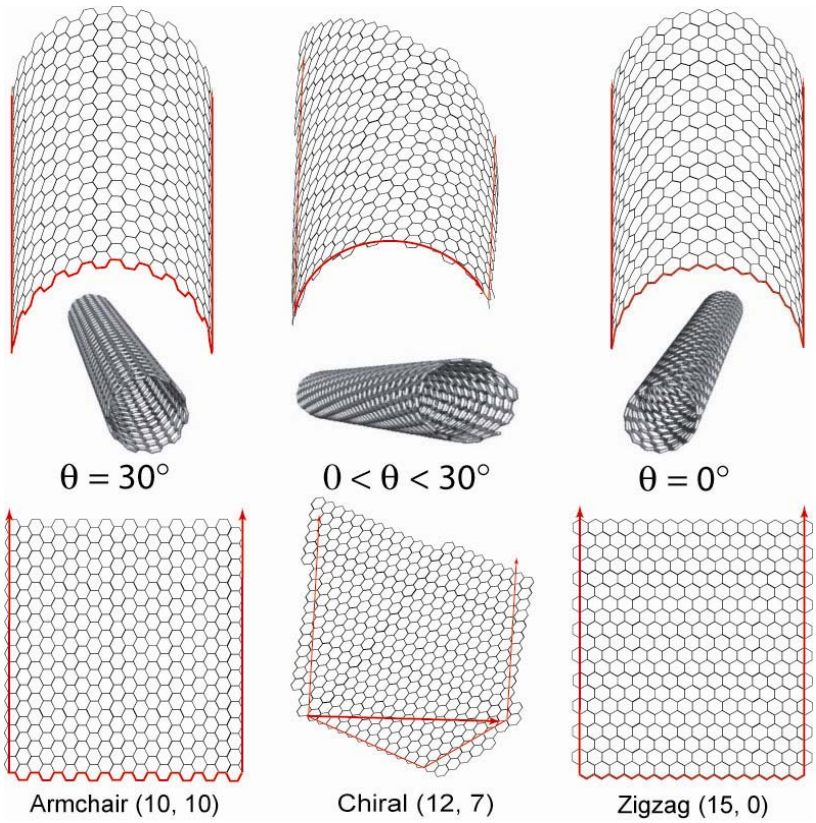

Figure 1-3 Three categories of single-walled carbon nanotubes. Armchair nanotubes, such as the (10, 10) are intrinsic metallic (left), whereas zigzag nanotubes, such as the (15, 0) are semimetallic (right). Chiral nanotubes, such as (12, 7) are semiconducting (middle). Three rolled-up SWNTs were reproduced from Angew. Chem. Int. Ed. 2002, 41, 1853 [10].

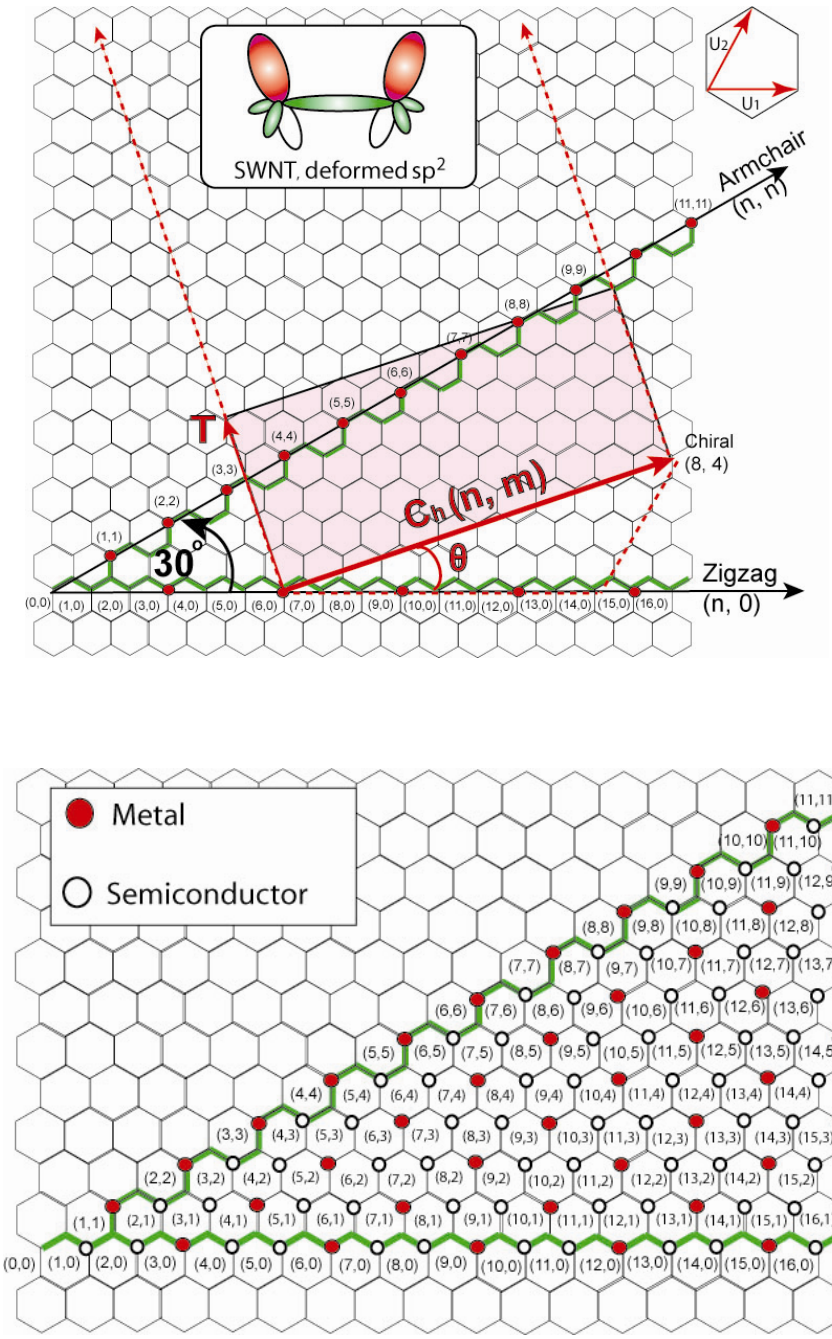

Figure 1-4 Hexagonal lattice carbon nanotubes. The chiral vector ($\mathbf{C}_h$) is represented as $n\mathbf{u}_1 + m\mathbf{u}_2$ where $\mathbf{u}_1$ and $\mathbf{u}_2$ are graphene unit cell vectors. **T** is the translational vector, and θ is the chiral angle. The red circles and empty circles, respectively, denote metallic and semiconducting behavior for each carbon nanotube.

(1) 1D Brillouin Zone

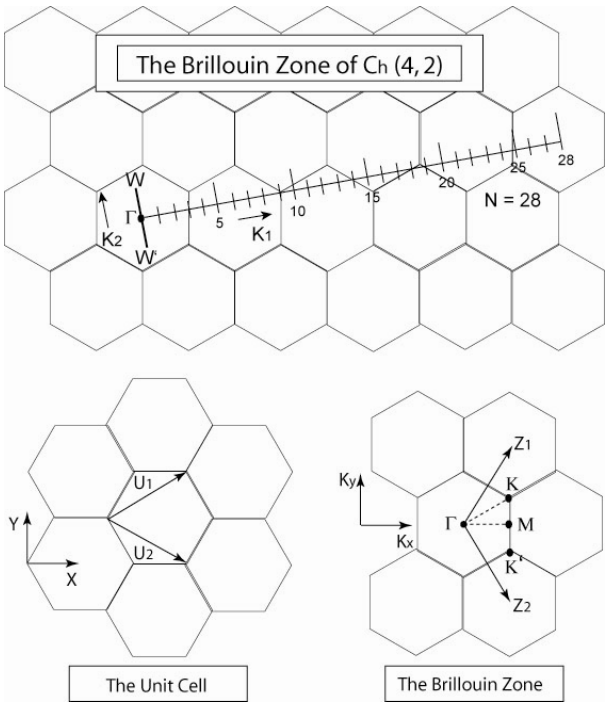

(2) Two- and Three- dimensional K Plots.

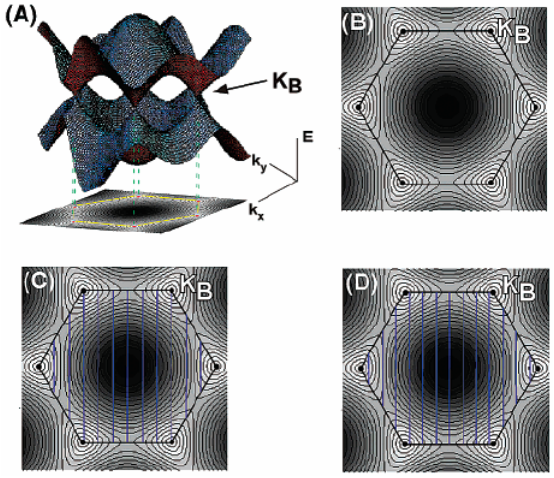

Figure 1-5 (1) The first Brillouin Zone of carbon nanotubes with N=28. $\mathbf{K}_1$ and $\mathbf{K}_2$ are reciprocal lattice vectors corresponding to $\mathbf{C}_h$ (4, 2) and **T** (4, -5). The line segment WW′ represents the brillouin zone of a CNT [18]. (2) A and B display the 3D and 2D graphene energy band, and C and D show allowed 1D wave vectors for semi-metallic (9, 0) and semiconducting (10, 0) tubes in the zigzag direction, respectively. (With permission from C.M. Lieber [14])

References

[1] S. Iijima, Helical Microtubules of Graphitic Carbon, Nature, 354, 56 (1991).

[2] R. Bacon, J. Appl. Phys., 31, 283 (1960).

[3] A. Oberlin, M. Endo, Filamentous Growth of Carbon through Benzene Decomposition, J. Cryst., Growth 32, 335 (1976).

[4] S. Iijima, T. Ichihashi, Single-Shell Carbon Nanotubes of 1-nm Diameter, Nature, 363, 603 (1993).

[5] D.S. Bethune, C.H. Kiang, M.S. DeVries, G. Gorman, R. Savoy, R. Beyers, Cobalt-Catalysed Growth of Carbon Nanotubes with Single-Atomic-Layer Walls, Nature, 363, 605 (1993).

[6] M. Meyyappan, Ed. Carbon Nanotubes, CRC Press LLC (2005).

[7] G.L. Miessler, D.A. Tarr, Inorganic Chemistry 2nd Ed., Prentice-Hill, Inc, New Jersey (1999).

[8] H.W. Kroto, J.R. Heath, S.C. O'Brien, R.F. Curl, R.E. Smalley, C60: Buckminsterfullerene, Nature, 318, 162 (1985).

[9] M. Menon, E. Richter, P. Raghavan, K. Teranishi, Large-Scale Quantum Mechanical Simulations of Carbon Nanowires, Superlattices and Microstructures, 27, 577 (2000).

[10] A. Hirsch, Functionalization of Single-Walled Carbon Nanotubes, Angew. Chem. Int. Ed., 41, 1853 (2002).

[11] R. Saito, M. Fujita, G. Dresselhaus, M.S. Dresselhaus, Electronic Structure of Chiral Graphene Tubules, Appl. Phys. Lett., 60(18), 2204 (1992).

[12] M.S. Dresselhaus, G. Dresselhaus, R. Saito, Physics of Carbon Nanotubes, Carbon, 33(7), 883 (1995).

[13] D. Qian, G.J. Wagner, W.K. Liu, M-F. Yu, R.S. Ruoff, Mechanics of Carbon Nanotubes, Appl. Mech. Rev., 55, 495 (2002).

[14] M. Ouyang, J.-L. Huang, C.M. Lieber, Fundamental Electronic Properties and Applications of Single-Walled Carbon Nanotubes, Acc. Chem. Res., 35, 1018 (2002).

[15] J.W. Mintmire, B.I. Dunlap, C.T. White, Are Fullerene Tubules Metallic? Phys. Rev. Lett., 68, 631 (1992).

[16] N. Hamada, S-i. Sawada, A. Oshiyama, New One-Dimensional Conductors: Graphitic Microtubules, Phys. Rev. Lett., 68, 1579 (1992).

[17] R. Saito, G. Dresselhaus, M.S. Dresselhaus, Carbon Fibers Based on C60 and Their Symmetry, Phys. Rev. B, 45, 6234 (1992).

[18] R. Saito, G. Dresselhaus, M.S. Dresselhaus, Physical Properties of Carbon Nanotubes, Imperial College: London, p191 (1998).

[19] P. Kim, T.W. Odom, J.-L. Huang, C.M. Lieber, Electronic Density of States of Atomically Resolved Single-Walled Carbon Nanotubes: van Hove Singularities and End States, Phys. Rev. Lett., 82, 1225 (1999).

[20] C. Kittel, Introduction to Solid State Physics 7th Ed., John Willey & Sons, Inc., New York, pp52-53 (1996).

[21] H. Kataura, Y. Kumazawa, Y. Maniwa, I. Uemezu, S. Suzuki, Y. Ohtsuka, Y. Achiba, Optical Properties of Single-Walled Carbon Nanotubes, Synt. Met., 103, 2555 (1999).

[22] S.M. Bachilo, M.S. Strano, C. Kittrell, R.H. Hauge, R.E. Smalley, R.B. Weisman, Structure-Assigned Optical Spectra of Single-Walled Carbon Nanotubes, Science, 298, 2361 (2002).

[23] J.W.G. Wildöer, L.C. Venema, A.G. Rinzler, R.E. Smalley, C. Dekker, Electronic Structure of Atomically Resolved Carbon Nanotubes, Nature, 391, 59 (1998).

[24] T.W. Odom, J.-L. Huang, P. Kim, C.M. Lieber, Atomic Structure and Electronic Properties of Single-Walled Carbon Nanotubes, Nature, 391, 62 (1998).

[25] T.W. Odom, J.-L. Huang, P. Kim, C.M. Lieber, Structure and Electronic Properties of Carbon Nanotubes, J. Phys. Chem. B, 104, 2794 (2000).

2

Principal Optical Characterization Techniques to Study Single-Walled Carbon Nanotubes

To understand the properties of nanotubes, it is important to characterize them by a variety of different analytical techniques. Two types of characterization tools, optical spectroscopy and electron microscopy, are generally used to probe the properties of carbon nanotubes. Optical spectroscopy reveals the electronic structure whereas electron microscopy reveals the morphology of the tubes. This chapter discusses the fundamental principles of optical instrumentation used in Raman and UV-Vis-NIR spectroscopy. These spectroscopic techniques are discussed with respect to the assessment of properties and structures of single-walled carbon nanotubes.

There are many instrumental analyses to investigate the uniqueness of SWNTs. Microscopy instruments to probe structures of SWNTs include atomic force microscopy (AFM), transmission electron microscopy (TEM), and fluorescent microscopy. However, optical spectroscopes are the primary equipments that I used to identify the outcome of experimental results in my project; therefore, this chapter only emphasize on UV-Vis-NIR and Raman spectroscopy.

2.1 UV-Vis-NIR Spectroscopy

UV-Vis-NIR spectroscopy is a common quantitative optical spectroscopic analysis technique that is used to investigate the electronic transitions in molecules and solids by the absorption of optical radiation. Electrons in molecules undergo electronic transitions after absorbing electromagnetic radiation from a light source in the ultraviolet (UV, ca. 200-400 nm), visible (Vis, ca. 400-800 nm) and near infrared (NIR, ca. 800-2500 nm) regions. The first commercially available UV-Vis spectrometers were manufactured by Beckman and composed of a molecular hydrogen lamp (the light source), a Brazilian quartz prism (monochromator) and a UV-sensitive phototube [1].

The UV-Vis-NIR spectrum provides useful information about the electronic structure of SWNTs. The band structures of SWNTs are characterized by sharp van Hove singularities (vHs) in the one-dimensional (1D) electronic density of states (DOS) [2]. Semiconducting SWNTs have a band gap and there is no electron density at the Fermi level. Electronic transitions between mirror-image pairs of singularities are allowed and

are detected. Metallic tubes have a finite electron density at the Fermi level but still have sharp spikes in the band structure with optically allowed transitions. The separation between the singularities depends on the diameter [3] and chirality of the SWNTs. Typical SWNT samples show broad UV-Vis-NIR spectra due to the presence of many different nanotubes species, as well as due to the aggregation effects caused by the bundling of SWNTs. UV-Vis-NIR spectroscopy can be used to investigate the solubility and debundling of SWNTs as shown in Figure 2-1 [4, 5]. The schematic shows the DOS of SWNTs and the UV-Vis-NIR spectra obtained for raw HiPco (high pressure CO process) SWNTs dispersed in H_2O using an anionic surfactant AOT (aerosol OT). Upon the individualization of the SWNTs, the energy gaps are no longer distorted by inter-tube interactions, and the van Hove singularities (vHs) display a well defined sharpened absorption peak. The spectrum demonstrates the valence (v) to conduction (c) electronic transition that can be divided into three regions. The features observed in the ultraviolet (UV) region between 400 and 600 nm correspond to the first metallic and semimetallic electronic transitions from v1 to c1, and are denoted as $^{M}E_{11}$. The features observed in the visible (Vis) region between 600 and 800 nm correspond to the second semiconducting electronic transitions from v2 to c2, and are denoted as $^{S}E_{22}$. The features observed in the near infrared (NIR) region between 830 and 1600 nm correspond to the lowest semiconducting electronic transitions from v1 to c1, and are denoted as $^{S}E_{11}$ [6].

The absorption spectroscopy has proven very useful for the purpose of measuring the success of efforts in dispersing bundled SWNTs.

2.2 Raman Spectroscopy

Raman spectroscopy is widely used to examine carbon nanotubes. Indeed, Raman spectroscopy has been widely employed to study graphite and fullerene materials over last few decades. The bonding, aggregation, and functionalization of metallic and semiconducting SWNTs can be probed by Raman spectroscopy.

The basic principle behind Raman spectroscopy is the Raman Effect (inelastic scattering of light) that was named after Sir Chandrasekhara Venkata Raman [7]. Raman published his findings, on inelastic light scattering, with K.S. Krishnan in *Nature*. The discovery of inelastic light scattering won him a Nobel Prize in 1930. Within a few decades after the advent of lasers, Raman scattering has become a useful and reliable probe for investigating almost all materials, and micro-Raman spectroscopy has more recently become a common technique.

As suggested above, Raman scattering involves the inelastic scattering of incident light as some of the incident laser excitation either excites degrees of freedom within the material or receives energy from the material, in accord with conservation of momentum and energy. In other words, the emitted light loses a discrete amount of energy that is used to create phonons. The ability of a photon to interact with a certain vibration transition depends on the selection rules (symmetry) and the energy of photon. To be able to detect a Raman signal (Raman active mode), a molecule must be symmetric. In part (A) of Figure 2-2, Rayleigh (elastic) and Raman (inelastic) scattering is shown. In Rayleigh scattering, when the photon from a light source (incident light frequency, ν_{in}) excites one of the electrons from the ground state to a virtual state (scattered light frequency, ν_{sc}), the increase of energy that is absorbed by electrons is equal to the energy

of the photon, hν. Rayleigh scattering is an elastic scattering process since the incident energy absorbed (E_{in}) and the emission energy (E_{sc}) are the same [8]. In other words, there is no energy lost in Rayleigh scattering (i.e. $\nu_{sc} = \nu_{in}$). However, it is also possible for incident photons to gain or lose energy when they interact with the molecules. This phenomenon observed as a shift in frequency of the emitted light is called Raman scattering (inelastic scattering). Since the excitation energy and the energy of emitted light are different, the change in energy leads to Stokes and anti-Stokes emissions. In Figure 2-2A, schematics (1) and (4) denote the two scattering processes. The Stokes and anti-Stokes emissions have different scattering energies of -ΔE and +ΔE, respectively, from the Rayleigh scattered light.

Raman spectroscopy is one of the most important tools used to study the vibrational properties and electronic structure of SWNTs. Understanding the Raman scattering of graphite will help to elucidate the peaks observed in the Raman spectra of carbon nanotubes, since graphite is built from carbon atoms arranged in a hexagonal pattern. P.-H. Tan et al. [9] have pointed out that only two of the E_{2g} modes (in-plane optical vibrations) located at 42 and 1582 cm^{-1} are Raman active for the D_{6h}^4 point group of graphite for the Brillouin zone. For the double resonance (DR) process in graphite, an electron with momentum (k) is scattered by emitting or absorbing a phonon with momentum (q). The phonon dispersion can be measure by Raman scattering because the phonon wave vectors lead to large disorder-induced Raman bands.

The Raman process in SWNTs includes the absorption and emission of photons in addition to the inelastic scattering of electrons by phonons. Phonons are the quantized normal mode of vibration in a crystal lattice and play an important role in determining the

thermal and electrical conductivities of solids. The Raman spectra of SWNTs and graphite can provide information about the electronic and phonon structure in carbon materials. Phonons can interact with electrons leading to electron-phonon (e-pn) coupling [10]. In semimetallic carbon nanotubes, electron-phonon coupling can induce changes in the electronic band structure and open a small band gap at the Fermi level of the lattice systems leading to superconductivity [11]. Raman scattering processes were discussed in detail by Dresselhaus et al. [12]. As shown in Figure 2-2(B), the cartoon depicts the excitation and relaxation processes involved in first-order Raman scattering with only one-phonon. The phonon scattering can be one-phonon, two-phonon, and so on. During one-phonon first-order Raman scattering, the excitation of an electron occurs from the valence band (at *k* state) to the conduction band by absorbing a photon. The excited electron in the conduction energy band is then scattered by either emitting or absorbing a phonon (k+q state). Since the sketch in Figure 2-2B shows first-order elastic Raman scattering, the phonon with momentum *q* has a value of zero, and the k+q state should not differ from the k state. The last event of first-order Raman scattering is the combination of the relaxation of an electron with a hole yielding an exciton. In Raman spectra, the G band (graphite band, ca. 1582 cm^{-1}) and RBM (radial breathing mode) are both one-phonon first-order Raman modes. In SWNTs, the G band is split into many peaks, and RBM bands are bond-stretching, out-of-plane phonon modes observed at low frequencies around 100-500 cm^{-1}.

Second-order Raman scattering (double resonance, DR) is a much more complicated process. The number of phonons emitted by the electrons for second-order DR Raman scattering (not in sketch) before relaxation can be either one or two. In this

inelastic process, the electron will absorb a photon (at k state), scatter a phonon (at $k+q$ state), scatter back for relaxation (at k state), emit a photon (at k state), and finally, recombine with a hole (at k state) [12]. Therefore, the assignment of second-order Raman scattering depends on the number of emitted phonons, which involve either one-phonon emission or two-phonon emissions. Through electron-phonon coupling, it is possible to observe Raman scattering from an isolated SWNT [13]. In graphite and SWNTs, the D-band (disorder band, ca. 1350 cm^{-1}) and the G′-band (overtone of D band, ca 2700 cm^{-1}) are the results of one-phonon and two-phonon DR Raman scattering processes, respectively.

Figure 2-3 shows the details of the Raman spectra of graphite and carbon nanotubes, with data generated by laser excitation at 2.41 eV (514.5 nm) from reference [12]. There are three major regions in the Raman spectra of SWNTs representing the radial breathing modes (RBM), the disorder-induced D-band, and the tangential graphite G-band. As mention before, the G-band and RBM of SWNTs arise from first-order Raman scattering with one-phonon emission. Figure 2-3A displays the circumferential breathing vibrations of SWNTs in the low-frequency region between 100 and 500 cm^{-1}. In Figure 2-3B, many Raman scattering modes are shown. The G-band is derived from the graphite in-plane mode at about 1582 cm^{-1}, with the G^+ and G^- components being in-plane vibrations along the SWNT axis and the circumferential direction, respectively. Figure 2-3B also shows the D-band (ca. 1350 cm^{-1}) and G′-band (D-band overtone, ca. 2700 cm^{-1}). In one-phonon double resonance, the out-of-plane transverse optical phonon (oTO, ca. 860 cm^{-1}) is infrared active but Raman inactive, and the M-band is an overtone of the oTO mode (i.e., two-phonon double resonance) at about 1720 cm^{-1}. Another two-

phonon double resonance Raman scattering feature is the so-called iTOLA peak which is a combination of iTO (in-plane transverse optical) and LA (longitudinal acoustic) modes.

The RBM of SWNTs is observed only when the carbon nanotubes are single-walled. The RBM is an out-of-plane one-phonon mode corresponding to the movement of the carbon atoms in the radial direction. The A_{1g} breathing mode can be used to predict the approximate diameter of the tube from the frequency equation, $\nu_{RBM} = (A / d_t) + B$, only if the tubes are in the range from 0.6 to 2 nm. The empirical parameters A and B depend on the type of SWNTs and the aggregation state. For HiPco SWNTs, 223.5 nm/cm is used for A, and a value of 12.5 cm^{-1} is used for B [4] from empirical findings. For isolated SWNTs on Si/SiO_2 substrate, a value of 248 nm/cm is used for A, and B, which relates to inter-tube coupling, is assigned a value of zero. For bundled SWNTs, a value of 224 nm/cm is used for A, and B of 14 cm^{-1} [14] is used due to the specific tube-tube interactions. The RBM peaks are diameter dependent as shown in Figure 2-3A, and RBM peak frequencies have a reciprocal relationship to the diameter of the nanotube. From the RBM frequencies in the Raman spectra, the (n, m) indices can be assigned for individual tubes using Eq. (1.2).

The graphite band (G-band) is a Raman-allowed optical mode (E_{2g} mode). The G-band relates to the tangential vibration mode of carbon atoms. Upon excited with the 2.41 eV line from an Ar^+ ion laser, the G-band is observed between 1500 to 1605 cm^{-1} [15]. In Figure 2-3B, the graphitic Raman peak (G-band) can be fitted with a symmetric Lorentzian peak at about 1582 cm^{-1}. However, the SWNT G-band is composed of two major peaks (G^+ and G^-) and several other peaks (M^+, M^-, and iTOLA). The upper-frequency G^+ peak at about 1590 cm^{-1} is associated with vibrations of carbon atoms along

the direction of the SWNT axis, longitudinal optic, LO mode. The G^+ peak is almost independent of tube diameter. The LO mode composed a one-phonon double resonance intervalley scattering process. Intervalley scattering happens when one-phonon scattering takes an electron from the K to K' (or vice versa) points where K and K' are two hexagonal corners of the Brillouin zone. The lower-frequency G^- peak at about 1570 cm^{-1} is associated with carbon atom vibrations along the circumferential direction of the tubes (transverse optic, TO mode). The TO mode is IR active mode in graphite. The lower-frequency G^- peak follows an empirical relationship with the diameter: $G^- = G^+ - C/d_t^2$ [16] where C values of 47.7 and 79.7 nm^2/cm have been used for semiconducting and metallic SWNTs, respectively. The G^- peak shows diameter dependence according to the tubes either semiconducting or metallic. The G^- peak is more sensitive to the electronic properties of SWNTs and indeed semiconducting and metallic SWNTs show dramatically different line shape. In semiconducting SWNTs, the G^- peak exhibits a symmetric Lorentzian lineshape. In metallic SWNTs, the G^- peak shows a much broader asymmetric Breit-Wigner-Fano (BWF) lineshape. The peaks, M^+, M^-, and iTOLA, correspond to two-phonon DR Raman scattering process in SWNTs. In graphite, the out-of-plane transverse optic mode (oTO) is another IR-active mode at about 860 cm^{-1} that is related to SWNTs. Figure 2-3B shows the M band which is the multi-featured band at about 1750 cm^{-1}. The M^+ and M^- peaks are overtone of oTO modes with q=2k (ca. 1732 cm^{-1}) and q=0 (ca. 1755 cm^{-1}), respectively. The iTOLA mode is the combination of the iTO mode (at ca. 1500 cm^{-1}) with the LA mode (at ca. 453 cm^{-1}) at about 1950 cm^{-1} in SWNTs.

The second-order Raman scattering process gives rise to a phenomenon is seen as the one-phonon DR that produces a D-band or the two-phonon DR that generates the overtone of D-band which is the G′-band [12]. These two DR Raman scattering peaks can be found in bundled SWNTs. The name "D-band" is the same as used from the disorder-induced mode for graphite at about 1355 cm^{-1}. The G′-band is the overtone of the D-band and is located at about 2700 cm^{-1}. The D- and G′- band frequencies increase with increasing laser excitation energies. However, the G′ band frequency is not exactly twice of the D band because the Stokes and anti-Stokes frequencies of G′- and D- bands are not exactly the same [17]. Unlike first-order Raman scattering, the D- and G′- bands are not predicted by group theory.

Thus, Raman spectroscopy is a powerful probe of the structure, electronic structure, and electron-phonon coupling in SWNTS. Overall, the major peaks, the G-band, the D-band, and the RBM are sufficient for studying the chemical functionalization of SWNTs and the formation of nanotube composite.

2.3 Relationship between UV-Vis-NIR and Raman Spectroscopy

Understanding the electronic properties of SWNTs is important for achieving the separation of nanotubes by chirality for metallic or semiconducting; as is necessary for practical applications. UV-Vis-NIR spectra can be used to determine whether the SWNTs are bundled or individualized. The Raman spectra can be used to determine whether the SWNTs are metallic or semiconducting. The optical transition between vHs observed as peaks in the UV-Vis-NIR spectra can be used in conjunction with resonant Raman spectroscopy and theoretical calculations to assign the (n, m) indices of each species of nanotubes in a sample.

The energy difference between mirror image of vHs in the conduction and valence bands can be written as E_{cv}, where this number represents the *i*th number of the band. The transition energy can be roughly calculated as ${}^{S}E_{11} = 2a_{cc}\beta/d$, ${}^{S}E_{22} = 4a_{cc}\beta/d$ [18], and ${}^{S}E_{33} = 8a_{cc}\gamma /d$ [19] where a_{cc} is the nearest neighbor carbon-carbon bond distance (0.144 nm) in graphite, γ is the pi-orbital transfer resonance integer (2.9 ± 0.5 eV), and d is the diameter of the nanotube. Theoretical calculations by Saito et al [20] indicate that the vHs transition energies are dependent on the diameter of the nanotubes. This simple relationship can be generalized as ${}^{S}E_{ii} = 2na_{cc}\gamma/d$ where n = 1, 2, 4, 5 for ${}^{S}E_{11}$, ${}^{S}E_{22}$, ${}^{S}E_{33}$, ${}^{S}E_{44}$, respectively [21]. However, a much more correlation has been determined from experimental investigations [4]. Weisman et al. [22] have developed the following relationships to correlate the transition energies to the nanotube diameter based on fluorescence measurements of individual SWNTs. These equations are:

For MOD(n-m, 3) = MOD1,

$$\nu_{11} = 10^7/(157.5+1066.9d_t) - 771\ [\cos(3\theta)]^{1.374}/d_t^{2.272} \quad (2.1)$$

$$\nu_{22} = 10^7/(145.6+575.7d_t) + 1326\ [\cos(3\theta)]^{0.828}/d_t^{1.809} \quad (2.2)$$

For MOD(n-m, 3) = MOD2,

$$\nu_{11} = 10^7/(157.5+1066.9d_t) + 347\ [\cos(3\theta)]^{0.886}/d_t^{2.129} \quad (2.3)$$

$$\nu_{22} = 10^7/(145.6+575.7d_t) - 1421\ [\cos(3\theta)]^{1.110}/d_t^{2.497} \quad (2.4)$$

The chiral angle, θ, has to be converted from degrees into π. The Weisman group [22] has listed the transition energies for optical transitions between the first two pairs of vHs for each specific species (n, m) of semiconducting nanotubes. In Table 3, information about the RBM frequencies has been added, and all the parameters have been recalculated.

Metallic SWNTs can are of two types, either intrinsic metallic SWNTs with an armchair topology or semi-metallic SWNTs with a zigzag or chiral topology. Armchair (n, n) tubes with a chiral warping angle of 30° and zigzag (n, 0) tubes with a chiral wrapping angle of 0° show very different band structure, as is clear from the DOS diagrams in Figure 2-4. The (9, 0) zigzag [23] and (10, 10) armchair [24] SWNTs in Figure 2-4 exhibit metallic behavior. The trigonal warping effect of the vHs of zigzag metallic nanotubes (a semi-metallic property) is shown as bold lines that intersect a corner of the K point at the Fermi energy in the two-dimensional Brillouin zone of hexagonal graphite. In contrast, the bold lines for intrinsic armchair metallic nanotubes display differently from zigzag metallic. The bold lines for armchair tubes line up at the

side of the hexagon which connects the line between KK' and the middle of the upper two M positions in the trigonal plane. Using the equation presented in 1.10 [3], the numerical assignment for the first pair transition of vHs for each specific species (n, m) of metallic SWNTs are listed in Table 4.

The simple calculation of van Hove optical transitions can be ${}^{M}E_{11} = 6a_{cc}\gamma/d$ [19] was derived by Mintmire and White [25]. From this equation for isolated SWNTs, the relationship between metallic and semiconducting tubes with the same tube diameter can be calculated as:

$$ {}^{M}E_{11}(d_M) = 3\ {}^{S}E_{11}(d_S) \qquad \text{where } d_{tube} = d_M = d_S \qquad (2.5) $$

A more detailed calculation for metallic SWNTs with (MOD0) for v1→c1 and v2→c2 optical transitions has been developed by the Strano group [26]. The formula in Eq (2.5) can be rewritten separately for metallic (MOD0) into intrinsic metallic (armchair topology, n=m) and semi-metallic (n≠m) SWNTs [27]. Empirically, this relationship has been calculated as for armchair SWNTs.

$$ \lambda_{11}^{armchair} = \frac{hc}{A}\left(\frac{d}{6a} + \frac{aB}{4d}\right) \qquad (2.6) $$

The metallic transition states are only seen when n=m in the armchair topology. The parameters, A and B, depend on the laser excitation energies. Table 4 summarizes the optical transition energies of metallic SWNTs calculated using equation 2.6. The values of (A, B, β, δ) are approximately (3 eV, 4.5, 2.23 eV, -0.78) obtained upon excitation using discrete Ar^{+} laser source between 458- and 514.5-nm [26]. The derivative energy for zigzag topology that produces splitting that corresponds with valence π (E^{+}) and conduction π^{*} (E^{-}) energy bands are:

$$\frac{1}{\lambda_{11}^{+}} = \frac{1}{\lambda_{11}^{armchair}} + \frac{2\beta}{hc}\left[-\frac{3}{2}\left(\frac{a_{cc}}{d}\right)^2 + 3\delta\left(\frac{a_{cc}}{d}\right)^3 \right]\cos(3\alpha) \qquad (2.7)$$

$$\frac{1}{\lambda_{11}^{-}} = \frac{1}{\lambda_{11}^{armchair}} + \frac{2\beta}{hc}\left[\frac{3}{2}\left(\frac{a_{cc}}{d}\right)^2 + 3\delta\left(\frac{a_{cc}}{d}\right)^3 \right]\left(\cos(3\alpha)\right)^2 \qquad (2.8)$$

Although many experiments have been performed in order to verify the computational prediction, it has proven to be quite challenging to match empirical and computational results. Table 3 and Table 4 summarize the optical transition energies and RBM frequencies for different (n, m) chiralities of SWNTs. The experimental methods are being continuously improved, and computational methods are being developed for better ways to give a deeper understanding of the observed results. With the help from many other research reports, semiconducting and metallic tables are recalculated using the formula in the Dresselhaus and Eklund report [28].

Accurately identifying the chirality of a given nanotube requires much effort and the use of complementary analytical techniques. Of course, there are many other techniques that can be used to identify specific species of SWNTs. For example, scanning tunneling microscopy (STM) can be used to directly observe and record the chiral angle of a tube. However, Raman and UV-Vis-NIR spectroscopy have been most frequently used to identify the chirality of nanotubes.

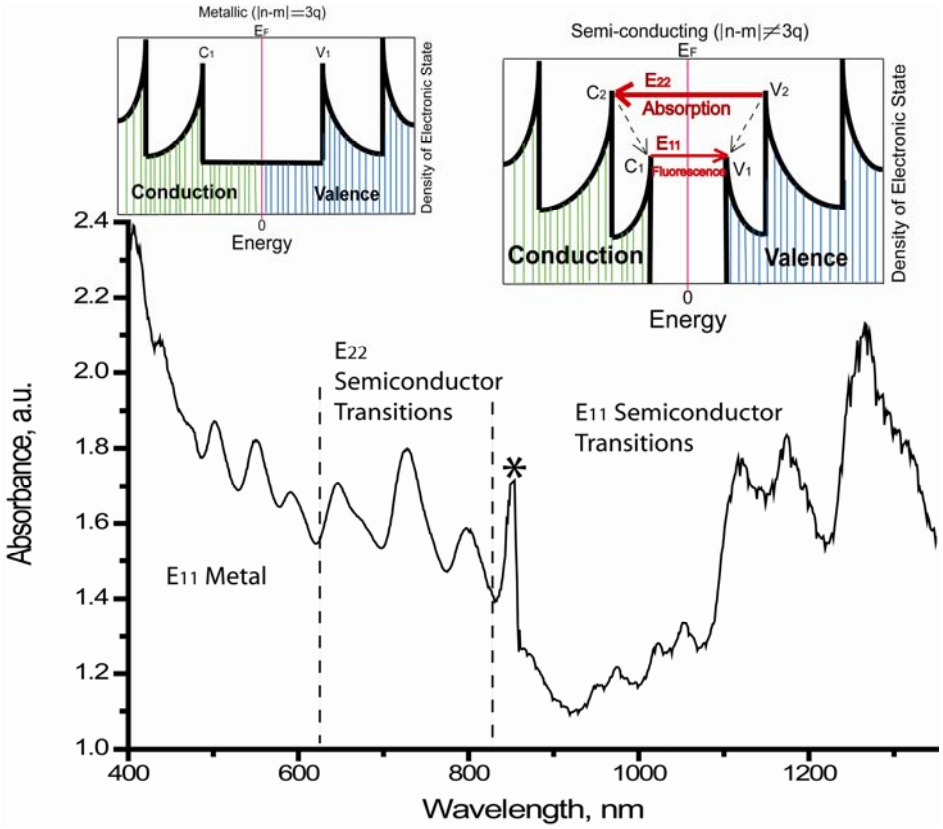

Figure 2-1 UV-Vis-NIR spectra of raw HiPco SWNTs dispersed in H_2O using an anionic surfactant AOT aqueous solution. Peaks are observed in three broad regions of the electromagnetic spectrum. Peaks corresponding to metallic E_{11} (v1→c1), semiconducting E_{22} (v2→c2), and semiconducting E_{11} (v1→c1) are observed in the range from 440 to 645 nm, 600 to 800 nm and 830 to 1600 nm, respectively. The insets show DOS diagrams for metallic and semiconducting SWNTs.

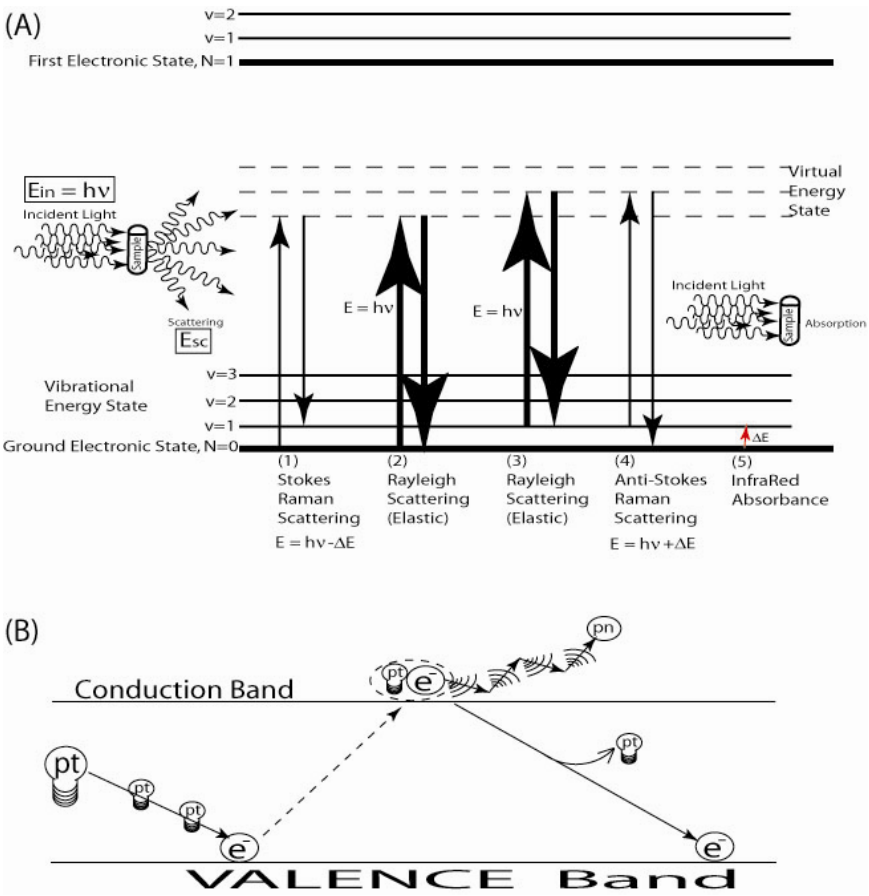

Figure 2-2 Diagrams depicting Rayleigh and Raman Scattering (A) and electron-photon, electron-phonon coupling (B). Rayleigh scattering in Part A (2) and (3) is energy conserved (elastic). The energy changes upon inelastic scattering are depicted for the Stokes (1) and anti-Stokes (4) emissions. The energy difference for the Rayleigh radiation is the energy of the first vibrational level of the ground state, $\pm\Delta E$. ΔE is identical to IR absorption energy (5). Cartoon (B) displays the electron excitation and relaxation mechanism for the absorption of a photon, scattering by a phonon and emission of a photon back to valence band.

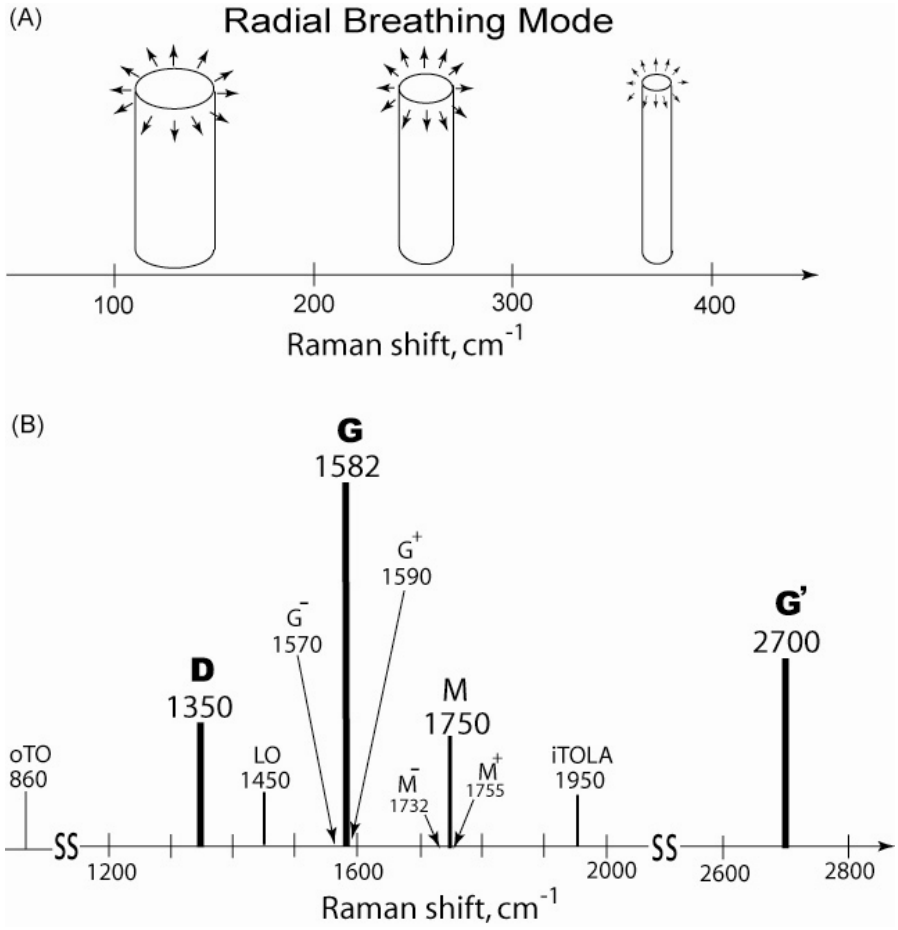

Figure 2-3 Raman peaks of graphite and SWNTs observed for the excitation at 514.5 nm. (A) Radial breathing mode (RBM) in the low frequency region between 100 and 400 cm^{-1}. (B) The Raman active mode (G-band) in graphite; G^+ and G^- are vibrations around tube axis and circumference in SWNTs, respectively. The D-band is the defective peak, and the G′-band is the D-band overtone. The oTO is a out-of-plane transverse optical phonon mode. The M-band is the overtone of the oTO mode.

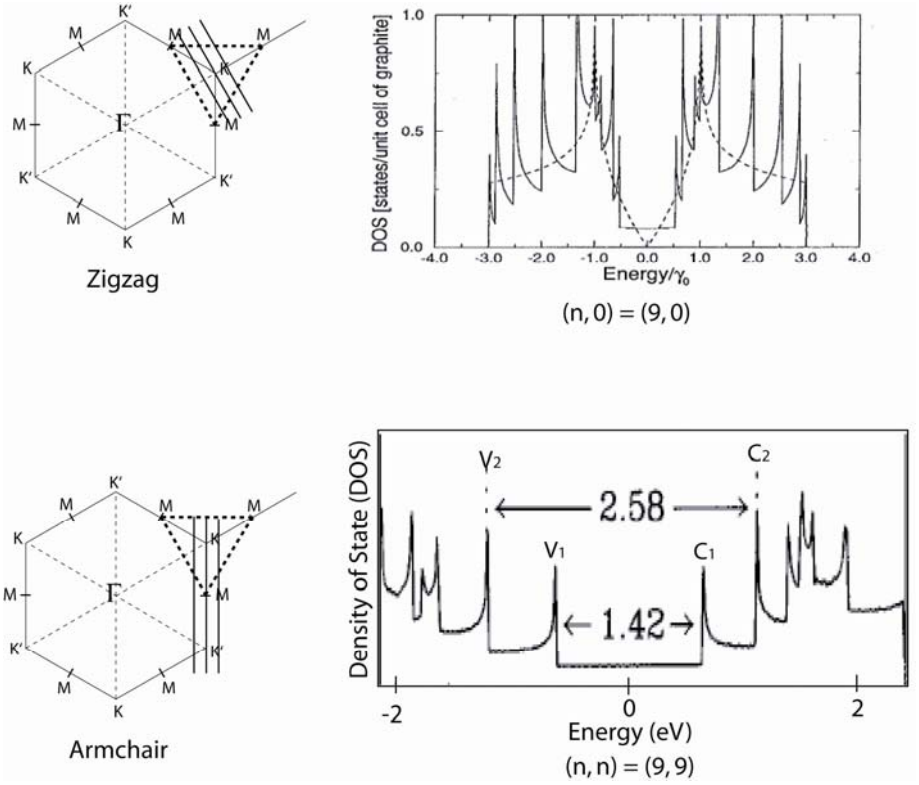

Figure 2-4 The trigonal warping effect [20] of metallic carbon nanotubes for zigzag (top) and armchair (bottom) chiralities reproduced from the Dresselhaus group [23, 24].

Table 3 Numerical assignments of (n, m) structures to the first and second van Hove optical transitions for semiconducting (MOD1) and (MOD2) single-walled carbon nanotubes.

(n, m)	d_t (nm)	ω (cm^{-1})	θ (deg)	λ_{11} (nm)	ν11 (cm^{-1})	E11 (eV)	λ22 (nm)	ν22 (cm^{-1})	E22 (eV)	MOD (n-m,3)
(4, 0)	0.318	716.3	0.00	1030	9704	1.203	244	41010	5.085	1
(4, 2)	0.420	544.5	19.11	562	17783	2.205	511	19558	2.425	2
(4, 3)	0.483	475.3	25.28	701	14261	1.768	398	25147	3.118	1
(5, 0)	0.397	575.5	0.00	508	19692	2.442	803	12455	1.544	2
(5, 1)	0.442	518.1	8.95	857	11670	1.447	330	30279	3.754	1
(5, 3)	0.556	414.7	21.79	720	13884	1.721	522	19148	2.374	2
(5, 4)	0.620	372.9	26.33	836	11964	1.483	483	20697	2.566	1
(6, 1)	0.521	441.8	7.59	653	15323	1.900	632	15828	1.962	2
(6, 2)	0.572	402.9	13.90	895	11169	1.385	418	23900	2.963	1
(6, 4)	0.692	335.4	23.41	873	11452	1.420	578	17312	2.146	2
(6, 5)	0.757	307.6	27.00	977	10238	1.269	566	17666	2.190	1
(7, 0)	0.556	414.7	0.00	962	10397	1.289	395	25318	3.139	1
(7, 2)	0.650	356.4	12.22	802	12468	1.546	626	15977	1.981	2
(7, 3)	0.706	329.2	17.00	993	10072	1.249	505	19819	2.457	1
(7, 5)	0.829	282.1	24.50	1024	9768	1.211	645	15496	1.921	2
(7, 6)	0.895	262.3	27.46	1120	8927	1.107	648	15441	1.914	1
(8, 0)	0.635	364.4	0.00	776	12886	1.598	660	15146	1.878	2
(8, 1)	0.678	342.0	5.82	1042	9600	1.190	471	21226	2.632	1
(8, 3)	0.782	298.3	15.30	952	10508	1.303	665	15029	1.863	2
(8, 4)	0.840	278.5	19.11	1112	8989	1.115	589	16981	2.105	1
(8, 6)	0.966	243.9	25.28	1173	8525	1.057	718	13928	1.727	2
(8, 7)	1.032	229.1	27.80	1265	7906	0.980	729	13727	1.702	1
(9, 1)	0.757	307.6	5.21	912	10964	1.359	691	14466	1.794	2
(9, 2)	0.806	289.9	9.83	1138	8787	1.089	551	18155	2.251	1
(9, 4)	0.916	256.6	17.48	1101	9086	1.126	722	13843	1.716	2
(9, 5)	0.976	241.6	20.63	1242	8049	0.998	672	14883	1.845	1
(9, 7)	1.103	215.1	25.87	1322	7567	0.938	793	12610	1.563	2
(9, 8)	1.170	203.6	28.05	1410	7091	0.879	809	12362	1.533	1
(10, 0)	0.794	294.0	0.00	1156	8652	1.073	537	18606	2.307	1
(10, 2)	0.884	265.3	8.95	1053	9493	1.177	737	13574	1.683	2
(10, 3)	0.936	251.3	12.73	1250	8002	0.992	632	15834	1.963	1
(10, 5)	1.050	225.3	19.11	1249	8006	0.993	788	12695	1.574	2
(10, 6)	1.111	213.6	21.79	1378	7258	0.900	754	13262	1.644	1
(10, 8)	1.240	192.7	26.33	1470	6805	0.844	869	11502	1.426	2
(10, 9)	1.307	183.5	28.26	1556	6427	0.797	889	11248	1.395	1
(11, 0)	0.873	268.4	0.00	1037	9644	1.196	745	13431	1.665	2
(11, 1)	0.916	256.6	4.31	1265	7906	0.980	610	16388	2.032	1
(11, 3)	1.014	233.0	11.74	1197	8353	1.036	793	12617	1.564	2
(11, 4)	1.068	221.7	14.92	1372	7291	0.904	712	14036	1.740	1
(11, 6)	1.186	201.0	20.36	1397	7157	0.887	858	11661	1.446	2
(11, 7)	1.248	191.6	22.69	1517	6593	0.817	836	11968	1.484	1
(11, 9)	1.377	174.8	26.70	1617	6183	0.767	947	10564	1.310	2
(11, 10)	1.444	167.2	28.43	1702	5876	0.729	969	10320	1.280	1
(12, 1)	0.995	237.2	3.96	1170	8549	1.060	799	12516	1.552	2
(12, 2)	1.041	227.2	7.59	1379	7254	0.899	686	14575	1.807	1
(12, 4)	1.145	207.7	13.90	1342	7452	0.924	855	11693	1.450	2
(12, 5)	1.201	198.5	16.63	1500	6667	0.827	793	12605	1.563	1
(12, 7)	1.321	181.6	21.36	1545	6473	0.803	930	10751	1.333	2
(12, 8)	1.384	174.0	23.41	1657	6033	0.748	917	10910	1.353	1
(12, 10)	1.515	160.1	27.00	1765	5666	0.703	1024	9763	1.210	2

Table 3 (CONT'D)

(n, m)	d_t (nm)	ω (cm^{-1})	θ (deg)	λ_{11} (nm)	ν11 (cm^{-1})	E11 (eV)	λ22 (nm)	ν22 (cm^{-1})	E22 (eV)	MOD (n-m,3)
(12, 11)	1.582	153.8	28.56	1848	5411	0.671	1049	9535	1.182	1
(13, 0)	1.032	229.1	0.00	1384	7228	0.896	677	14770	1.831	1
(13, 2)	1.120	212.1	7.05	1307	7651	0.949	858	11661	1.446	2
(13, 3)	1.170	203.6	10.16	1498	6674	0.827	764	13095	1.624	1
(13, 5)	1.278	187.4	15.61	1487	6723	0.834	922	10843	1.344	2
(13, 6)	1.336	179.8	17.99	1633	6124	0.759	874	11441	1.419	1
(13, 8)	1.457	165.9	22.17	1692	5909	0.733	1004	9956	1.234	2
(13, 9)	1.521	159.5	24.01	1800	5556	0.689	997	10027	1.243	1
(13, 11)	1.652	147.8	27.25	1912	5230	0.648	1102	9071	1.125	2
(13, 12)	1.719	142.5	28.68	1994	5014	0.622	1128	8862	1.099	1
(14, 0)	1.111	213.6	0.00	1295	7721	0.957	859	11640	1.443	2
(14, 1)	1.153	206.3	3.42	1502	6660	0.826	748	13364	1.657	1
(14, 3)	1.248	191.6	9.52	1447	6910	0.857	920	10867	1.347	2
(14, 4)	1.300	184.5	12.22	1623	6160	0.764	842	11875	1.472	1
(14, 6)	1.411	170.9	17.00	1633	6123	0.759	992	10078	1.249	2
(14, 7)	1.470	164.5	19.11	1769	5653	0.701	955	10476	1.299	1
(14, 9)	1.594	152.7	22.85	1840	5435	0.674	1080	9261	1.148	2
(14, 10)	1.658	147.3	24.50	1943	5147	0.638	1078	9279	1.150	1
(14, 12)	1.789	137.4	27.46	2059	4856	0.602	1181	8470	1.050	2
(14, 13)	1.857	132.9	28.78	2141	4671	0.579	1208	8278	1.026	1
(15, 1)	1.232	193.8	3.20	1426	7011	0.869	920	10864	1.347	2
(15, 2)	1.278	187.4	6.18	1622	6165	0.764	822	12163	1.508	1
(15, 4)	1.377	174.8	11.52	1589	6294	0.780	986	10140	1.257	2
(15, 5)	1.431	168.7	13.90	1753	5706	0.707	921	10858	1.346	1
(15, 7)	1.546	157.1	18.14	1779	5621	0.697	1064	9396	1.165	2
(15, 8)	1.606	151.7	20.03	1907	5243	0.650	1035	9663	1.198	1
(15, 10)	1.730	141.7	23.41	1987	5032	0.624	1156	8650	1.072	2
(15, 11)	1.795	137.0	24.92	2087	4792	0.594	1158	8635	1.071	1
(15, 13)	1.927	128.5	27.64	2207	4532	0.562	1259	7942	0.985	2
(15, 14)	1.994	124.6	28.86	2287	4372	0.542	1288	7767	0.963	1
(16, 0)	1.270	188.4	0.00	1623	6163	0.764	815	12264	1.521	1
(16, 2)	1.357	177.2	5.82	1561	6405	0.794	984	10162	1.260	2
(16, 3)	1.405	171.6	8.44	1746	5728	0.710	898	11139	1.381	1
(16, 5)	1.508	160.7	13.17	1732	5775	0.716	1055	9480	1.175	2
(16, 6)	1.564	155.4	15.30	1885	5305	0.658	1000	9999	1.240	1
(16, 8)	1.680	145.5	19.11	1925	5194	0.644	1138	8789	1.090	2
(16, 9)	1.741	140.9	20.82	2047	4885	0.606	1115	8968	1.112	1
(16, 11)	1.867	132.2	23.90	2134	4685	0.581	1233	8111	1.006	2
(16, 12)	1.932	128.2	25.28	2231	4482	0.556	1238	8077	1.001	1
(16, 14)	2.064	120.8	27.80	2354	4249	0.527	1338	7475	0.927	2
(16, 15)	2.132	117.3	28.93	2434	4109	0.509	1367	7315	0.907	1
(17, 0)	1.350	178.1	0.00	1552	6443	0.799	984	10167	1.261	2
(17, 1)	1.391	173.2	2.83	1744	5733	0.711	886	11289	1.400	1
(17, 3)	1.483	163.2	7.99	1699	5886	0.730	1050	9525	1.181	2
(17, 4)	1.533	158.3	10.33	1873	5339	0.662	974	10263	1.272	1
(17, 6)	1.641	148.7	14.56	1875	5332	0.661	1125	8886	1.102	2
(17, 7)	1.697	144.2	16.47	2020	4951	0.614	1079	9264	1.149	1
(17, 9)	1.816	135.6	19.93	2072	4827	0.599	1212	8248	1.023	2
(17, 10)	1.877	131.6	21.49	2188	4570	0.567	1195	8367	1.037	1
(17, 12)	2.004	124.0	24.32	2281	4383	0.543	1310	7633	0.946	2
(17, 13)	2.069	120.5	25.60	2376	4209	0.522	1318	7587	0.941	1
(17, 15)	2.202	114.0	27.93	2501	3999	0.496	1416	7060	0.875	2
(17, 16)	2.269	111.0	29.00	2580	3876	0.481	1447	6913	0.857	1

Table 3 (CONT'D)

(n, m)	d_t (nm)	ω (cm^{-1})	θ (deg)	λ_{11} (nm)	$\nu 11$ (cm^{-1})	E11 (eV)	$\lambda 22$ (nm)	$\nu 22$ (cm^{-1})	E22 (eV)	MOD (n-m,3)
(18, 1)	1.470	164.5	2.68	1682	5944	0.737	1048	9543	1.183	2
(18, 2)	1.515	160.1	5.21	1868	5353	0.664	958	10433	1.294	1
(18, 4)	1.611	151.2	9.83	1838	5439	0.674	1118	8947	1.109	2
(18, 5)	1.663	146.9	11.93	2003	4992	0.619	1052	9508	1.179	1
(18, 7)	1.773	138.5	15.75	2020	4952	0.614	1197	8351	1.035	2
(18, 8)	1.831	134.6	17.48	2157	4637	0.575	1159	8629	1.070	1
(18, 10)	1.951	127.0	20.63	2218	4509	0.559	1288	7765	0.963	2
(18, 11)	2.013	123.5	22.07	2330	4291	0.532	1275	7842	0.972	1
(18, 13)	2.141	116.9	24.68	2428	4118	0.511	1388	7206	0.893	2
(18, 14)	2.206	113.8	25.87	2521	3966	0.492	1398	7153	0.887	1
(18, 16)	2.339	108.1	28.05	2648	3777	0.468	1495	6688	0.829	2
(18, 17)	2.407	105.4	29.05	2727	3668	0.455	1526	6553	0.813	1
(19, 0)	1.508	160.7	0.00	1867	5357	0.664	953	10492	1.301	1
(19, 2)	1.594	152.7	4.95	1816	5507	0.683	1114	8979	1.113	2
(19, 3)	1.641	148.7	7.22	1994	5015	0.622	1033	9683	1.201	1
(19, 5)	1.741	140.9	11.39	1979	5052	0.626	1187	8422	1.044	2
(19, 6)	1.795	137.0	13.29	2135	4683	0.581	1130	8853	1.098	1
(19, 8)	1.907	129.7	16.76	2164	4621	0.573	1271	7869	0.976	2
(19, 9)	1.966	126.2	18.35	2295	4357	0.540	1238	8076	1.001	1
(19, 11)	2.087	119.6	21.25	2364	4230	0.524	1364	7332	0.909	2
(19, 12)	2.149	116.5	22.57	2473	4044	0.501	1355	7379	0.915	1
(19, 14)	2.278	110.6	25.00	2575	3883	0.481	1465	6824	0.846	2
(19, 15)	2.343	107.9	26.11	2666	3750	0.465	1478	6767	0.839	1
(19, 17)	2.476	102.8	28.16	2795	3578	0.444	1574	6353	0.788	2
(19, 18)	2.544	100.3	29.11	2873	3480	0.432	1605	6229	0.772	1
(20, 0)	1.588	153.3	0.00	1808	5531	0.686	1113	8989	1.114	2
(20, 1)	1.629	149.7	2.42	1990	5024	0.623	1023	9775	1.212	1
(20, 3)	1.719	142.5	6.89	1952	5124	0.635	1181	8466	1.050	2
(20, 4)	1.768	138.9	8.95	2122	4711	0.584	1108	9025	1.119	1
(20, 6)	1.872	131.9	12.73	2121	4715	0.585	1258	7947	0.985	2
(20, 7)	1.927	128.5	14.46	2270	4405	0.546	1208	8280	1.027	1
(20, 9)	2.041	122.0	17.65	2309	4331	0.537	1345	7435	0.922	2
(20, 10)	2.100	118.9	19.11	2435	4107	0.509	1318	7589	0.941	1
(20, 12)	2.223	113.0	21.79	2511	3983	0.494	1440	6943	0.861	2
(20, 13)	2.286	110.3	23.02	2616	3822	0.474	1435	6969	0.864	1
(20, 15)	2.415	105.1	25.28	2722	3673	0.455	1543	6479	0.803	2
(20, 16)	2.480	102.6	26.33	2812	3556	0.441	1558	6420	0.796	1
(20, 18)	2.614	98.0	28.26	2942	3399	0.421	1653	6050	0.750	2
(20, 19)	2.682	95.8	29.15	3020	3312	0.411	1685	5936	0.736	1

Table 4 Numerical assignment of (n, m) structures of the first van Hove optical transitions for metallic (MOD0) single-walled carbon nanotubes using discrete Ar^+ (between 458 and 514.5 nm) laser excitation.

(n, m)	dt(nm)	ω(cm-1)	θ(deg)	λ11(nm)	λ11+(nm)	λ11-(nm)
(4, 1)	0.364	626.8	10.89	358.1	420.2	354.4
(6, 0)	0.476	481.7	0.00	368.5	502.9	336.2
(5, 2)	0.496	463.3	16.10	372.2	340.5	367.4
(4, 4)	**0.550**	**418.8**	**30.00**	**384.9**		
(7, 1)	0.599	385.4	6.59	398.5	445.0	387.2
(6, 3)	0.630	367.2	19.11	407.7	459.0	392.8
(5, 5)	**0.688**	**337.6**	**30.00**	**426.3**		
(9, 0)	0.715	325.3	0.00	435.5	498.0	408.8
(8, 2)	0.728	319.7	10.89	440.1	456.9	437.6
(7, 4)	0.766	304.4	21.05	453.7	507.6	430.1
(6, 6)	**0.825**	**283.4**	**30.00**	**475.9**		
(10, 1)	0.836	279.7	4.72	480.2	479.8	480.2
(9, 3)	0.859	272.8	13.90	488.8	460.5	477.5
(8, 5)	0.902	260.4	22.41	505.6	492.5	503.2
(12, 0)	0.953	247.1	0.00	526.0	571.9	501.2
(7, 7)	**0.963**	**244.7**	**30.00**	**530.1**		
(11, 2)	0.963	244.7	8.21	530.1	569.7	510.6
(10, 4)	0.992	237.9	16.10	541.9	526.8	538.2
(9, 6)	1.038	227.8	23.41	561.2	578.9	556.4
(13, 1)	1.074	220.6	3.67	576.1	576.8	576.1
(12, 3)	1.091	217.3	10.89	583.5	595.4	581.2
(8, 8)	**1.100**	**215.7**	**30.00**	**587.1**		
(11, 5)	1.126	211.1	17.78	598.0	562.4	573.8
(10, 7)	1.175	202.7	24.18	619.1	585.5	596.8
(15, 0)	1.191	200.2	0.00	625.9	665.0	601.8
(14, 2)	1.199	198.9	6.59	629.3	652.6	620.1
(13, 4)	1.222	195.4	13.00	639.5	648.9	637.9
(9, 9)	**1.238**	**193.1**	**30.00**	**646.2**		
(12, 6)	1.260	189.8	19.11	656.1	682.7	643.5
(11, 8)	1.312	182.9	24.79	678.6	697.3	672.0
(16, 1)	1.312	182.9	3.00	678.6	647.9	658.4
(15, 3)	1.326	181.0	8.95	684.9	680.0	684.4
(14, 5)	1.354	177.5	14.70	697.3	733.4	673.8
(10, 10)	**1.375**	**175.0**	**30.00**	**706.5**		
(13, 7)	1.396	172.6	20.17	715.6	693.3	704.6
(18, 0)	1.429	168.9	0.00	730.5	766.0	706.7
(17, 2)	1.436	168.2	5.50	733.4	710.2	721.2
(12, 9)	1.449	166.8	25.28	739.3	770.8	720.0
(16, 4)	1.455	166.1	10.89	742.2	752.5	740.0
(15, 6)	1.487	162.8	16.10	756.6	744.2	753.1

Table 4 (CONT'D)

(n, m)	dt(nm)	ω(cm-1)	θ(deg)	λ11(nm)	λ11+(nm)	λ11-(nm)
(11, 11)	**1.513**	**160.3**	**30.00**	**767.9**		
(14, 8)	1.531	158.5	21.05	776.3	808.8	754.8
(19, 1)	1.550	156.7	2.54	784.6	792.0	783.3
(18, 3)	1.562	155.6	7.59	790.0	767.3	777.7
(13, 10)	1.586	153.4	25.69	800.9	797.3	800.6
(17, 5)	1.586	153.4	12.52	800.9	834.5	777.6
(16, 7)	1.621	150.4	17.27	816.9	817.8	816.9
(12, 12)	**1.650**	**147.9**	**30.00**	**830.0**		
(15, 9)	1.667	146.6	21.79	837.8	812.3	821.7
(20, 2)	1.673	146.1	4.72	840.3	840.1	840.3
(19, 4)	1.690	144.8	9.37	848.0	817.7	824.9
(18, 6)	1.717	142.6	13.90	860.6	840.2	850.2
(14, 11)	1.723	142.2	26.04	863.1	835.2	843.4
(17, 8)	1.756	139.8	18.26	878.0	871.7	877.0
(13, 13)	**1.788**	**137.5**	**30.00**	**892.7**		
(16, 10)	1.803	136.4	22.41	899.9	890.4	897.6
(20, 5)	1.819	135.4	10.89	907.1	916.6	904.8
(19, 7)	1.850	133.3	15.08	921.2	931.0	918.9
(15, 12)	1.860	132.6	26.33	925.9	898.7	906.5
(18, 9)	1.890	130.7	19.11	939.8	962.5	927.4
(14, 14)	**1.925**	**128.6**	**30.00**	**955.8**		
(17, 11)	1.940	127.7	22.95	962.5	993.1	940.5
(20, 8)	1.983	125.2	16.10	982.5	971.1	979.0
(16, 13)	1.997	124.4	26.58	989.1	978.3	986.0
(19, 10)	2.026	122.8	19.84	1002.1	973.0	979.0
(15, 15)	**2.063**	**120.9**	**30.00**	**1019.2**		
(18, 12)	2.076	120.1	23.41	1025.6	1038.8	1021.1
(17, 14)	2.135	117.2	26.80	1052.6	1061.4	1050.5
(20, 11)	2.161	115.9	20.48	1064.9	1070.6	1064.0
(16, 16)	**2.200**	**114.1**	**30.00**	**1083.0**		
(19, 13)	2.213	113.5	23.82	1089.0	1068.4	1077.1
(18, 15)	2.272	110.9	27.00	1116.4	1139.7	1102.2
(17, 17)	**2.338**	**108.1**	**30.00**	**1147.0**		
(20, 14)	2.350	107.6	24.18	1152.6	1125.0	1130.7
(19, 16)	2.409	105.3	27.17	1180.4	1210.0	1157.3
(18, 18)	**2.475**	**102.8**	**30.00**	**1211.2**		
(20, 17)	2.547	100.3	27.32	1244.6	1273.2	1222.5
(19, 19)	**2.613**	**98.0**	**30.00**	**1275.5**		
(20, 20)	**2.750**	**93.8**	**30.00**	**1340.0**		

References

[1] http://www.wooster.edu/chemistry/is/brubaker/uv/default.html.

[2] M.E. Itkis, F. Borondics, A. Yu, R.C. Haddon, Bolometric Infrared Photoresponse of Suspended Single-Walled Carbon Nanotube Films, Science, 312, 413 (2006).

[3] R. Saito, G. Dresselhaus, M.S. Dresselhaus, Physical Properties of Carbon Nanotubes, Imperial College: London, (1998).

[4] S.M. Bachilo, M.S. Strano, C. Kittrell, R.H. Hauge, R.E. Smalley, R.B. Weisman, Structure-Assigned Optical Spectra of Single-Walled Carbon Nanotubes, Science, 298, 2361, (2002).

[5] M.E. Itkis, S. Niyogi, M.E. Meng, M.A. Hamon, H. Hu, R.C. Haddon, Spectroscopic Study of the Fermi Level Electronic Structure of Single-Walled Carbon Nanotubes, Nano Lett., 2, 155 (2002).

[6] M.S. Strano, C.A. Dyke, M.L. Usrey, P.W. Barone, M.J. Allen, H. Shan, C. Kittrell, R.H. Huge, J.M. Tour, R.E. Smalley, Electronic Structure Control of Single-Walled Carbon Nanotube Functionalization, Science, 301, 1519 (2003).

[7] R. Singh, C. V. Raman and the Discovery of the Raman Effect, Phys. Perspect., 4, 399 (2002).

[8] J.J. Laserna, Ed., Modern Techniques in Raman Spectroscopy, John Wiley & Son Ltd, England (1996).

[9] P.-H. Tan, S. Dimovski, Y. Gogotsi, Raman Scattering of Non-Planar Graphite: Arched Edges, Polyhedral Crystals, Whiskers and Cones, Phil. Trans. R. Soc. Lond.A, 362, 2289 (2004).

[10] R. Atta-Fynn, P. Biswas, D. A. Drabold, Electron–Phonon Coupling is Large for Localized States, Phys. Rev. B, 69, 245204 (2004).

[11] T. Hertel, G. Moos, Electron-Phonon Interaction in Single-Walled Carbon Nanotubes: A Time-Domain Study, Phys. Rev. Lett., 84, 5002 (2000).

[12] M.S. Dresselhaus, G. Dresselhaus, R. Saito, A. Jorio, Raman Spectroscopy of Carbon Nanotubes, Phys. Rep., 409, 47 (2005).

[13] A. Jorio, R. Saito, J.H. Hafner, C.M. Lieber, M. Hunter, T. McClure, G. Dresselhaus, M.S. Dresselhaus, Structural (n, m) Determination of Isolated Single-Walled Carbon Nanotubes by Resonant Raman Scattering, Phys. Rev. Lett., 86, 1118 (2001).

[14] A. M. Rao, J. Chen, E. Richter, U. Schlecht, P. C. Eklund, R. C. Haddon, U. D. Venkateswaran, Y.-K. Kwon, D. Tománek, Effect of van der Waals Interactions on the Raman Modes in Single-Walled Carbon Nanotubes, Phys. Rev. Lett., 86, 3895 (2001).

[15] M.S. Dresselhaus, G. Dresselhaus, A. Jorio, A.G. Souza Filho, R. Saito, Raman Spectroscopy on Isolated Single Walled Carbon Nanotubes, Carbon, 40, 2043 (2002).

[16] A. Jorio, A.G. Souza Filho, G. Dresselhaus, M.S. Dresselhaus, A.K. Swan, M.S. Ünlü, B.B. Goldberg, M.A. Pimenta, J.H. Hafner, C.M. Lieber, R. Saito, G-Band Resonant Raman Study of 62 Isolated Single-Walled Carbon Nanotubes, Phys. Rev. B, 65, 155412 (2002).

[17] R. Saito, A. Grüneis, G.G. Samsonidze, V.W. Brar, G. Dresselhaus, M.S. Dresselhaus, A. Jorio, L.G. Cançado, C. Fantini, M.A. Pimenta, A.G.S. Filho, Double Resonance Raman Spectroscopy of Single-Walled Carbon Nanotubes, New J. Phys., 5, 157.1 (2003).

[18] M.A. Hamon, M.E. Itkis, S. Niyogi, T. Alvaraez, C. Kuper, M. Menon, R.C. Haddon, Effect of Rehybridization on the Electronic Structure of Single-Walled Carbon Nanotubes, J. Am. Chem. Soc., 123, 11292 (2001).

[19] D. Chattopadhyay, I. Galeska, F. Papadimitrakopoulos, A Route for Bulk Separation of Semiconducting from Metallic Single-Walled Carbon Nanotubes, J. Am. Chem. Soc., 125, 3370 (2003).

[20] R. Saito, G. Dresselhaus, M.S. Dresselhaus, Trigonal Warping Effect of Carbon Nanotubes, Phys. Rev. B, 61, 2981 (2000).

[21] Y. Lian, Y. Maeda, T. Wakahara, T. Akasaka, S. Kazaoui, N. Minami, N. Choi, H. Tokumoto, Assignment of the Fine Structure in the Optical Absorption Spectra of Soluble Single-Walled Carbon Nanotubes, J. Phys. Chem. B, 107, 12082 (2003).

[22] R.B. Weisman, S.M. Bachilo, Dependence of Optical Transition Energies on Structure for Single-Walled Carbon Nanotubes in Aqueous Suspension: An Empirical Kataura Plot, Nano. Lett., 3, 1235 (2003).

[23] R. Saito, M. Fujita, G. Dresselhaus, M.S. Dresselhaus, Electronic Structure of Chiral Graphene Tubules, Appl. Phys. Lett., 60, 2204 (1992).

[24] A.M. Rao, E. Richter, S. Bandow, B. Chase, P.C. Eklund, K.A. Williams, S. Fang, K.R. Subbaswamy, M. Menon, A. Thess, R.E. Smalley, G. Dresselhaus, M.S. Dresselhaus, Diameter-Selective Raman Scattering from Vibrational Modes in Carbon Nanotubes, Science, 275, 187 (1997).

[25] J.W. Mintmire, C.T. White, Universal Density of States for Carbon Nanotubes, Phys. Rev. Lett., 81, 2506-2509 (1998).

[26] M.S. Strano, S.K. Doorn, E.H. Haroz, C. Kittrell, R.H. Hauge, R.E. Smalley, Assignment of (n, m) Raman and Optical Features of Metallic Single-Walled Carbon Nanotubes, Nano. Lett., 3, 1091 (2003).

[27] S. Reich, C. Thomsen, Chirality Dependence of the Density-Of-States Singularities in Carbon Nanotubes, Phys. Rev. B, 62, 4273 (2000).

[28] M.S. Dresselhaus, P.C. Eklund, Phonons in Carbon Nanotubes, Adv. Phys., 49, 705 (2000).

3

Synthesis of Single-Walled Carbon Nanotubes

Finding different methods to controllably grow carbon nanotubes still remains a challenge. Controlling the number of shells (e.g. single, double, or multi-walled carbon nanotubes) to match the requirements for diverse applications needs a lot of effort. Yet another challenge is the production of materials with sufficient purity – precluding the need for complex and potentially damaging post-synthesis purification products. How to produce enough amounts of tubes to off set the cost of purchased materials? Different methods to synthesize carbon nanotubes are briefly introduced in this chapter.

Carbon nanotubes are characterized by very distinctive electronic properties along with exceptional mechanical strength. Despite the remarkable properties of CNTs, the production of bulk quantities of purified CNTs still remains a challenge. There is still much that remains to be done to improve the synthesis methods employed to produce CNTs. The goal is to reduce the time required to synthesize CNTs, increase the amount of products, control the end products, and eliminate the unwanted catalysts. In this chapter, the traditional methods used to grow CNTs will be introduced. Subsequently, an experimental modification of the chemical vapor deposition (CVD) method is demonstrated for the synthesis of carbon nanotubes. This method involves the direct thermal decomposition of ethanol in a stainless-steel reaction chamber under high pressure.

The results from CVD growth of CNTs will be discussed in detail; with the resulting CNTs have been characterized by Raman spectroscopy, thermogravimetric analysis (TGA), and transmission electron microscopy (TEM).

3.1 Introduction

CNTs are one of the most promising materials to have been developed over the last decade. However, for the integration of CNTs in many practical applications, it is important to develop methods to manufacture high-quality nanotubes in large quantities.

Although many new and improved techniques have been reported for producing significant amounts of different types of CNTs (e.g. ternary BCN nanotubes [1]), the synthesized products can be divided into three major classes. These three major techniques are arc-discharge evaporation, pulsed laser ablation, and chemical vapor deposition (CVD). The HiPco method, which involves the high-pressure decomposition of CO over in situ generated Fe catalysts, is a popular embodiment of the CVD technique. Most of these procedures require a high vacuum, but CVD can be run in vacuum or at atmospheric pressure.

There is much that still remains unknown about the growth mechanism and the formation of the nanotubes. There might be more than one mechanism operating during the synthesis of CNTs. In general, the carbon precursor is decomposited at high temperatures and dissolves in the transition-metal nanoparticle. Eventually, the nanoparticles become supersaturated with carbon and at a C composition depending on the entities of the C-metal binary mixture. Carbon nanotubes or nanofibers start to crystallize from the nanoparticles. Nanoparticles are used because of their relatively low melting points which allows for operation at relatively low temperatures.

Sinnot and co-workers [2] reported two feasible schematic mechanisms, growth along the side of metal catalyst (also called root or extrusion growth) or growth at the base of the metal catalyst (also called tip growth), for synthesizing carbon nanotubes shown in Figure 3-1. According to the root-growth (base growth or extrusion) model, the metal catalyst particles (Ni, Co, Fe, or combination) are present on the supporting substrate, and the carbon source, as carbide particles, forms a wall of rod-like carbon tubes on the top surface of the metal particles. Carbon nanotubes then grow in the upward

direction. According to the tip-grow model (called base growth in carbon nanotubes as viewed from the growing point), the catalyst particles are detached from the substrate, and act as leading guides for the tube to grow as the precursor gas carries it along the CVD chamber. To determine if the products are single-walled or multi-walled CNTs, the diameter of catalysts are the key. The number of walls is controlled by the diameter of the catalyst.

Arc discharge or laser ablation produces relatively less defective carbon nanotubes than chemical vapor deposition. On the other hand, CVD can produce large amounts of tubes but the products contain much more defective tubes than other growth methods. For applications requiring high quality tubes, arc discharge or laser ablation techniques are ideal. However, for application requiring large quantities of carbon nanotubes, the CVD method represents a promising alternative.

3.1.1 Arc Discharge

In 1991, multi-walled carbon nanotubes were first produced by using arc-discharge evaporation [3]. This method is, however, relevant primarily in academic laboratories due to its simplicity of operation. Additionally, it is the cheapest prepared way to obtain significant amounts of SWNTs even though as-produced SWNTs by arc discharge are less pure than these produced by laser ablation. SWNTs were first prepared in 1993 [4] by DC arc discharge which is essentially a modification of the method used to synthesize C_{60} fullerenes [5].

The basic experimental setup for arc discharge is depicted in Figure 3-2. The diagram shows that the main components of the arc discharge apparatus are the two

opposite by charged electrodes (6-12 mm in diameter), two graphite rods (carbon source), catalyst seeds, the circuit power supply, and the atmosphere. Two graphitic carbon rods are connected to the positive and negative electrodes and placed end to end separated by approximately 1-4 mm, this distance is controlled by a gap adjuster. The graphite rod connected to the anode is filled with graphite powder deposited with catalytic metals such as Fe, Ni, and Co or alloy. These two consumable graphite rods serve as the carbon source when the circuit is discharged and nanotubes are found in the carbon soot that is produced around the puncture hole where the catalysts are present. A stepper motor is used to advance the consumable rod to prevent the gap from increasing. The arc discharge technique can also be operated under different atmosphere. For examples, SWNTs can be prepared using Ni/Y under a helium [6] atmosphere or Ni/Co under a nitrogen [7] ambient. This method is still being required to solve the problem appertaining to the high ratio of metal catalysts and amorphous carbon in the end product. Arc discharge can be achieved using either an AC (alternative current) or DC (direct current) arc power supply. For DC arc discharge, the gap voltage across the gap and the power are constant. DC arcs provide higher yields of nanotubes than AC arc discharge.

In the arc discharge system, multi-walled carbon nanotubes are deposited on the cathode, but SWNTs are found in the chamber soot. Therefore, arc discharge can produce high yields of SWNTs. To produce SWNTs, right kind of catalyst has to be used. Alloy catalysts (bi-metallic catalysts) produce a higher yield of SWNTs than catalysts composed of only one metal [8], the catalysts are filled into the hole located in the graphitic carbon rod on the anode side. The weight ratio of metals also affects the yield of SWNTs. Even though many parameters need to be optimized to control the yield, purity,

and number of walls in the product, arc discharge remains a useful method for producing large amounts of SWNTs. Nevertheless, the high amount of impurities present in the products and the difficulties involved in purified CNTs has lead to the increasing popularity of other synthesized methods.

3.1.2 Laser Ablation

Laser ablation (or laser vaporization) was used to produce copper clusters in 1982 [9] and C_{60} fullerene in 1985 [5] by Smalley's group. Since the boiling point for carbon is very high about 4827°C, and the laser energy density is much higher than achievable by most other sources, laser ablation can be useful for growing carbon nanotubes. The obtained yield of CNTs was minimal until Smalley and group came up with a modification involving the combination of the laser-oven method with an annealing system (1200°C) to produce C_{28} fullerenes [10]. The use of laser ablation or pulsed laser vaporization (PLV) to synthesize SWNTs was reported by Guo et al. in 1995 [11] and by the Thess group in 1996 [12].

The schematic of the laser ablation setup is shown in Figure 3-3. The major components of the PLV system include a furnace, a quartz tube, a target graphitic carbon rod with embedded catalyst, a water cooling controller, pressure and flow rate control system, an argon gas tank, and a laser (typical Nd:YAG) source. Nanotubes are synthesized by pulsed Nd:YAG laser ablation of graphite targets in a high-temperature furnace at about 1200°C; an inert gas (Ar) flow is maintained in the chamber at 1 cm/s rate with a typical pressure of 500 Torr [13]. The vaporized carbon forms a very hot vapor path, expands, and then cools rapidly; the formed tubes develop and condense on

the cooler surfaces of the reactor. To collect the CNT samples, a water-cooled surface is needed.

The laser ablation method has many advantages. In this technique, high-quality SWNTs are produced in large quantities with controllable diameters. Although the SWNTs are of high quality, samples contain many impurities then can be quite difficult to remove. Recently, it has been possible to obtain high quality SWNTs with a relatively low density of defects and with controlled diameter by precisely adjust furnace temperature; post-synthesis purification protocols have also been developed to remove contaminants such as the metal catalysts [14]. In the PLV method, the resulting amorphous carbon is more homogenously spread than in the arc-discharge method. A longer pulse duration will lead to the laser energy density and vaporization temperature to become low, and it is essential for the growth of single-walled carbon nano-horns (SWNHs) using CO_2 as laser energy source [15]. In this report, catalysts were eliminated in the synthesis process. This is one of the attractions for using laser ablation technique to grow various new nanomaterials, and it may possibly become a powerful tool for nanotechnology in the twenty-first century. Laser ablation may thus become a powerful tool for nanotechnology in the twenty-first century.

3.1.3 Chemical Vapor Deposition

Chemical vapor deposition (CVD) is one of the most important methods for synthesizing carbon nanotubes. Carbon nanotubes were produced by CVD involving the thermal decomposition of hydrocarbon vapor over a transition metal catalyst in 1993 [16], notably CVD methods were used to produce CNTs in 1959 [17] but the products were

not identified as such. CVD has later been used to synthesize large scale aligned CNTs in 1996 [18]. Using CVD method to produce carbon nanotubes has several advantages. Compared with arc-discharge and laser ablation methods, a CVD setup is experimentally simpler to assemble and operate. Three main parameters need to be adjusted for the CVD growth of nanotubes: the hydrocarbons (which function as the carbon source), the catalyst (which mediates the decomposition of the hydrocarbons at low temperatures), and the reaction temperatures.

In general, nanotubes are grown from nucleation sites of catalysts in carbon based gas environments at elevated temperatures (ca 600 – 1000 °C). Temperature is an important parameter in CVD that affects the quality of the product and determines whether the tubes are single-walled (900-1200 °C) or multi-walled (600-900 °C). At low temperatures, CVD results in the formation of MWNTs from most hydrocarbon gas sources. On the other hand, SWNTs are produced at relatively high temperature. This result suggests that SWNTs have a higher energy and a higher strain of formation. The carbon source f can be ethylene, methane, or other similar hydrocarbon. As mentioned above, MWNTs can be synthesized from most of the hydrocarbon precursors because of the low temperature involved. However, at the higher temperature required to synthesize SWNTs, most hydrocarbons tend to "crack" and therefore more stable precursors such as CO or CH_4 are required. A quartz boat or substrate is placed with metal catalyst particles (Ni, Co, Fe) or alloy particles. Nanoparticle catalysts are required to catalyze the formation of carbon nanotubes. One of the advantages of CVD methods using nanoparticle catalysts is the ability to control the diameter of the nanotubes [19]. The overall benefit of the CVD method is that it is a less time-consuming and more

economical technique that can be carried out at lower temperatures and ambient pressure. Since the growth of CNTs relies upon the precise preparation of nanoparticle catalysts, this condition limits the mass production of CNTs. However, the CVD process can be used to grow CNTs on substrates, as well as to align CNTs in arrays and assembles, which is not possible with either arc-discharge or laser ablation. This is especially useful for applications. Terrones et al. [20] have produced aligned arrays of nanotubes with nearly no by-products, Pan et al. [21] have been successful in growing very long nanotubes (ca. 2 mm in length); whether Wei et al. [22] have produced organized assemblies of CNTs on Si wafers.

As mentioned before, the major draw back of using CVD is the amounts produced. A lot of expense will be increased in using catalysts to grow large quantities of carbon nanotubes. There is a more cost-effective approach for synthesizing CNTs that involves using metallic catalysts generated from the steel industry. The steel manufacturing process creates large amounts of side products that can be used as catalyst for growing carbon nanotubes. Several research groups have demonstrated the formation of well-aligned carbon nanotubes on stainless steel grids by CVD methods. In particular, Wal and Hall [23] have reported the effects of various pretreatments on grids made of type 304 stainless-steel mesh (diameter of wire is 0.0009 inch) upon flowing various reactive gas mixtures inside the CVD system for growth of CNTs. The model for this system is called carbon solvation, diffusion, and precipitation (CSDP). The synthesis of nanotubes using type 304 stainless steel has been further developed using CH_4/CO_2 in a microwave plasma chemical vapor deposition [24]. Applying the microwave plasma CVD technique, aligned carbon nanotubes have been obtained which are used to study field emission

properties. Apart from the use of stainless steel mesh, Liu et al. [25] have reported a new process that produces CNTs in large quantities called ethanol thermal reduction process. In this process, ethanol is used as the carbon source and Mg as the reducing agent (reductant) in a stainless steel autoclave at a temperature of 600 °C. This ethanol thermal reduction process yields a bamboo-shaped and also a few Y-junction multi-walled carbon nanotubes.

A much simpler method for the CVD growth of CNTs has been reported by our group [26]. In our process, no catalytic metal nanoparticles or reducing agents are required. The preparation of metallic catalysts is completely eliminated in our experiment, and stainless steel is instead used as an intrinsic catalyst. In this simplified construction, the temperature and pressure can be optimized quickly by rapidly screening the products.

3.1.4 High Pressure Carbon Monoxide Conversion

The HiPco process developed at Rice University [27] involves the thermal decomposition of iron pentacarbonyl in a CO flow reactor at high pressures of 1-10 atm and temperatures ranging from 800-1200 °C. $Fe(CO)_5$ is used as the iron catalyst precursor source, whereas the carbon feedstock source is flowing CO gas. The decomposition of iron precursors leads to the formation of metallic cluster, and these cluster products serve as catalysts for growing SWNTs. The cluster catalysts enhance the disproportionation of CO molecules into C atoms and accelerate SWNTs growth. Essentially the process is the Boudard reaction, $CO + CO \xrightarrow{Fe} C + CO_2$. These HiPco samples are particularly well characterized with respect to their optical properties. HiPco technique was a successful achievement of modification of CVD that can produce large

quantities of small diameter (0.7 nm) single-walled carbon nanotubes. The diameter distribution of SWNTs grown by this method is from 0.7 to 1.1 nm.

3.2 Experiments

Here, we investigate the synthesis of CNTs via thermal decomposition. Instead of using nanoparticles as catalysts, highly alloyed 316-type stainless steel (18Cr10Ni2Mo) cylindrical tubes mounted inside the furnace are used as both the reactor and the catalyst for the synthesis of tubes. Ethanol is used as the carbon source. About 5 mL of highly purified ethanol is loaded into a small boat. The ethanol-loaded-boat is then placed inside a clean, meter-long 316-type stainless steel tube that is moved into the heated central region of the furnace. Highly purified argon gas is used to purge the reaction chamber for more than 30 minutes to remove air from the steel tube; argon gas is then filled to a given pressure ranging typically from 5 to 10 atm. Subsequently, the stainless steel tube is sealed. The temperature within the reaction chamber is gradually increased to the desired final temperature in the range of ~ 600-900 °C. The pressure within the chamber is kept constant by varying the pressure of argon gas. The reaction is carried out for a period 0.5 to 2 h. At the end of the reaction, the formed products are left in the still sealed stainless steel tube during cool-down to room temperature. Within the chamber, a black, hair-like powdered carbon material is obtained. The products are occurred from the system by brushing the inner surface of the stainless steel tube with a solid glass rod.

To probe the obtained carbon material, electron microscopy (TEM), vibrational spectroscopy (Raman), and thermalgravimetric analysis (TGA) have been employed. TEM measurements of the morphologies of the as-synthesized carbon nanotubes were acquired using a Philips CM120 TEM equipped with a LaB_6 filament. The TEM samples were prepared by placing one drop of the as-produced carbon nanotubes dispersed in sodium dodecylbenzenesulfonic acid (SDBS) aqueous solution on a copper grid, and then

evaporating the solvent. Raman spectra were acquired with a LabRam (J-Y Instruments) Raman spectrometer using a 632 nm radiation to excite solid samples placed on a silicon wafer substrate. Thermogravimetric (TG) analysis was executed on a Universal V3.5B TA Instrument Thermal Analyzer from room temperature to ca. 1000 °C, and the heating rate was 10 ºC/min with 100 mL/min nitrogen atmosphere flow rate.

3.3 Results and Discussion

Figure 3-5 shows Raman spectra of carbon nanotubes grown on a stainless steel tube by direct decomposition of ethanol in the central zone of the furnace at 750 ºC with pressures of 7.5 and of 1 atm in curves A and B, respectively. The Raman spectra display two sharp peaks corresponding to the D- and G-bands that are characteristic of carbon nanotubes [28]. The band at ca. 1572 cm^{-1} is assigned to the first-order 2D graphitic (i.e., G-band) peak of ordered carbon. The relative intensity of the G band for CNTs grown at 1 atm is lower than for CNTs grown at 7.5 atm. The Raman band at 1325 cm^{-1} is associated with the amount of defective disorder-induced carbon on the surface of the carbon nanotubes. As-prepared CNTs grown at high and low pressures display strong peaks corresponding to defects and disordered carbon. The Raman G′ bands located at ca. 2656 and 2875 cm^{-1} are assignable to the overtone of the D-band (i.e., ca. 2×1325 cm^{-1}) and the combination band of the G- and D-bands, respectively. One reaction of the qualities of the nanotubes is the ratio of the intensities of the G and D peak for CNTs grown at different pressures. Figure 3-5, comparing the relative G/D intensity ratio for the as-grown carbon nanotubes samples, one can conclude that the degree of graphitization is higher for samples synthesized under high-pressure at 7.5 atm than for samples synthesized at a pressure 1 atm.

Figure 3-6 shows TEM images of CNTs grown on the surface of a stainless steel tube by direct decomposition of ethanol at 750 ºC at pressures of 7.5 and 1 atm. Several different MWNTs can be clearly seen in the TEM images for tubes grown at 7.5 atm. In Figure 3-6A, the TEM shows a linear, open-ended CNT with an outer diameter of ca. 26 nm and an inner diameter of ca. 14 nm, clearly indicating that the end products are multi-

walled nanotubes. Figure 3-6B and C show bamboo-type MWNTs with outer and inner diameters of ca. 30 and 22 nm, respectively. Similar bamboo-shaped carbon nanotubes have been reported in studies by others [29]. In Figure 3-6D, a spiral shaped MWNT is shown; such structures have also been described by Ajayan et al. [30]. Branched Y-shaped and saw-toothed W-shaped carbon nanotubes are shown in Figure 3-6E, Xu et al. [31] and Rao et al. [32] have reported a special setup for growing Y-shaped carbon nanotubes, since these structures are potentially useful as new materials for nanoscale wiring and electronic circuitry. TEM observations of carbon nanotubes grown at nearly atmospheric pressure show the formation of a few MWNTs. Panel G of Figure 3-6 shows a typical straight CNT synthesized at 1 atm pressure with outer and inner diameters of ca. 60 and ca. 10 nm, respectively. CNTs synthesized at this lower pressure do not exhibit the diverse morphologies found in CNT sample synthesized at high pressures.

Thermogravimetric analysis (TGA) and derivative thermogravimetric analysis (DTA) of CNTs grown at a pressure of 7.5 atm are shown in Figure 3-7. TG thermal decomposition curves (also called thermograms) provide helpful information about decomposition mechanisms for the preparation of carbon nanotubes. An initial 3 wt. % loss is observed for the sample from ambient temperature to ca. 200 °C, which can be reasonably attributed to the removal of physisorbed water and the burning of disordered carbon. There is a ca. 90 wt. % weight loss between 525 and 700 °C, which can be attributed to the oxidation of carbon nanotubes into CO_2. The total weight loss up to a temperature of 525 °C is less than 4 wt. %, suggesting that the amount of disordered carbon contained in our sample is very low. The residue present after the complete oxidation of the carbon species is ca. 7.0 wt. % of the original sample, which is lower

than generally found for samples prepared by CVD or carbon arc discharge methods. The derivative of the thermogram can sometimes reveal information that is unclear from the TG thermogram. Indeed, the DTA curve shows three peaks, as shown in Figure 3-7. The three peaks (with maximum weight loss per degree occurring at 638.1 °C) suggest that there are at least three carbon components within this sample; this is consistent with TEM measurements showing the presence of several types of CNTs.

It is widely believed that the development of different processes to produce different shapes of carbon nanotubes is important for the advancement of the field of nanoelectronics [31, 33]. For example, branched carbon nanotubes may be useful as building blocks or connections in nanoelectronic circuits. In general, it is not easy to reproducibly grow junction carbon nanotubes by conventional syntheses methods. However, many branched and saw-toothed carbon nanotube structure are found in our samples prepared by the thermal decomposition of ethanol on type 316 stainless steel tube under high pressure. Additionally, since ethanol is produced in large quantities by the fermentation of sugar-containing crops, it is the use of ethanol for growing CNTs that is expected to be cost-effective.

In general, the temperature and pressure significantly affect the nature of the produced carbon nanotubes. The optimal conditions for the production of carbon nanotubes are temperatures ranging from 700 – 800 ºC and an applied total pressures in the range of 5 – 10 atm. In addition, other organic liquid carbon sources, such as methanol and benzene, can also be used for the high-pressure synthesis of CNTs instead of ethanol. From Raman spectra, we discover that it is possible to grow nanostructured carbon from these precursors; however, this process is yet to be optimized.

Based on a surface roughening (also referred to as surface "breakup") scheme, the CNT yield can be attributed to the supply of carbon atoms plus the number and size of catalytic sites; these two factors are critically important for the catalytic growth of nanotubes. This hypothesis is in accordance with the CSDP model put forth by other researchers [2, 23]. In other words, the growth of CNTs on stainless steel derives from the existence of large numbers of nanoscopic alloy sites and/or catalytic nanoparticles that originate from breaking and forming bonds at the surface of the substrate [23, 24]. The carbon atoms are thus produced via the catalytic decomposition of ethanol at the various catalytic sites. The process of forming CNTs involve the solvation of the carbon atoms in the metal; the carbon atoms then diffuse in the molten solvent and ultimately precipitate to form CNTs with a variety of morphologies. In our system, a sealed tube at a given temperature and pressure, the concentration of carbon reactants is expected to be high. Different sizes and shapes of catalytic sites are likely to form through breakup of the surface. When these two conditions, a high pressure and temperature, are met, carbon reactants are able to dissolve and interact with each other. On the other hand, sufficient quantities of the carbon reactants are not present at low pressures. Insufficient supply of carbon reactants will result in an inadequate number of carbon atoms at the various catalytic sites and slow down reaction between carbon atoms, resulting in a diminished number of CNT morphologies and low yields.

3.4 Conclusion

In this study of the synthesis of carbon nanotubes by CVD, it is essential to have a sufficient supply of reactive carbon, produced by the thermal decomposition of the carbon source. The presence of different catalytic particle sizes and shapes on the surface of stainless steel for the formation of carbon nanotubes with a wide variety of morphologies is also important. Ethanol is found to be a cost-effect carbon source. The as-synthesized CNTs are of high quality and exhibit low amorphous carbon content. The current method is a simple and economical approach for the synthesis of carbon nanotubes.

Nevertheless, the search continues for methods to controllably synthesize specific types of nanotubes with controllable chirality, length, and diameter. Thus far, these requirements have not yet been entirely achieved. However, basic growth methods have been developed. What is required is the modification of existing procedures. The ongoing efforts at refining the synthesis of CNTs are likely to result in the development of a standardized product for the controlled system of CNTs at commercially viable scales.

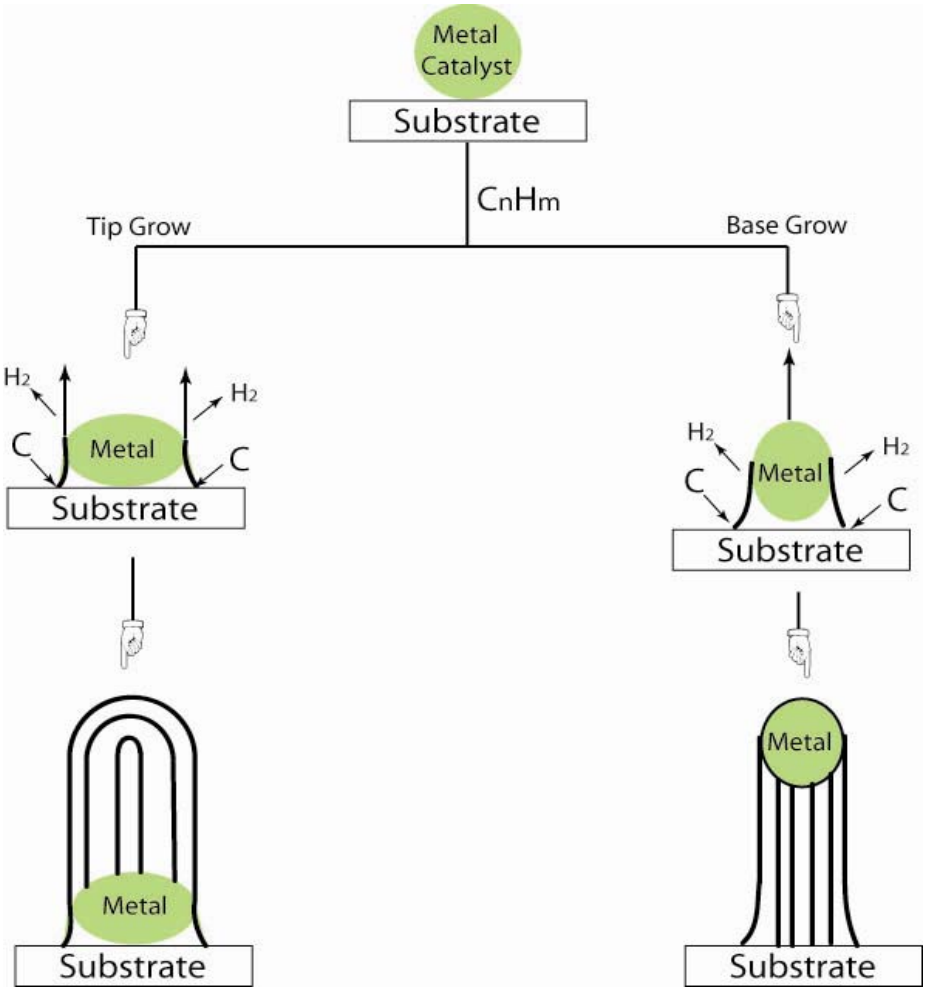

Figure 3-1 Depending on the growing direction of the nanotubes, two feasible mechanisms for CVD are suggested. On the left is the growth mechanism from the tip of the metal catalysts. On the right is the schematic for the growth mechanism from below the base of the metal catalysts.

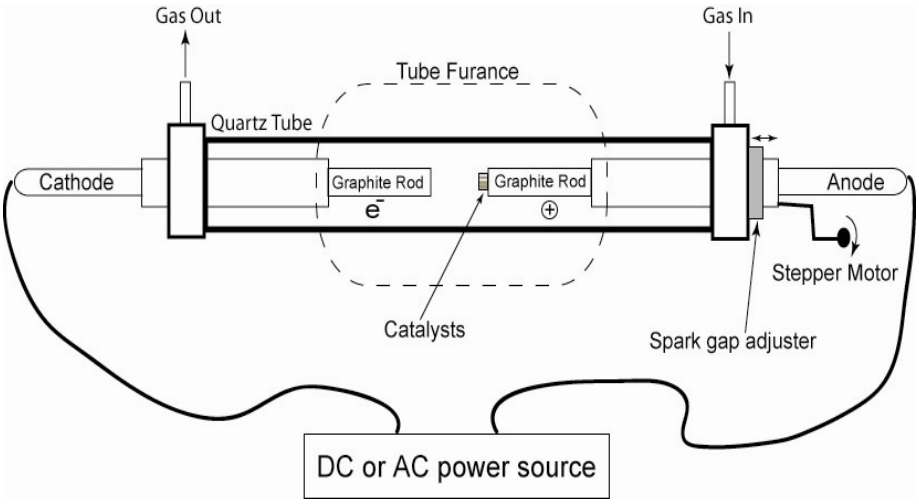

Figure 3-2 Arc discharge diagram. A positive electrode (cathode) and negative electrode (anode) are connected to a power source with either a DC or AC voltage arc discharge. Two graphite rods are connected with a positive charge (anode) and a negative charge (cathode). Carbon nanotubes are deposited on the cathode (MWNTs) or found in the chamber soot (SWNTs). Catalysts (individual or bimetallic) were deposited in a hole in the graphite rod connected to the anode. Gas flows into the inlet and leaves from the outlet. As adjuster or stepper motor is used to control the gap between two rods.

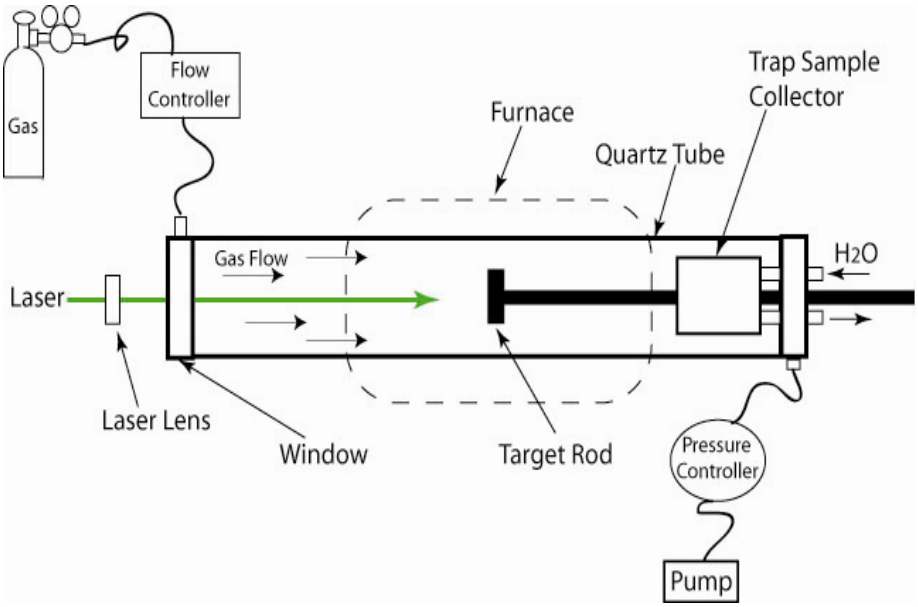

Figure 3-3 Laser Ablation or pulsed laser vaporization (PLV) diagram. The major components of a PLV system are a furnace, a quartz tube, a target carbon rod with catalyst, a water cooling controller, pressure and flow rate control system, an argon gas tank, and a laser beam (typically Nd:YAG laser) source.

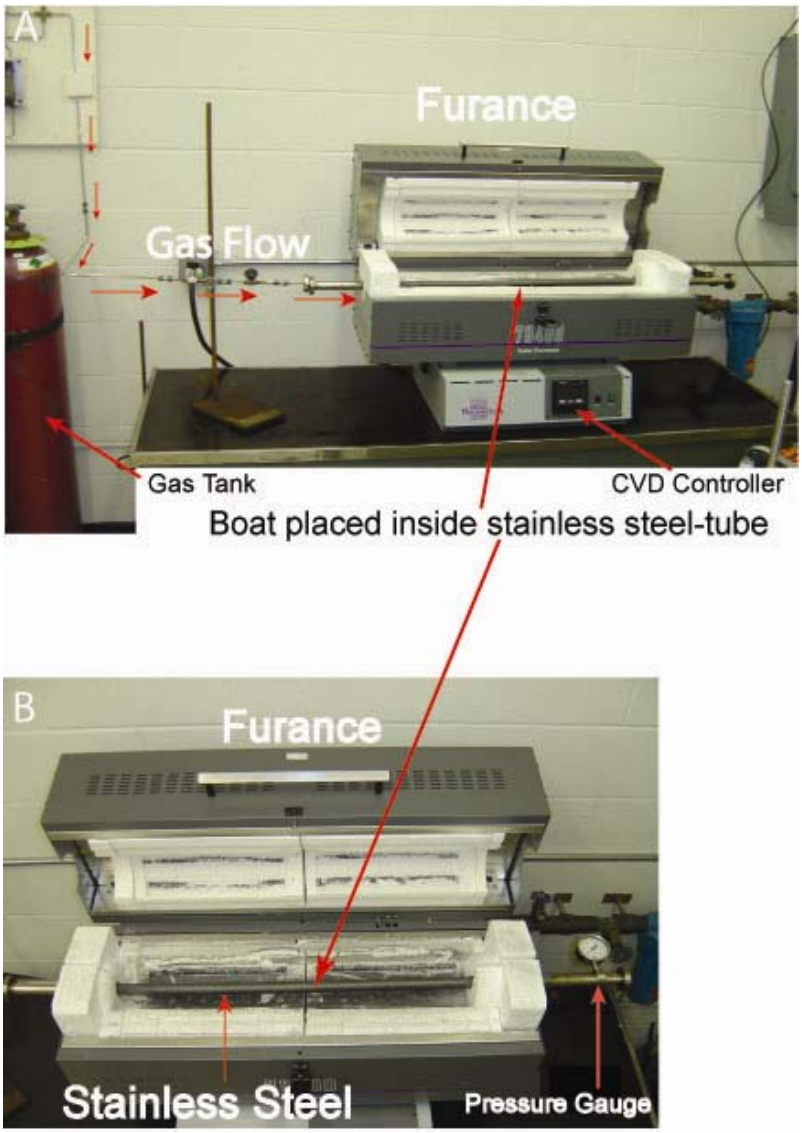

Figure 3-4 Chemical Vapor Deposition setup using 316-type stainless steel. The catalyst was replaced by stainless steel (18Cr10Ni2Mo) cylindrical tubes for the synthesis of carbon nanotubes. Ethanol used as the carbon source and was loaded into a small boat and placed inside the steel tubes. Argon is used to purge the chamber and is filled inside the steel tube. The temperature is controlled in the range from 600-900°C, and the pressure is varied from 5-10 atm.

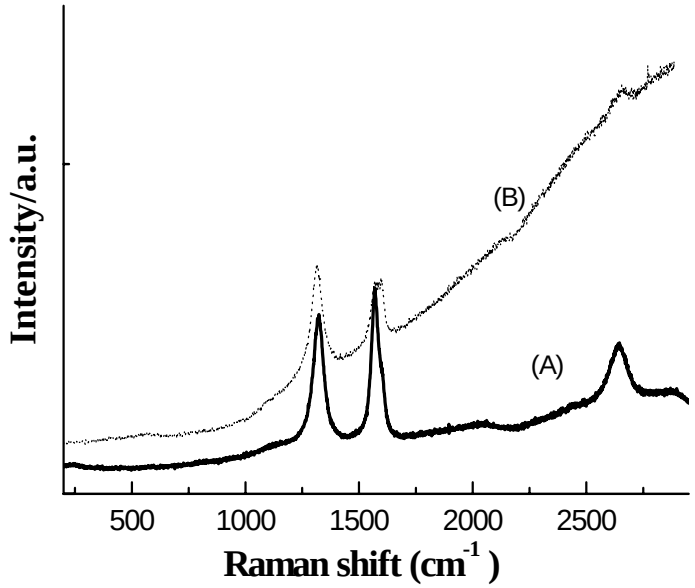

Figure 3-5 Typical Raman spectra of as-grown carbon nanotubes at 750 ^{o}C under pressures of (A) 7.5 atm and (B) 1 atm.

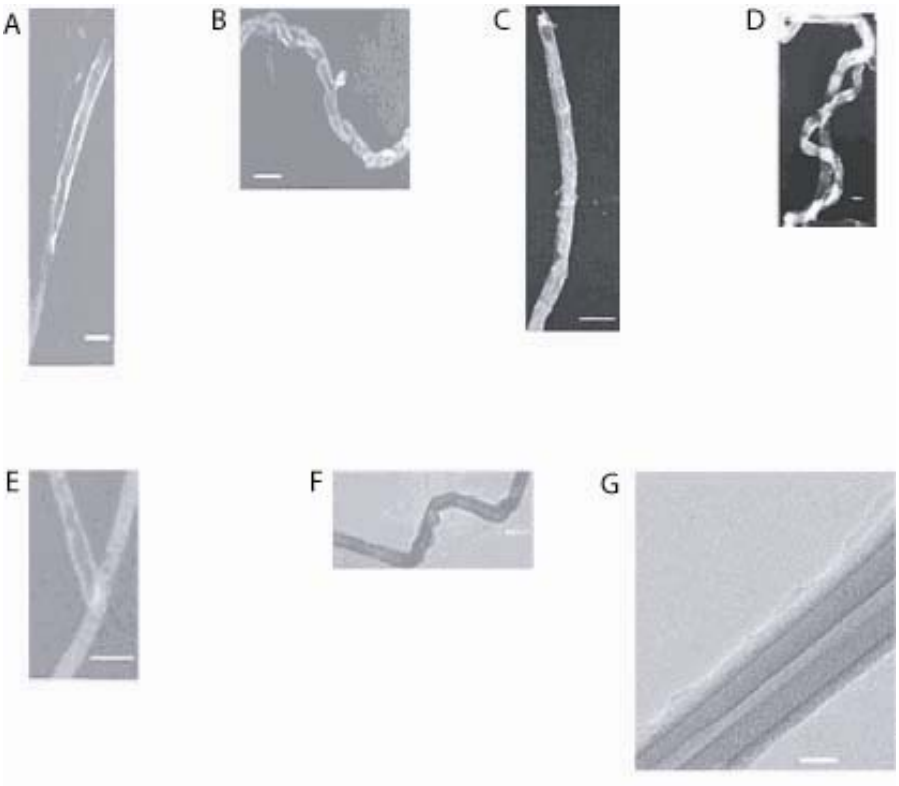

Figure 3-6 TEM images of as-grown CNTs formed by the decomposition of ethanol at 750 ºC; the synthesis pressure for the micrographs A through F is 7.5 atm; for G, the synthesis pressure is 1 atm. Part A shows a straight, open-ended CNT; the scale bar corresponds to 50 nm. The outer diameter is ca. 26 nm and the inner diameter is ca. 14 nm, indicating that the as-synthesized nanotubes are MWNTs. The TEM images in Part B and C (bar scale corresponds to 50 nm) are of bamboo-type MWNTs, with outer and inner diameters of ca. 30 and 22 nm, respectively. Part D (bar length corresponds to 50 nm) shows a spiral shaped MWNT, while Parts E (bar length corresponds to 100 nm) and F (bar length corresponds to 100 nm) show Y- and W-shaped MWNTs, respectively. It is to be noted that in Parts A, B, E, and F the brightness and contrast of the images have been modified since the nanostructures, in these images, were initially hard to discern due to lack of contrast. Part G shows a straight CNT; the scale bar corresponds to 50 nm).

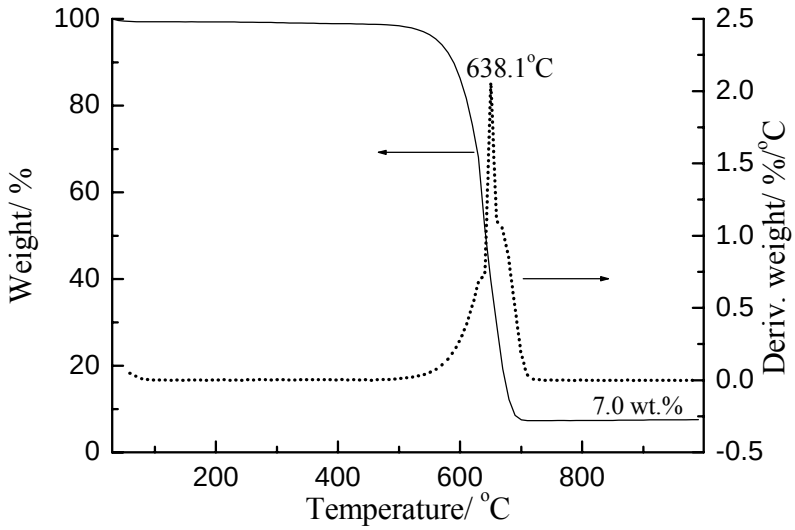

Figure 3-7 TG (solid) and DTA (dash) thermal decomposition curves of CNTs grown at 750 °C at a pressure of 7.5 atm.

References

[1] W.L. Wang, X.D. Bai, K.H. Liu, Z. Xu, D. Golberg, Y. Bando, E.G. Wang, Direct Synthesis of B-C-N Single-Walled Nanotubes by Bias-Assisted Hot Filament Chemical Vapor Deposition, J. Am. Chem. Soc., 128, 6530 (2006).

[2] S.B. Sinnott, R. Andrews, D. Qian, A.M. Rao, Z. Mao, E.C. Dickey, F. Derbyshire, Model of Carbon Nanotube Growth through Chemical Vapor Deposition, Chem. Phys. Lett., 315, 25 (1999).

[3] S. Iijima, Helical Microtubules of Graphitic Carbon, Nature, 354, 56 (1991).

[4] S. Iijima, T. Ichihashi, Single-Shell Carbon Nanotubes of 1-nm Diameter, Nature, 363, 603 (1993).

[5] H.W. Kroto, J.R. Heath, S.C. O'Brien, R.F. Curl, R.E. Smalley, C60: Buckminsterfullerene, Nature, 318, 162 (1985).

[6] C. Journet, W.K. Maser, P. Bernier, A. Loiseau, M. L. de la Chapelle, S. Lefrant, P. Deniard, R. Lee, J.E. Fisher, Large-Scale Production of Single-Walled Carbon Nanotubes by The Electric-Arc Technique, Nature 388, 756 (1997).

[7] Y. Makita, S. Suzuki, H. Kataura, Y. Achiba, Synthesis of Single Walled Carbon Nanotubes by using Arc Discharge Technique in Nitrogen Atmosphere, Eur. Phys. J. D 34, 287 (2005).

[8] S. Seraphin, D. Zhou, Single-Walled Carbon Nanotube Produced at High Yield by Mixed Catalysts, Appl. Phys. Lett., 64, 2087 (1994).

[9] D.E. Powers, S.G. Hamen, M.E. Geurlc, A.C. Puiu, J.B. Hopklns, T.G. Dletr, M.A. Duncan, P.R.R. Langrldge-Smith, R.E. Smalley, Supersonic Metal Cluster Beams: Laser Photoionization Studies of Cu2, J. Phys. Chem., 86, 2556 (1982).

[10] T. Guo, M.D. Diener, Y. Chai, M.J. Alford, R.E. Haufler, S.M. McClure, T. Ohno, J.H. Weaver, G.E. Scuseria, R.E. Smalley, Uranium Stabilization of C28: a Tetravalent Fullerene, Science, 257, 1661 (1992).

[11] T. Guo, P. Nikolaev, A. Thess, D.T. Colbert, R.E. Smalley, Catalytic Growth of Single-Walled Nanotubes by Laser Vaporization, Chem. Phys. Lett., 243, 49 (1995).

[12] A. Thess, R. Lee, P. Nikolaev, H. Dai, P. Petit, J. Robert, C. Xu, Y. H. Lee, S.G. Kim, A.G. Rinzler, D.T. Colbert, G.E. Scuseria, D. Tomanek, J.E. Fischer, R.E. Smalley, Crystalline Ropes of Metallic Carbon Nanotubes, Science, 273, 483 (1996).

[13] A.A. Puretzky, D.B. Geohegan, X. Fan, S.J. Pennycook, In Situ Imaging and Spectroscopy of Single-Walled Carbon Nanotube Synthesis by Laser Vaporization, Appl. Phys. Lett., 76, 182 (2000).

[14] H. Ishii, H. Kataura, H. Shiozawa, H. Yoshioka, H. Otsubo, Y. Takayama, T. Miyahara, S. Suzuki, Y. Achiba, M. Nakatake, T. Narimura, M. Higashiguchi, K. Shimada, H. Namatame, M. Taniguchi, Direct Observation of Tomonaga–Luttinger-Liquid State in Carbon Nanotubes at Low Temperatures, Nature, 426, 540 (2003).

[15] S. Iijima, M. Yudasaka, R. Yamada, S. Bandow, K. Suenaga, F. Kokai, K. Takahashi, Nano-Aggregates of Single-Walled Graphitic Carbon Nano-Horns, Chem. Phys. Lett., 309, 165 (1999).

[16] M. José-Yacamán, M. Miki-Yoshida, L. Rendon, J.G. Santiesteban, Catalytic Growth of Carbon Microtubules with Fullerene Structure, Appl. Phys. Lett., 62, 657 (1993).

[17] P. L. Walker Jr. et al., J. Phys. Chem, 63, 133 (1959).

[18] W.Z. Li, S.S. Xie, L.X. Qian, B.H. Chang, B.S. Zou, W.Y. Zhou, R.A. Zhao, G. Wang, Large-Scale Synthesis of Carbon Nanotubes, Science, 274, 1701 (1996).

[19] H. Ago, T. Komatsu, S. Ohshima, Y. Kuriki, M. Yumura, Dispersion of Metal Nanoparticles for Aligned Carbon Nanotube Arrays, Appl. Phys. Lett., 77, 79 (2000).

[20] M. Terrones, N. Grobert, J. Olivares, J.P. Zhang, H. Terrones, K. Kordatos, W.K. Hsu, J.P. Hare, P.D. Townsend, K. Prassides, A.K. Cheetham, H.W. Kroto, D.R.M. Walton, Controlled Production of Aligned-Nanotube Bundles, Nature, 388, 52 (1997).

[21] Z.W. Pan, S.S. Xie, B.H. Chang, C.Y. Wang, L. Lu, W. Liu, W.Y. Zhou, W.Z. Li, Very Long Carbon Nanotubes, Nature, 394, 631 (1998).

[22] B.Q. Wei, R. Vajtai, Y. Jung, J. Ward, R. Zhang, G. Ramanath, P.M. Ajayan, Organized Assembly of Carbon Nanotubes, Nature, 416, 495 (2002).

[23] R.L.V. Wal, L.J. Hall, Carbon Nanotube Synthesis upon Stainless Steel Meshes, Carbon, 41, 659 (2003).

[24] C.-L. Lin, C.-F. Chen, S.-C. Shi, Field Emission Properties of Aligned Carbon Nanotubes Grown on Stainless Steel using CH4/CO2 Reactant Gas, Diamond and Related Materials, 13, 1026 (2004).

[25] J. Liu, M. Shao, X. Chen, W. Yu, X. Liu, Y. Qian, Large-Scale Synthesis of Carbon Nanotubes by an Ethanol Thermal Reduction Process, J. Am. Chem. Soc., 125, 8088 (2003).

[26] H. Yang, P. Mercier, S.C. Wang, D.L. Akins, High-Pressure Synthesis of Carbon Nanotubes with a Variety of Morphologies, Chem. Phys. Lett., 416, 18 (2005).

[27] P. Nikolaev, M.J. Bronikowski, R.K. Bradley, F. Rohmund, D.T. Colbert, K.A. Smith, R.E. Smalley, Gas-Phase Catalytic Growth of Single-Walled Carbon Nanotubes from Carbon Monoxide, Chem. Phys. Lett., 313, 91 (1999).

[28] W. Li, H. Zhang, C. Wang, Y. Zhang, L. Xu, K. Zhu, S. Xie, Raman Characterization of Aligned Carbon Nanotubes Produced by Thermal Decomposition of Hydrocarbon Vapor, Appl. Phys. Lett., 70, 2684 (1997).

[29] T. Katayama, H. Araki, K. Yoshino, Multiwalled Carbon Nanotubes with Bamboo-Like Structure and Effects of Heat Treatment, J. Appl. Phys., 91, 6675 (2002).

[30] P.M. Ajayan, J.M. Nugent, R.W. Siegel, B. Wei, Ph. Kohler-Redlich, Growth of Carbon Micro-Trees, Nature, 404, 243 (2000).

[31] J. Li, C. Papadopoulos, J. Xu, Growing Y-Junction Carbon Nanotubes, Nature, 402, 253 (1999).

[32] F.L. Deepak, A. Govindaraj, C.N.R. Rao, Synthetic Strategies for Y-Junction Carbon Nanotubes, Chem. Phys. Lett., 345, 5 (2001).

[33] C.N.R. Rao, A. Govindaraj, Carbon Nanotubes from Organometallic Precursors, Acc. Chem. Res., 35, 998 (2002).

4

Solubilization of Single-Walled Carbon Nanotubes

The unique electronic properties of single-walled carbon nanotubes (SWNTs) have attracted much academic and industrial attention. The next logical step is the integration of SWNTs in functional devices. Without industrial and commercialized products, SWNTs will just be another exciting new material with extraordinary physical properties without any marketable value. One major challenge that has impeded the use of SWNTs is their insolubility in most solvents. SWNTs tend to bundle together due to strong van der Waals forces of tube-tube contact. Here, we address the solubilization and individualization of SWNTs.

SWNTs are insoluble in most solvents. The insolubility of SWNTs has been a major impediment for the future applications of these exciting new materials. Since most chemistry is done in solution, the ability to dissolve tubes in organic and aqueous solvents is essential to enable their subsequent functionalization for biomedical and material applications. Furthermore, single SWNTs or small bundles (2-5 tubes) are desirable for most applications. As-prepared SWNTs tend to tangle together into large bundles or ropes (more than 5 tubes) due to tube-tube Van-der-Waals interactions [1]. Bundled SWNTs are difficult to disrupt, and these aggregated tubes are difficult to disperse in solution. The bundling of SWNTs very significantly affects the electronic, optical, and mechanical properties of nanotubes. For example, the aggregation of nanotubes results in the quenching of the fluorescence of semiconducting tubes [2]. To address this insolubility issue, two main approaches have been used. One approach involves the functionalization of SWNTs along the sidewall or on the end caps of the nanotubes. This chemical functionalization approach typically disrupts the electronic properties of the functionalized SWNTs. However, the chemical functionalization of SWNTs allows them to interact with various chemical moieties, and functionalized SWNTs can be used to selectively bind biological species for biosensor applications. A second approach that is commonly used is the non-covalent wrapping of SWNTs in different surfactants, which also leads to the individualization of the SWNTs. The major advantage of this approach is that the electronic

properties of SWNTs are not disrupted. Consequently, these non-covalently-functionalized SWNTs can be used in device applications.

4.1 Methods for the Solubilization of SWNTs

Since the discovery of SWNTs in 1993 [3], they have attracted much attention for their remarkable structural, mechanical, and electronic properties [4]. Potential applications have been proposed for SWNTs in optoelectronic devices [5], as the active elements of field-emission diodes, as hydrogen storage materials, and as scanning probe microscopy tips [6, 7]. In addition, SWNTs have attracted attention in the area of biomedical engineering recently. In biomedical applications, as examples, SWNTs have been extensively studied for incorporation into biosensors [8, 9], drug delivery platforms [10], and for bone reconstruction [11]. Although carbon nanotubes clearly have great potential for many applications, the controlled separation of SWNTs according to chirality (and thus electronic properties) still remains a challenge. This has impeded the integration of SWNTs in electronic devices. One major challenge to handling SWNTs is their tendency to aggregate into large bundles and their insolubility in most solvents. The individualization of bundled and aggregated tubes is essential for the full realization of the remarkable potential of these materials. Another challenge is the dissolution of individual nanotubes in solution. As mentioned previously, covalent [12] and non-covalent [13] functionalization methods have been developed to unbundle and solubilize SWNTs. However, even though covalent modification is very effective in dissolving SWNTs [14], this process typically leads to the disruption of the electronic properties of

the SWNTs [15]. Thus, to retain the good electronic properties of SWNTs, an alternative approach has been developed to solubilize SWNTs involving the physisorption of polymers or surfactants onto the SWNTs. Non-covalent functionalization with surfactants usually leads to the individualization of SWNTs or the formation of small bundles of 2-5 nanotubes [16].

Three different approaches have been used to functionalize SWNTs, as shown in Figure 4-1. The first approach involves acid treatment in order to form functional groups on the side wall of SWNTs (discussed in section 4.2). The second approach involves the polymer wrapping of SWNTs (discussed in section 4.3). The third approach involves the encapsulation of SWNTs by surfactants (discussed in section 4.4).

4.2 Purification

In the early stages of nanotube research, as-purchased SWNTs (AP-SWNT) were contaminated with different metal catalysts (e.g., Fe, Co, Ni) used during synthesis. Thus, the first approach involves the purification of SWNTs [17–19] and the removal of metal catalysts and amorphorous carbon. The first step in the purification protocol usually involves acid treatments either under reflux or with ultrasonication.

4.2.1 Introduction

The electronic properties of SWNTs are very sensitive to the diameter and chirality of the nanotubes. The HiPco nanotubes (produced by a high-pressure CO conversion process using Fe as the catalyst) have diameters ranging from 0.7 to 1.4 nm. Although many different kinds of tubes are available commercially, we have used HiPco SWNTs in most of our experiments. Thus, unless otherwise mentioned, the nanotubes used are HiPco SWNTs.

AP-SWNTs contain residues of metals that were used as catalysts in the synthesis process. The aim of purification is to remove this catalyst material and amorphous carbons. Typically, the purification process includes acid treatment followed by filtration and/or centrifugation. Many different methods have been reported up till now. The most popular purification techniques are oxidation, thermal annealing, and acid treatment. An effective acid-treatment protocol was first developed by Rinzer et al. [20] to purify large quantities of SWNTs in high yields. Most acid-treatment protocols involve the use of oxidizing acids such as H_2SO_4 and HNO_3 and non-oxidizing acids such as HCl. SWNTs are either refluxed in an acid solution or subjected to ultrasonication with the acid. Zhang

and co-workers [21] have systematically compared the effectiveness of different purification protocols. Acid treatment generally results in the functionalization of the end caps and defect sites with oxygenated functional groups such as the carboxylic acid groups depicted in Figure 4-1(a). However, acid treatment can be quite destructive, especially to small-diameter tubes. Most importantly, oxidizing acids often disrupt the electronic properties of SWNTs. The purification of SWNTs without disrupting their electronic properties still remains a challenge. Methods such as magnetic filtration [22] have been developed to purify SWNTs without functionalization. A more thorough procedure using acid reflux to remove catalysts, followed by sonication to exfoliate and shorten the tubes has been developed by Q. Chen et al. [23]. However, with improvements in the synthesis process, the purity of AP-SWNTs is already around 85%. Therefore, the purification of SWNTs is not always necessary. Nevertheless, purification procedures can have the added benefit of functionalizing the end caps of the tubes due to the increased curvature at these sites. One of the crucial parameters to control purification during acid reflux without damaging tubes is the temperature [24]. Centrifugation is carried out to separate the catalyst (suspended in the supernatant) and amorphorous carbon from functionalized and purified SWNTs (which is recovered as the precipitate).

In order to compare the properties of SWNTs after purification, both reflux and sonication methods have been employed in the experiment. The purification procedures were based on processes reported previously in the literature [23, 25].

4.2.2 Experimental

Pure HiPco SWNTs were purchased from Carbon Nanotechnologies, Inc., Houston, Texas (Lot#: P0257, P0286).

Reflux procedure in HNO_3/HCl (1:1 v/v) mixture: 20 mg SWNTs (Lot# P0257) were refluxed in 20 mL HCl and 20 mL HNO_3 at 100 °C over an oil bath for 18 h. After acid treatment, the solution was allowed to stand at room temperature for 1 day to let the tubes sediment to the bottom. Most of the supernatant was then carefully removed without disturbing the precipitated tubes. The remaining solution with nanotubes was centrifuged in a Fisher Scientific Centrific centrifuge (Model 228; RPM = 3,300 rpm) for 10 minutes. The precipitate was rinsed with water and centrifuged again for several cycles. The dried sample was obtained by placing the centrifuged tubes in an oven at 200 °C for 4 h. After the sample was completely dry, the purified-SWNTs (pSWNT) were redispersed in 0.5 wt% AOT aqueous solution using ultrasonication for 2 h.

An identical procedure was carried out except for the duration of reflux. Each cycle was refluxed in 20 mL HNO_3- HCl for 6 h plus centrifugation, and the precipitate was used for refluxing in the next cycle. This was repeated 3 times.

Sonication procedure in H_2SO_4/HNO_3 (3:1 v/v) mixture: Two vials of 20 mg SWNTs (Lot# P0286) were sonicated in 4 mL of a mixture of H_2SO_4 and HNO_3 (3:1 v/v) for 1 h. The SWNT-acid mixture was centrifuged, and the precipitate was rinsed with H_2O several times, rinsed with NaOH three times, and with H_2O in the last cycle. The centrifuged sample was dried in an oven at 70 °C. Two dispersion procedures have been used. One part of the precipitate was directly dispersed in water, and the other part was

dispersed in 0.2 wt% AOT aqueous solution. Both dispersions were sonicated in a Fisher Ultrasonic Cleaner (model FS15) for 1 h.

Raman spectra were obtained using a HR800 Jobin Yvon Horiba Raman Microscope equipped with a charge coupled device (CCD) detector. A He/Ne laser with an energy of 632.8 nm (1.96 eV) was used as the excitation source. The Raman spectra were collected using a liquid sample holder with a quartz cell or on a silicon wafer in a backscattering configuration. For backscattering collection, a microscope with a 100X objective was used in room temperature.

4.2.3 Results and Discussion

The different purification methods, reflux and sonication, are compared in Figure 4-2(A). Curve (1) is observed after 18 h acid reflux. The intensity of the D-band peak increases due to damage to SWNT sidewalls. Curve (2) shows the Raman spectra for SWNTs treated with the same acid mixture but put through three sequential 6 h reflux-centrifugation cycles. Although the total reflux time is the same, the nanotubes sustain more damage than for just one acid reflux cycle. Hence, the D-band intensity is also increased. It is likely that there is some loss of material in each reflux-centrifugation cycle. Consequently, a relatively small amount of tubes is treated with high concentrations of the acid in the latter steps, which may explain the enhanced damage. The sonicated SWNTs exhibit a strong photoluminescent (PL) signal, as shown in Figure 4-2A curve (c). The acid SWNTs mixture used for sonication was homogeneous. It is difficult to remove unwanted residues from the SWNTs. The mixture became viscous and is highly protonated when the solution is neutralized. In part B, the acid-treated carbon

nanotubes were dispersed in an aqueous solution of AOT after either refluxing or sonication. From empirical results [26], it is expected that acid-treated SWNTs will produce –COOH group on endcaps and tube's surface. Hydrogen bonding may be possible between –COOH (from 18 h acid-treated SWNTs) and –O (from the hydrophilic head group of AOT), resulting in Figure 4-2B (b). Consequently, the RBM peaks in the Raman spectra are diminished. Acid treatment with an oxidizing acid will oxidize the end caps and attack the defect sites. After the end caps are consumed, acid oxidation will result in the shortening of the tubes. In contrast, it is well known that ultrasonication cuts tubes at defect sites, yielding shorter fragments of SWNTs. It can be deduced that sonicating acid-treated SWNTs became fragile, and may destroy the cylindrical structure of the tubes (Part B curve c). This is also seen when SWNTs are dispersed into AOT aqueous solution (Part B curve d).

The flow chart in Figure 4-3 depicts the steps of the ultrasonication purification experiment. This shows that purified tubes are dispersed into different solvents, for example, water, NaOH, and AOT aqueous solution. Comparison of SWNTs dispersion in the three different solvents is shown in Figure 4-3 that display in full region (A) and low frequency region (B). The solutions were prepared by dispersing 1 mg of d-pSWNTs (vacuum dried SWNTs after purification) in 10 mL of each individual solution. Curve (a) corresponds to directly dispersing sonicated acid-treated nanotubes into water solution. Curve (b) corresponds to dispersing sonicated acid-treated nanotubes into NaOH with sonication to perform neutralization action, and then centrifuged, dried and redispersed into water. Curve (c) corresponds to dispersing acid-treated nanotubes into AOT aqueous solution.

4.2.4 Conclusion

The removal of catalysts and amorphous carbon materials is still a challenge and there is much effort focused on developing better purification methods. The controllable introduction of functional groups on SWNTs surfaces also remains an area of active research. From the Raman spectra in Figure 4-2 and Figure 4-3, acid treatments, either in reflux or in sonication, demonstrated acid-treated processes are not practical for better isolation of bundled SWNTs into individual tubes, and the spectra showed evidence of the damaged tubes. However, techniques for producing purified SWNTs are constantly being modified and improved. Different functionalization approaches are currently being developed to incorporate nanotubes in nanocomposites and to enable them to bind different species.

4.3 Dispersion in Polymer

In this section, we discuss the one-step diameter-selective dispersion of HiPco SWNTs with the polymer Chitosan (CHI). Polymeric CHI is a water-soluble, biocompatible, and an antibacterial polyelectrolyte. It is found to preferentially wrap around small-diameter SWNTs with a narrow diameter distribution, leading to the suspension of SWNT in an aqueous medium, whereas the larger-diameter SWNTs precipitate from solution either spontaneously or upon centrifugation. UV-Vis absorption, Raman scattering using 514 and 632 nm excitations, and AFM measurements have been used to characterize the SWNT samples.

4.3.1 Introduction

SWNTs have attracted enormous attention from scientists and engineers because of their highly unusual structural (a 1D rolled-up of 2D graphite sheet), mechanical (Young's modulus, tensile strength and density), and electrical (conducting or semiconducting) properties. Indeed, their properties have made them attractive candidates for many important applications, such as field emission devices (e.g. field effect transistor, FET [27]), storage materials (e.g. hydrogen storage [28]), and scanning-probe microscopy tips (e.g. AFM tip [29]). A number of challenges, however, must be overcome before SWNTs can be exploited for most of the envisioned applications as mentioned before. These challenges include high-yield and purity synthesis, length control of tubes, selectivity of particular diameters and chiralities, and protocol development for physically manipulating and chemically processing individual nanotubes or their composites.

The wrapping of SWNTs with conjugate polymer allows the tubes to be dissolved while still retaining their electronic properties. The solubilization and functionalization of SWNTs can be achieved by carefully selecting the appropriate polymers. Modeling and calculations done by Blau et al. [30] demonstrate the potential advantages of using polymer matrices for the homogenous solubilization of tubes, the isolating of individual tubes, and to enable the decoration of the SWNT sidewalls with functional groups.

The solubilization of nanotubes by post-synthesis treatment might bestow extra benefits, including some that are desirable, and some that are quite remarkable, such as the separation of semiconducting and metallic tubes, the partitioning of zigzag, armchair, and chiral tubes, and even separations by length (as discussed in the next section). In order to explore particular applications, selection of specific diameters and chiralities can be crucial parameters. Lee et al. [31] have reported a large scale high-yield process (over 55%), yielding SWNTs with a less concentration of defects and with a controlled diameter (0.7-2.8 nm) using the CVD method. The CVD method is easy to setup and is a low-cost growth procedure for fabricating relatively pure nanotubes. A CVD method using catalysts supported in a mesoporous MCM-41 matrix has been reported by Shinohara and co-workers [32]. These researchers have systematically varied the different synthesis times and temperatures to control the diameter and purity of the attained carbon nanotubes. Many different approaches are being used to synthesize carbon nanotubes.

The ultimate goal is the synthesis of SWNTs that all have the same chirality. However, there is much that needs be done in terms of developing the synthesis before the chirality can be “dialed in.” One alternative approach involves the post-synthesis

separation of SWNTs by chirality. In practice, it might be easier to separate nanotubes by diameter rather than chirality. The chemical reactivity of SWNTs is significantly affected by the diameter of the nanotubes. This provides a handle for separating SWNTs by diameter. Small diameter (ca. 0.7 – 1.2 nm) SWNTs are typically more reactive than their larger diameter counterparts due to increased strain from pyramidaliztion and π-orbital misalignment [33]. As a result, the smaller diameter tubes are more susceptible to functionalization upon acid treatment [34]. The separation of metallic and semiconducting SWNTs is also of great interest. As prepared SWNTs have both metallic and semiconducting tubes that coexisting in the same sample. Several different separation methods have been recently developed. Lee et al. [35] have used the functionalization of SWNTs by nitronium ions (NO_2^+) to separate semiconducting and metallic SWNTs. Papadimitrakopoulos and co-workers [36] and Tour and co-workers [37] have used different sidewall-functionalization approaches to separate metallic and semiconducting SWNTs. These post-synthesis separate metallic or semiconducting SWNT may be useful for FETs, chemical sensors, biomedical sensors, etc.

Most common polymers that were used to wrap carbon nanotubes are poly(vinyl pyrrolidone) (PVP) [38] and poly(meta-phenylenevinylene) (PmPV) [39]. In this study [40], CHI (shown in Figure 4-1b), a biological polysaccharide macromolecule, has been used as the polymeric wrapping agent. CHI is abundantly available and can be extracted from the skeletons of crustaceans such as shrimps. CHI has been used as the primary ingredient in many commercialized products such as cosmetics, dietary supplements, and skin care lotions. The natural abundance and non-toxicity of CHI make it especially ideal for use in functionalizing SWNTs. CHI contains an amino group ($-NH_2$) at the C-2

position and a hydroxyl group (-OH) at the C-6 position. It is used here as a wrapping agent to non-covalently encapsulate SWNTs. During dispersion, CHI wraps around carbon nanotubes as a serpentine rope (Figure 4-1b cartoon). The SWNT-CHI interactions are diameter selective, and different diameter distributions are found in supernatant and precipitate.

4.3.2 Experimental

AP-SWNTs (HiPco) were purchased from Carbon Nanotechnologies, Inc., Houston, Texas ((Lot#: P0257, Batch#: 7782-42-5). CHI (poly(D-glucosamine), low molecular weight, M.W. 6,300,000) and sodium dodecylbenzene sulfonate (SDBS) were purchased from Sigma-Aldrich Co. All solutions were prepared using deionized water.

A stock solution (0.5 wt% CHI solution) for dispersing SWNTs was prepared by dissolving a CHI flake in 0.01 M H_2SO_4 aqueous solution at 80-90 ^oC. The CHI/H_2SO_4 solution was then cooled to room temperature, and filtered after washing several times with deionized water. After drying, the CHI powder was re-dispersed in water to form an aqueous stock solution. To achieve solubilization of SWNTs, 1.0 mg of HiPco SWNTs was added to a 10.0 mL of 0.5 wt% aqueous solution of CHI, and the mixture was ultrasonically treated in an ice bath for more than 5 h to accomplish dispersion. The resultant (SWNT/CHI solution) black supernatant had a calculated concentration of 0.1 mg/mL and appeared to be homogeneous and stable. The SWNT/CHI solution was allowed to stand overnight. A murky black precipitate settled at the bottom and was separated, whereas the suspension remained clear and homogeneous. The supernatant

was then carefully decanted for further centrifugation. The centrifugation was carried out at 29,000 g for 2 hours.

For comparative purposes, a 0.10 mg/mL solution SWNT/SDBS was formed comprising 1.0 mg of HiPco SWNTs, 3.0 mg of SDBS, and 10.0 mL of water. Ultrasonication was used to mix the nanotubes and SDBS in an ice bath for more than 10 h to form the SWNT/SDBS solution. Subsequently, the supernatant was subjected to centrifugation at 29,000 g for 2 h.

UV-Vis absorption spectra were acquired using a Perkin-Elmer Lambda 18 spectrophotometer over the range of 200-900 nm; quartz cuvettes were used for these measurements. Raman spectra were obtained using an HR800 Jobin Yvon Horiba Raman microscope. Samples were placed in quartz cuvettes, and laser excitation energies of 632.8 or 514.5 nm were used to acquire the Raman spectra. AFM images were obtained using a Vecco Digital Instrument, Nanoscope IIIA microscope in the tapping mode. One drop of a 0.1 mg/mL SWNT dispersion was placed on a mica film and air dried before observation.

4.3.3 Results and Discussion

Figure 4-4 compares the UV-Vis absorption spectra of supernatants of 0.1 mg/mL SWNTs solutions dispersed using SDBS and CHI after 2 h centrifugation at 29,000 g; the spectrum for the SWNT/CHI suspension before centrifugation is also shown in the figure. Well-resolved and narrow optical absorption features are visible for the samples after centrifugation. The peaks can be ascribed to transitions between the van Hove singularities in the density of states (DOS) of SWNTs. The narrow spectral features

indicate that the SWNTs have been individualized or exist in the form of small bundles [41].

In general, without centrifugation, SWNTs dispersed with the use of a coating agent exhibit absorption spectra that have broadened peaks, indicating the presence of nanotubes of a range of diameters as well as nanotubes that are bundled together (possibly in the form of ropes) whose individual transitions frequencies are affected by intermolecular interactions. After centrifugation, the absorption spectra of SWNTs contained in the supernatant are often found to exhibit sharper peaks resulting from interband transitions for isolated nanotubes. The decrease in intermolecular interactions leads to narrow spectra features from less homogeneous broadening. As can be seen in Figure 4-4 for CHI-dispersed SWNTs, no obvious changes in the absorption band widths, before or after 2 h centrifugation, are evident, suggesting complete dispersion even before centrifugation. However, we observe a small red-shift in the absorption bands for both metallic (ca. 400-600 nm range) and semiconducting (ca. 600-850 nm) tubes dispersed by CHI as compared to those dispersed by SDBS [42], suggesting a non-specific interaction of CHI with both metallic and semiconducting SWNTs.

It is to be noted that after the SWNTs are dispersed in a CHI aqueous solution, a black muddy precipitate appears after the solution is allowed to stand overnight (see Figure 4-4 image). Our hypothesis for this phenomenon is that the chitosan encapsulating the SWNTs might be in a serpentine rope configuration. To wrap larger diameter or bundled SWNTs, chitosan will need to have more than one revolution around the tubes and this is the mechanism by which the larger diameter tubes are separated and precipitated. Nevertheless, the associated supernatant is homogeneous with a transparent

black color. The precipitate cannot be redispersed using the CHI solution. This suggests a robust method for forming stable SWNTs in solution.

Raman spectroscopy is a powerful probe of the structure of carbon nanotubes. Depending on the excitation energy, Raman spectra can probe different types of tubes. It is known that at 632.8 nm laser radiation (1.96 eV), the Raman spectra of both semiconducting and metallic HiPco nanotubes, but primarily of semiconducting tubes, are resonantly enhanced. Figure 4-5 shows the Raman spectra of the raw HiPco SWNT sample, the supernatant of dispersed SWNTs in CHI solution (the final concentration is 0.1 mg/mL) without centrifugation, and the precipitate. In Figure 4-5(A), the G^+ bands at ca. 1590 cm^{-1} and the distinctive shoulder peaks at ca. 1551 cm^{-1} (i.e., G^- bands) associated with the E_{2g} optical modes of graphite, indicate the presence of SWNTs in the sample. Compared with the as-received raw HiPco SWNTs in curve (a) of Figure 4-5(A), the supernatant without centrifugation in curve (b) has a narrower G^+ band and the G^- band is diminished in intensity; whereas for the precipitate in curve (c), the G^+ band is broader and the G^- band is enhanced in intensity. The latter band also has a narrower lineshape as compared to the raw HiPco sample. The G^- band is associated with vibrations along the circumferential direction of the nanotubes, and lineshape is sensitive to the types of carbon nanotubes [43]. These findings suggest that more metallic (broaden Breit-Wigner-Fano lineshape) nanotubes exist in the supernatant and more semiconducting (sharp Lorentzian lineshape) tubes are present in the precipitate. Additionally, the relatively low intensity of the D-band at ca. 1308 cm^{-1} indicates that the amount of amorphous carbon in our CHI-dispersed SWNT sample is quite low. The low-frequency RBM region in Figure 4-5(B) shows characteristic radial vibrations of the

SWNTs. For the raw HiPco sample shown in curve (a) of Figure 4-5(B), five distinct RBM peaks are found at around (i) 191, (ii) 217, (iii) 255, (iv) 281, and (v) 294 cm^{-1}, corresponding to the nanotube diameters of 1.25, 1.09 0.92, 0.83, and 0.79 nm, respectively. SWNT diameters are deduced from the RBM frequency, $\omega_{RBM}(cm^{-1})$, using $d(nm) = 223.5/(\omega_{RBM}(cm^{-1}) - 12.5)$ [44] where the two empirical parameters 223.5 and 12.5 (which vary depending on the synthesis process) are derived from previous experiments on HiPco SWNTs. As indicated in a previous literature report the RBM bands above ca. 240 cm^{-1} correspond to smaller diameter nanotubes while RBM bands below 240 cm^{-1} correspond to larger diameter nanotubes. The peaks labeled (i), (ii), (iii), (iv), and (v) can be assigned to (11,7)/(14,3), (12,3), (9,4)/(11,1), (10,1), and (10,0) SWNTs. The peak at 191 cm^{-1} may originate from either (11,7) or (14,3) SWNTs. For the supernatant of CHI-dispersed SWNTs, only two RBM bands are observed at 256 and 283 cm^{-1}, corresponding to SWNTs with diameters of 0.92 and 0.83 nm, respectively. These bands indicate an enrichment of small-diameter SWNTs in the supernatant. For SWNTs in the precipitate, the appearances of RBM peaks at ca. 195 (1.22 nm), 217 (1.09 nm), 244 (0.97 nm), 257 (0.92 nm), and 286 (0.82 nm) cm^{-1} denotes a predominance of large-diameter nanotubes. The Raman spectra acquired with 632.8 nm excitation indicates that the CHI wrapping process leads to some selectivity: smaller diameter SWNTs are preferentially found in the supernatant whereas larger diameter SWNTs are present in the precipitate.

A laser excitation energy of 2.41 eV (514.5 nm) is expected to resonantly enhance Raman scattering from metallic nanotubes for HiPco samples. In curves (a), (b), and (c) of Figure 4-6(A), the G^- bands indicate the presence of metallic SWNTs. From curve

(b), it is difficult to determine whether the G^+ band is broader or narrower than those in curves (a) or (c); however, the G^- band in curve (c) is clearly enhanced relative to the band in curve (a). Thus, from the Raman spectra acquired with 514.5 nm excitation, it appears that there may be a higher concentration of metallic SWNTs in the precipitate. However, our evidence for this selectivity is not compelling, and is likely associated with poor resonance discrimination between different SWNT chiralities upon excitations at 514.5 nm. However, bands in the RBM region provide better insight into the selectivity of this functionalization process. In the RBM region in Figure 3(B), for raw HiPco SWNTs, there are four distinct peaks located at 185, 206, 249, and 265 cm^{-1}, which correspond to nanotube diameters of 1.30, 1.16, 0.95, and 0.89 nm with chiral indices of (14,4), (14,1), (12,0), and (10,2), respectively. For CHI-dispersed SWNTs in curve (b), one RBM band at 278 cm^{-1} is most prominent, corresponding to SWNTs with diameters of 0.84 nm and with a chirality of (8,4), a less prominent shoulder corresponding to (10,3) SWNTs with a diameter of 0.93 nm is also observed. For the functionalized precipitate (curve (c)), the semiconducting SWNTs with RBM bands at 183, 203, 242, and 257 cm^{-1} correspond to nanotube diameters of 1.31, 1.17, 0.97, and 0.91 nm with chiral indices of (10,9), (9,8)/(13,3), (9,5), and (11,1), respectively. As reported in the literature [45][1], RBM bands between 175 to 213 cm^{-1} correspond to semiconducting nanotubes with the diameters larger than 1.1 nm, and RBM bands between 218 to 280 cm^{-1} correspond to metallic nanotubes with the diameters smaller than 1.1 nm at laser excitation energy of 2.41 eV. It is clear that small-diameter SWNTs are selectively wrapped by the polymer, which helps them dissolved and suspended in the supernatant. Conversely, the larger diameter nanotubes can be found in the precipitate.

From Raman spectra acquired with 632.8 and 514.5 nm laser excitation, it appears that smaller diameter SWNTs are selectively dispersed by CHI. The functionalization process does not appear to be chirality selective. This process thus allows the separation of SWNTs according to their diameter. In the supernatant layer, the diameter of the tubes appears to be less than 1 nm. The Raman spectra of the precipitate (1.96 and 2.41 eV laser source) show a broad diameter distribution from 0.8 to 1.3 nm. Table 5 shows a summary of the diameter selectivity discussed above. The results reveal that the supernatant of the SWNT/CHI system contained diameters of nanotubes that are smaller than 1 nm. The precipitate contains a broader range of diameters in which the majority is larger than 1 nm. Coincident to this is that the semiconductor nanotubes appeared in 2/3 ratio and metallic tubes are in 1/3 ratio of the bands in two laser source excitation energy.

Figure 4-7 provides an AFM image of SWNTs dispersed in CHI aqueous solution (after 2 h centrifugation) coated onto a mica substrate. The AFM image clearly reveals separated and individual SWNTs wrapped with CHI that have been adsorbed onto the mica substrate. These samples have been found to be extremely stable and do not spontaneously rebundled. From the AFM images, the height of the tubes is visualized as approximately 1.22 ~ 1.48 nm. This dimension is rationalized as resulting from HiPco SWNTs surrounded by Chitosan. Additionally, in AFM images one finds many free Chitosan nanoparticles on the mica surface, consistent with Chitosan selectively wrapping nanotubes of a limited diameter range or not at all, freeing up unused Chitosan to form the nanoparticles.

4.3.4 Conclusions

In conclusion, a simple and efficient process for the water dispersion and diameter-selective separation of SWNTs without centrifugation was constructed. "Smaller-diameter" SWNTs are preferentially dispersed and wrapped by CHI in the aqueous supernatant followed by centrifugation, while "larger-diameter" SWNTs exist in the precipitation just one day after formation of dispersion before centrifugation. The driving force is likely the increase in surface reactivity with decreasing diameter of SWNTs and an appropriate match between charge on the polyelectrolyte and reactive sites on the surface. In addition of the surface reaction, for CHI to wrap around larger diameter tubes firmly, it will require CHI to coil more tightly, and with more revolutions, around the nanotubes. This results in the larger diameter SWNTs to be much heavier and eventually cause the SWNT/CHI composite to sink down onto the bottom of solution. From Raman measurements, the tube diameter from the supernatant is about 0.9 ± 0.1 nm, which greatly limits the chirality of the SWNTs as well. Since CHI is a water-soluble and biocompatible polymer which exists in many commercial products on the market, integrating SWNTs with CHI into nanocomposites may increase its advantages in biosensor device developments.

4.4 Dispersion in Surfactants

In this section, the debundling and aqueous dispersion of SWNTs using an anionic, biomimetic surfactant, dioctyl sodium sulfosuccinate (Aerosol-OT, or AOT) is discussed [46]. The effectiveness of different concentration of AOT aqueous solutions for forming stable dispersions of SWNT samples has been assessed using the critical micellar concentration (CMC) as a reference. The effects of centrifugation duration and concentration of AOT surfactant on the debundling and dispersion of a HiPco sample into individual SWNTs in aqueous solution have also been investigated. UV-Vis-NIR and Raman spectroscopy and AFM microscopy have been employed to characterize solubilized SWNTs. Additionally, the SWNT-AOT dispersions have been utilized to align SWNTs in FET geometries by AC dielectrophoresis. Centrifugation of the aforementioned dispersion results in enhanced concentrations of individual SWNTs, as judged from the decreased absorption intensities, attributed to the removal of small bundled tubes in the supernatant, and sharpening of interband transition peaks measured by absorption spectroscopy. Typical SWNT-AOT suspensions have been found to be stable for more than a year.

4.4.1 Introduction

Despite the benefits of purifying SWNTs, the harsh acid treatment does lead to some undesirable defects in the tubes. This makes it unsuitable for many applications, especially in the biomedical field. The dispersion of SWNTs in aqueous solutions of

surfactants may yield dissolved tubes with intact electronic properties. Therefore, the dispersion of SWNTs in surfactant aqueous solutions without any acid treatment will be a welcome addition in the biological research field.

A well-known anionic surfactant (shown in Figure 4-1c), AOT – widely used as the stabilizer in reverse micelle (water-in-oil) microemulsion systems [47], is used to solubilize and non-covalently wrap SWNTs in aqueous solution. It is well known that AOT can serve to encapsulate different nanotubes materials [48] and can also act as a capping agent to control the sizes of nanoparticles [49]. The structure of AOT is depicted in Figure 4-1c, and has a hydrophilic head and a short hydrophobic double tail [50]. The latter structural feature was a factor in choosing AOT for investigation, since we anticipated that the short tail might efficiently allow the intercalation of AOT between bundled SWNTs, possibly aided by ultrasonication, thereby facilitating the debundling of the nanotubes.

In this section, we report a detailed study of the dispersion of SWNTs in AOT aqueous solutions. We also compare SWNT-AOT dispersions with nanotube solutions prepared using other anionic and cationic surfactants. Sodium dodecylbenzenesulfonic acid (SDBS) has been used frequently to individualize bundled SWNTs [51, 52]; however, no detailed studies of the dispersion of SWNTs using AOT have been reported. The CMC is a main factor for surfactants to form micelles. Below the CMC, surfactants are unable to assemble together due to the surface tension around the medium (such as water). Different concentrations of AOT, therefore, produce different kinds of SWNT dispersions. The choice of Aerosol OT is due to the fact that AOT possesses a hydrophilic head and hydrophobic tail group with microemulsion properties, which might

be useful for future biological applications. Ultrasonication is commonly used to prepare good SWNT dispersions [53]. Bundled SWNTs are dispersed in AOT aqueous solutions with sonication to separate the bundled tubes and cut the tubes into isolated individual short strands. Sonic vibrations are used to assist the AOT spacing agent to intercalate between aggregated tubes. We have attempted to determine the optimum concentrations and sonication times for the formation of good dispersions of individual SWNTs. The cartoon in Figure 4-1c depicts the individualization of bundled SWNTs. Dispersion followed by sonication is used to obtain well-dispersed SWNTs. High speed centrifugation is used to obtain solutions of individual SWNTs, and to separate the individual SWNTs from bundled SWNTs and catalysts particles [54] after direct dispersion of SWNTs into solution medium. We also demonstrate the formation of nanotube FETs using these individualized tubes.

4.4.2 Experimental

Materials: AP-HiPco SWNTs were purchased from Carbon Nanotechnologies, Inc., Houston, Texas (Lot#: P0257, Batch#: 7782-42-5). Anionic surfactant, 98% purity, of sodium bis(2-ethylhexyl) sulfosuccinate (also referred to herein as dioctyl sodium sulfosuccinate and/or AOT), was purchased from Fisher Scientific Co. Sodium dodecylbenzenesulfonic acid (SDBS) and dodecyltrimethylammonium bromide (C_{12}TAB) were purchased from Aldrich Chemical Co. The sodium salt of dodecyl sulfate (SDS) and n-hexadecyltrimethylammonium bromide (C_{16}TAB) were purchased from Alfa Aesar.

Methods: Various aqueous solutions with AOT concentrations of 22.5 (1.0 wt%), 11.25 (0.5 wt%), 4.5 (0.2 wt%), 2.25 (0.1 wt%), and 1.125 mM (0.05 wt%) were prepared in 20 mL vials. Measured quantities of as-purchased SWNTs (without further purification) were added to the AOT solutions to achieve a final SWNT concentration of 1 mg/mL. Homogeneous SWNT-AOT aqueous solutions were formed after 2 h sonication in an ice bath (Fisher Corp. FS15). To determine the solubility, different sonication times of 4, 8, 12, 16, and 24 h were used. Centrifugation at 29,000 g (ca. 17000 rpm), for durations of close to 2 hours, and for different AOT concentrations, resulted in the sedimentation of amorphous carbon and large bundled SWNTs at the bottom of the centrifuged microtubes. The upper 80% of the supernatant was siphoned-off for spectral characterization.

In order to assess the character of the supernatant, centrifugation durations of 1, 2, 3, and 6 hours for the 0.5 wt% AOT samples were utilized. Centrifugation was performed after allowing the sonicated SWNT-AOT samples to equilibrate at room temperature for 1 day. For comparative purposes, four other surfactants, anionic (SDBS and SDS) and cationic (C_{12}TAB and C_{16}TAB), have also been used to disperse SWNTs, with the as-prepared HiPco sample added to give solutions with a concentration of 1 mg/mL SWNTs and a surfactant concentration of 0.5 wt%.

Optical Spectroscopy: A Varian Cary 500 UV-Vis-NIR spectrometer with 240 nm/min scan speed was used to measure the electronic absorption spectra of the SWNT samples. Quartz cuvettes (10 mm path length) were used to hold the aqueous sample. For the Raman measurements, a Jobin Yvon Horiba, HR800 Raman spectrophotometer,

with the He/Ne laser excitation energy of 632.8 nm (1.96 eV) was used. The samples were placed in 10 mm quartz cuvettes.

Microscopy: For AFM measurements, a Vecco Digital Instrument Nanoscope IIIA spectrometer was used in tapping mode. The substrate for the measurements, a silicon wafer fragment (P<100>, P/Boron type) was cleaned by using a Piranha solution (4:1 v/v of 96% H_2SO_4 and 30% H_2O_2). A drop of the sample was placed on the cleaned silicon-wafer and air dried before observation.

To obtain TEM images, we utilized a TECNAI G2 F20 instrument manufactured by FEI Inc. For our measurements, a 300-mesh holey carbon grid film was used and the samples were prepared by dispensing 10 μL of the solution onto the grid; the excess solution was blotted by uranyl acetate.

AC Dielectrophoretic Alignment of SWNTs: Microlectrode structures with a 3 μm gap were fabricated on Si/SiO_2 (500 nm) substrates by electron-beam lithography, followed by the electron-beam evaporation of 5 nm Cr and then 50 nm Au. A 5 MHz 8 V peak-to-peak voltage was applied across the electrodes and an 8 μL drop of the AOT dispersion was placed in the gap. The drop was held in the gap for varying periods of time ranging from 1—5 min and was then washed with ~800 μL deionized water. Scanning electron microscopy (SEM) images of the aligned tubes were obtained on a Hitachi S4700 instrument at an accelerating voltage of 0.8 kV. The device characteristics of the obtained nanotube field-effect transistors were studied using a HP4145 semiconductor parameter analyzer using the silicon substrate as a back gate.

4.4.3 Results and Discussion

A large number of potential applications of SWNTs require that nanotubes be functionalized (covalently or non-covalently) and suspended in a stable solution as individual or very small bundled tubes. UV-Vis-NIR electronic absorption spectra can aid in the identification of specific individual SWNT types [55], through the existence of absorptions associated with interband transitions between van Hove singularities in the DOS of individual SWNTs, the relative changes of intensity for specific interband transitions can help to identify the selective solubilization of a particular SWNT species. Smalley et al., for example, reported interband transitions for HiPco/SDS dispersions containing metallic (M_{11}) and semiconducting (S_{22} and S_{11}) nanotubes, whose respective absorptions occur in the ranges of 440 to 645 nm, 600 to 800 nm, and 830 to 1600 nm [56].

To evaluate the solubilization and dispersion of SWNTs in AOT aqueous solution, four surfactants were used for comparative purposes, similar to an earlier investigation reported in the literature [57]. Figure 4-8 shows absorption spectra of 1 mg/mL SWNTs dispersed in 0.5 wt% of five different surfactant solutions, with 2 h centrifugation at 29,000 g following the 2 h sonication treatment. From the figure it is clear that the solubility of SWNTs dispersed in anionic surfactants (SDBS, SDS and AOT) is better than that observed for the cationic surfactants (C_{12}TAB and C_{16}TAB). This is clearly evident since the optical absorption spectra for the anionic surfactants are narrower and more well-defined then for the cationic surfactants. Moreover, the double-tailed AOT is shown to solubilize the SWNT sample better than SDS [58]. Also, AOT displays similar dispersing properties as SDBS (a commonly used surfactant for the non-covalent dispersion of SWNTs). Hence, AOT appears to be a good non-covalent wrapping species

for separation of bundled SWNTs into individual tubes, at least to an extent similar to that found for SDBS.

The sonication time is one of the important parameters for controlling the solubility of the SWNT dispersions [53]. The purpose of sonication is to use vibrations to shake apart the aggregation bundled SWNTs in order for surfactants to squeeze into the interstitial spaces between individual nanotubes. To determine the time required to completely separate the bundled tubes into individual ones, while also maintaining the length of the tubes, the sonication times are varied in the increments up to 1 day. Figure 4-9 exhibits the comparison of sonication time. Two HiPco SWNTs sources were used: Pure HiPco SWNTs, which contained 13 wt% residual Fe, and Raw HiPco SWNTs, which contained 20 wt% residual Fe (and cost $125/gram less than pure SWNTs). After 8 h sonication, pure-SWNTs are debundled to give individual SWNTs whereas raw-SWNTs require 16 h of sonication to isolate individual SWNTs. In other words, more time is required to debundle raw-SWNTs into individual tubes. After 20 h sonication, the curve for both pure-SWNTs and raw-SWNTs overlaps as displayed in Figure 4-9B. Therefore, saturation time for raw-SWNTs is 20h.

Centrifugation is another major parameter for obtaining individual SWNTs. Figure 4-10 shows the absorption spectra of 1.0 mg/mL SWNTs suspended in 0.5 wt% AOT solution at different centrifugation times [59]. In general, without centrifugation (but samples are diluted to 0.1 mg/mL in order to avoid too strong an absorption) dispersed as-synthesized SWNT samples exhibit absorption spectra with broadened peaks (especially in the S_{11} region), indicating the presence of nanotubes of a range of diameters as well as bundled nanotubes whose individual transitions frequencies are

affected by intermolecular interactions. With an increase in centrifugation time, Figure 4-10 indicates that fewer bundled SWNTs exist in the supernatant, as is to be expected. Moreover, after more than 2 h centrifugation, the absorption spectra of SWNTs are found to be dominated by sharp peaks, attributable to interband transitions of isolated nanotubes, indicating elimination, to a substantial degree, of bundled SWNTs [60]. It is further to be noted that absorption spectroscopy does not reveal any peak shifting or broadening after 2 h centrifugation; only changes in intensity associated with removal of SWNTs from the supernatant with extended centrifugation are observed.

Raman spectroscopy studies for the AOT-SWNT samples provide a slightly more in-depth assessment [43]. As regards to Raman spectra of 1.0 mg/mL SWNTs suspended in 0.5 wt% AOT solutions with different centrifugation times, such measurements (see Figure 4-11, parts A and B) can provide useful information on SWNT structure as well as information concerning the compositional makeup of samples [61]. From the Raman spectra in the region above 1200 cm^{-1} (i.e., part A), hereinafter also referred to as the high-frequency region, the G band (graphite tangential mode at ca. 1589 cm^{-1}) is associated with the optical mode E_{2g} of graphite, and is characteristic of sp^2 hybridized carbon materials, as are the distinctive shoulder peaks near the 1541 cm^{-1}. The Raman G-band mode uniquely indicates the presence of SWNTs and indicates the existence of a hexagonal graphite lattice. The relative intensity of the disorder-induced peak at ca. 1320 cm^{-1} (the so-called D-band) provides an indication of the relative amount of disordered carbon present. The relatively low intensity of the D-band indicates that the amount of amorphous carbon within these samples is quite low. In part B of Figure 4, referred to hereinafter as the low-frequency region, bands attributable to radial breathing mode

(RBM) vibrations of SWNTs are clearly seen. Figure 4B reveals that in the RBM region, a new band at 194 cm^{-1} is found after ca. 1 h centrifugation at 29,000 g, and a second band at 263 cm^{-1} is formed after 2 h centrifugation. No band shifts occurred after 2 h or more of centrifugation, but band narrowing is demonstrated. These results suggest that AOT wrapped nanotubes, with 2 h or more of centrifugation, are separated into individual or very small bundles in the supernatant. Raman scattering further reveals an overall increase in intensity with increasing centrifugation duration. Since the supernatant solution contains fewer tubes, there must be an increase in the concentration of individual tubes, indicating that residual bundling is eliminated with extended centrifugation.

As an additional study, we have examined the effect of AOT concentration on the absorption spectra of dispersed SWNTs. It is to be noted that the critical micellar concentration (CMC) for AOT in water at room temperature is ca. 0.12 wt% (2.50 mM), and the CMC is an important parameter that gauges how the surface tension of a surfactant can influences the formation of bilayer, cylindrical, and/or spherical micellar structures within host solutions [62]. Concentrations of AOT that exceed the CMC are expected to have some visible effects on the dispersion of the nanotubes [63]. Figure 4-12 is a comparison of the absorption spectra of SWNTs suspended at different AOT concentrations after 2 h centrifugation at 29,000 g. For our system, we can deduce that exceeding the CMC does have dramatic effects on the separation of individual HiPco SWNTs as compared with concentrations below the CMC. However, for concentrations of AOT above the CMC (0.2, 0.5, and 1.0 wt% of AOT), no new absorption bands appear, but absorptions of the existing bands are enhanced [56].

Figure 4-13 exhibits AFM and TEM images, respectively, of SWNT originally in 0.5 wt% AOT aqueous solution after 6 h centrifugation. The samples for AFM are placed onto Si wafer, whereas samples for TEM are placed onto TEM grid. The AFM height and phase images shown in Figure 4-13A reveal separated, individual SWNTs coated with AOT that have been adsorbed onto a Si wafer. These samples have been found to be extremely stable and do not spontaneously rebundle. From the AFM images, the height of the tubes is visualized as approximately 2 nm. This dimension can be rationalized as resulting from HiPco SWNTs surrounded by one layer of surfactant. Additionally, the tubes show evidence of long length, and the tubes do not seen to be shortened even after sonication for more than 8 h. This might be due to the double tail of AOT which may shield SWNTs during the sonication period. For longer sonication times, the affinity of AOT toward SWNTs will push AOT to more tightly bind the SWNTs. This phenomenon leads to the very long tubes observed in the AFM phase images. Isolated AOT-coated SWNTs are revealed in the TEM image shown in Figure 4-13B, further confirming the debundling of HiPco SWNTs by AOT.

As a demonstration of the potential device applications of these individualized tubes, we have fabricated field-effect transistors by aligning these AOT-solubilized tubes in device geometries by AC dielectrophoresis [45, 64]. The dielectrophoretic force experienced by a nanotube in solution is proportional to the difference between the complex dielectric constants of the nanotube and the medium (water in this case). Metallic nanotubes have a much higher dielectric constant than water ($\varepsilon = 79$) due to the presence of mobile carriers (effectively infinite). Semiconducting SWNTs have a bandgap dependent dielectric constant (~2—5), which is less than that of water;

however, due to the large surface conductance induced by the electric double layer at the surfactant interface, both metallic and semiconducting species are pulled into the gap [65]. Indeed, zeta potential measurements (-65.6 mV), indicate that the AOT-SWNT micelles carry a significant negative charge, which is not surprising given the anionic nature of the surfactant.

Figure 4-14 shows the alignment of AOT-solubilized SWNTs within device geometries upon the application of a 5 MHz AC voltage. The number of nanotubes in the gap can be controlled by the duration of the dielectrophoresis process. Single nanotube transistors and network devices containing dense arrays of aligned nanotubes can be obtained by varying the time the voltage is on from 1 to 5 min. The dielectrophoretically aligned nanotubes initially have high contact resistances (ranging up to 10 MΩ) due to the presence of the surfactant at the contacts. However, upon annealing under nitrogen at 300 °C, the contacts are significantly improved and ambipolar devices are obtained as shown in Figure 4-14e. A more detailed investigation of the device characteristics of surfactant wrapped tubes, including the role of the surfactant as a dielectric, is currently underway.

4.4.4 Conclusion

In summary, we have ascertained from UV-Vis-NIR and Raman measurements that even without centrifugation, dispersions of SWNTs samples in AOT solutions consist predominantly of individual nanotubes, although some quantity of small bundled material is deduced to exist in solution. Centrifugation of the aforementioned dispersion results in enhanced individual nanotube concentration, as judged from decreased

absorption intensities, attributed to the removal of small bundled tubes in the supernatant, and sharpening of interband transitions peaks measured by absorption spectroscopy. Moreover, following centrifugation, the Raman bands show intensity enhancements in accord with UV-Vis-NIR findings.

We have also demonstrated the precise placement of these nanotubes in device geometries. The number of tubes in the devices can be controlled by the duration of the dielectrophoresis process. Ambipolar transport has been demonstrated for a nanotube network device.

The data obtained in this paper [66] suggest the simplicity and efficiency of using AOT as a spacing agent for dispersion of SWNTs in aqueous solution. Moreover, the structure of AOT with two short hydrocarbons tails (ca. 1 nm for each) — with their hydrophobic character — that are close in length to that of phospholipids (head-to-tail about 2 nm) that exist in cell membranes, should facilitate intercalation of SWNTs in biological systems for biomedical applications, such as drug delivery systems.

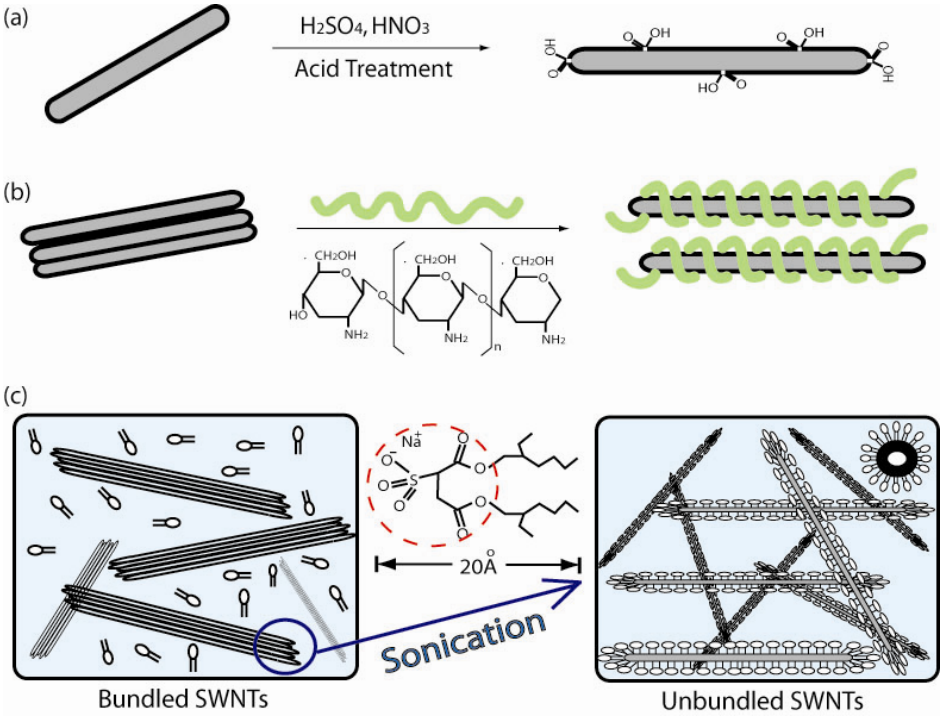

Figure 4-1 Solubilization of SWNTs can be performed by three basic methods. (a) Purification by acid treatment. (b) Polymer wrapped SWNTs. (c) Bundled SWNTs dispersed in anionic surfactant AOT aqueous solution, where AOT depicted as having a 'tadpole' structure.

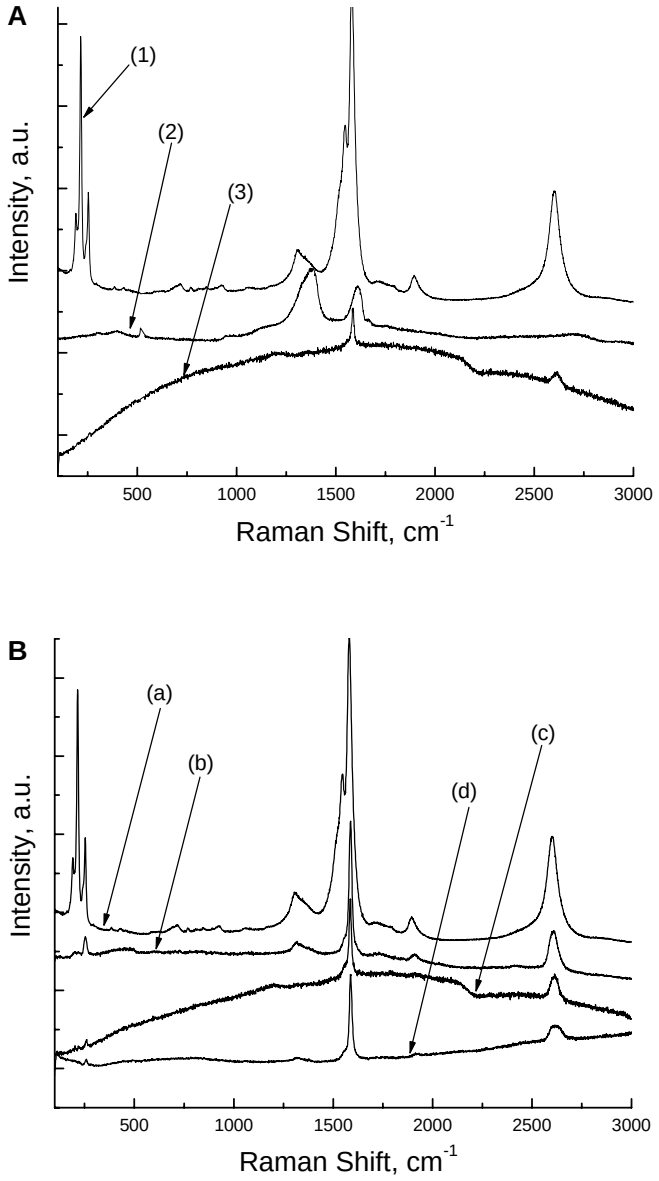

Figure 4-2 Comparison of refluxing treatment and ultrasonication in acid. In Part A, (1) the samples are refluxed for 18 h in 1 cycle, (2) refluxed 6 h over three periods, and (3) sonicated for 1 h. In Part B, (a) the SWNTs are refluxed for 18 h, (b) acid refluxed SWNTs are dispersed in AOT aqueous solution, (c) SWNTs sonicated for 1 h, and (d) disperse acid sonication tubes in AOT aqueous solution.

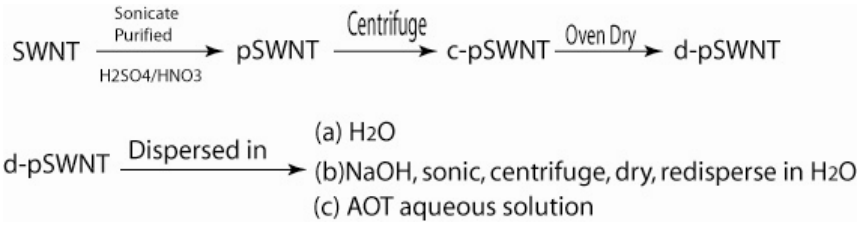

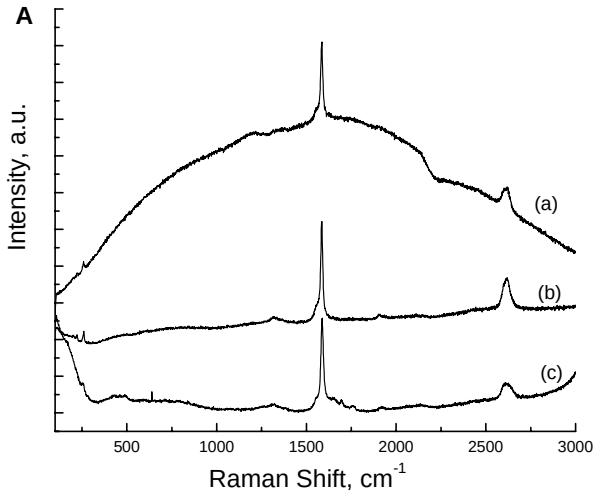

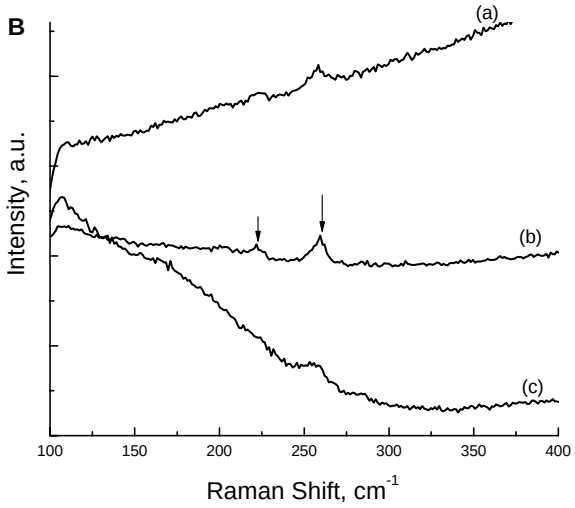

Figure 4-3 Raman spectra showing (A) the full region and (B) the low-frequency region for a dispersion of acid sonicated SWNTs. Three curves were compared: dispersion of dried purified SWNTs in water (a), two-stage dispersion into NaOH and H_2O (b), and dispersion in AOT aqueous solution (c).

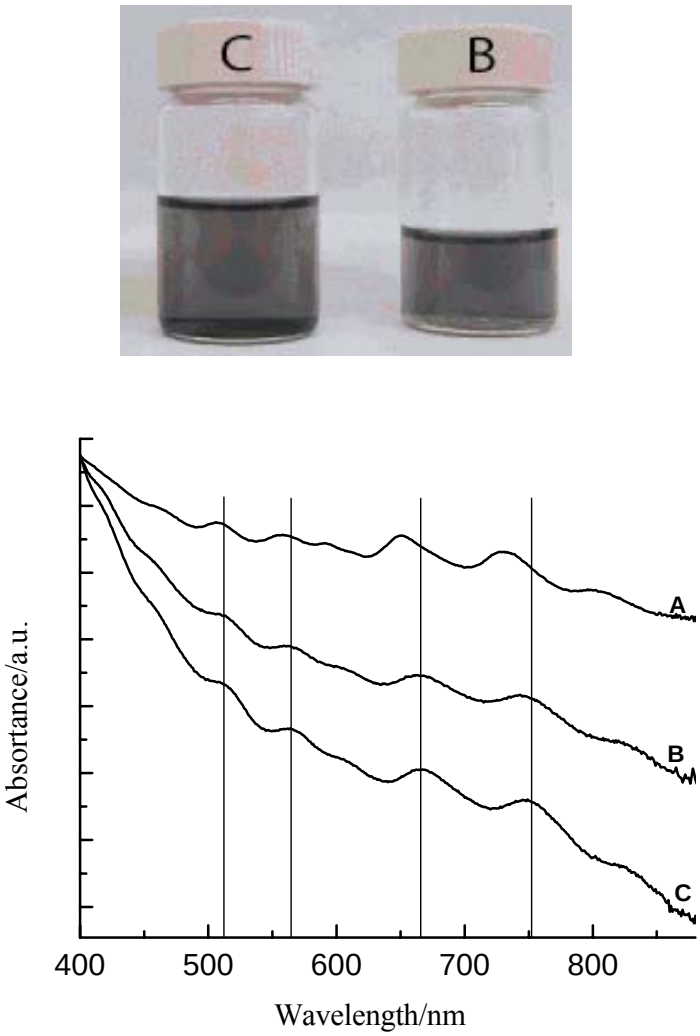

Figure 4-4 UV-Vis absorption spectra. Supernatants of 0.1 mg/mL SWNTs dispersed in (A) SDBS and (B) Chitosan after 2 h centrifugation at 29,000 g. (C) SWNT/CHI suspensions without centrifugation.

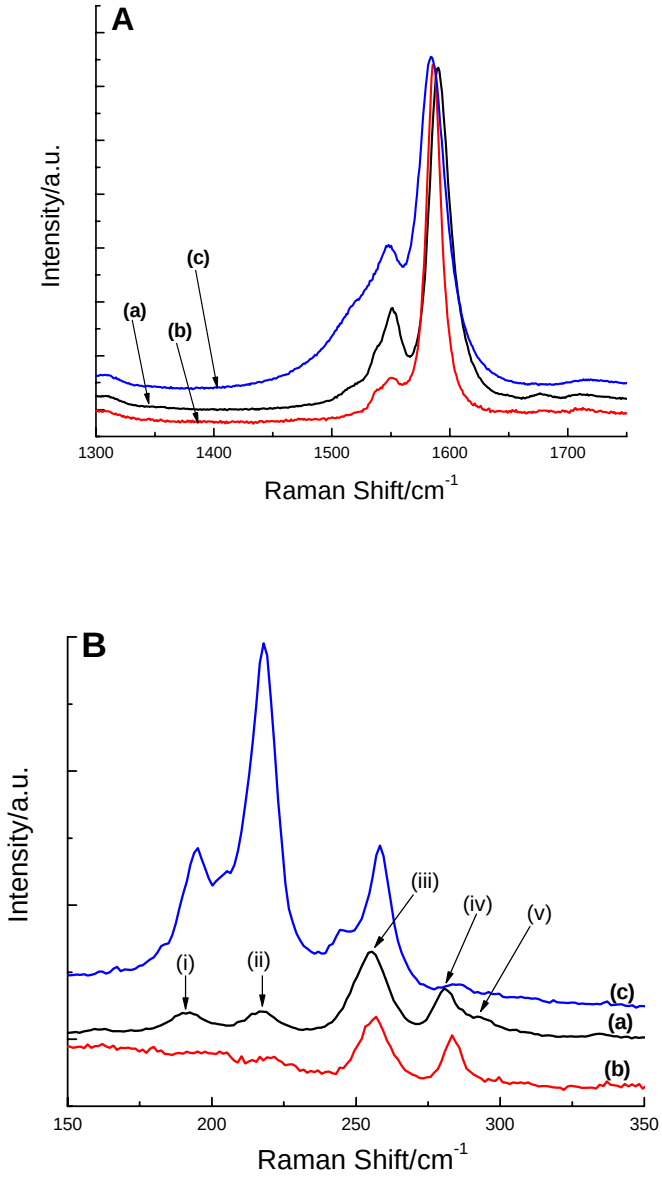

Figure 4-5 Raman spectra acquired using an excitation energy of 632.8 nm (1.96 eV). Part A shows the G and D bands, and Part B shows RBM low-frequency region of (a) as-received raw HiPco SWNTs, (b) supernatant of 0.1 mg/mL SWNT/CHI dispersion without centrifugation, and (c) precipitate of 0.1 mg/mL SWNT/CHI dispersion after standing overnight.

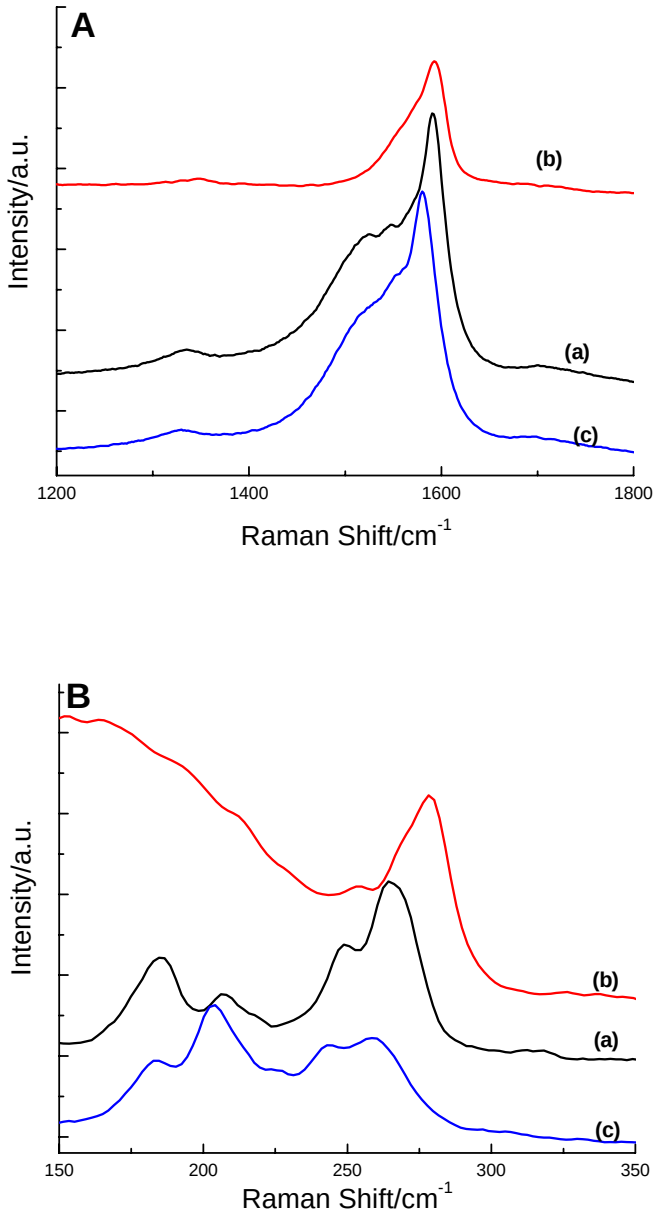

Figure 4-6 Raman spectra acquired using an excitation laser of 514.5 nm (2.41 eV). Part A shows the G and D bands, and Part B shows RBM low-frequency region of (a) as-received raw HiPco SWNT, (b) supernatant of 0.1 mg/mL SWNT/CHI dispersion without centrifugation, and (c) precipitate of 0.1 mg/mL SWNT/CHI dispersion after standing overnight.

Table 5 List of RBM bands observed using 632.8 (1.96 eV) and 514.5 (2.41 eV) nm laser excitation energies. Semiconducting nanotubes are denoted as S, and metallic nanotubes are denoted as M. The assignment of the indices is based on the predictions in calculation shown in Chapter 2.

Exp ν (cm^{-1})	d (nm)	(n,m) prediction	Type of tube	Samples	E_{EX} (eV)
183	1.31	(10,9)	S	precipitate	2.41
185	1.30	(14,4)	S	HiPco	2.41
191	1.25	(11,7) or (14,3)	S	HiPco	1.96
195	1.22	(13,4)	M	precipitate	1.96
203	1.17	(9,8) or (13,3)	S	precipitate	2.41
206	1.16	(14,1)	S	HiPco	2.41
217	1.09	(12,3)	M	HiPco	1.96
217	1.09	(12,3)	M	precipitate	1.96
242	0.97	(9,5)	S	precipitate	2.41
244	0.97	(7,7)	M	precipitate	1.96
249	0.95	(12,0)	M	HiPco	2.41
252	0.93	(10,3)	S	Supernatant	2.41
255	0.92	(9,4) or (11,1)	S	HiPco	1.96
256	0.92	(9,4) or (11,1)	M	Supernatant	1.96
257	0.91	(11,1)	S	precipitate	2.41
257	0.91	(9,4) or (11,1)	S	precipitate	1.96
265	0.89	(10,2)	S	HiPco	2.41
278	0.84	(8,4)	S	Supernatant	2.41
281	0.83	(10,1)	M	HiPco	1.96
283	0.83	(7,5)	S	Supernatant	1.96
286	0.82	(6,6)	M	precipitate	1.96
294	0.79	(10,0)	S	HiPco	1.96

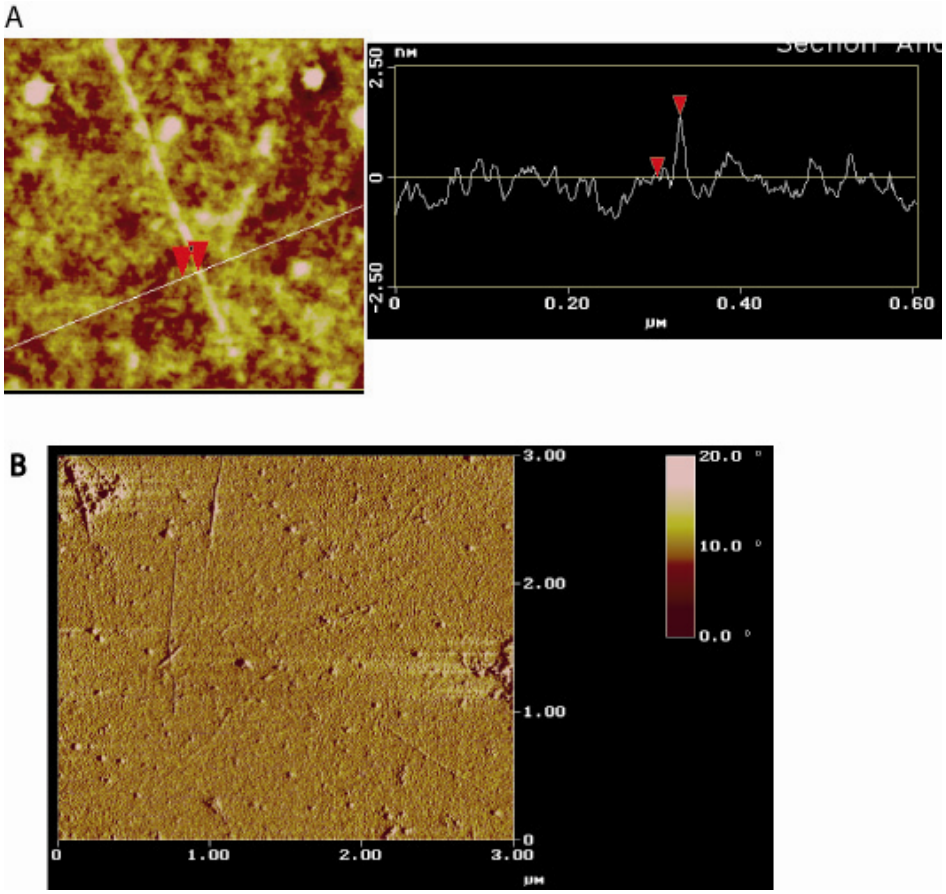

Figure 4-7 Tapping-mode AFM image of 0.1 mg/mL SWNTs dispersed in 0.5 wt% chitosan (CHI) aqueous solution after 2 h centrifugation on a mica substrate. (A) The height of the CHI-wrapped-SWNT is ca. 1.22-1.48 nm. (B) The phase image shows the well-dispersed SWNT/CHI on a mica substrate.

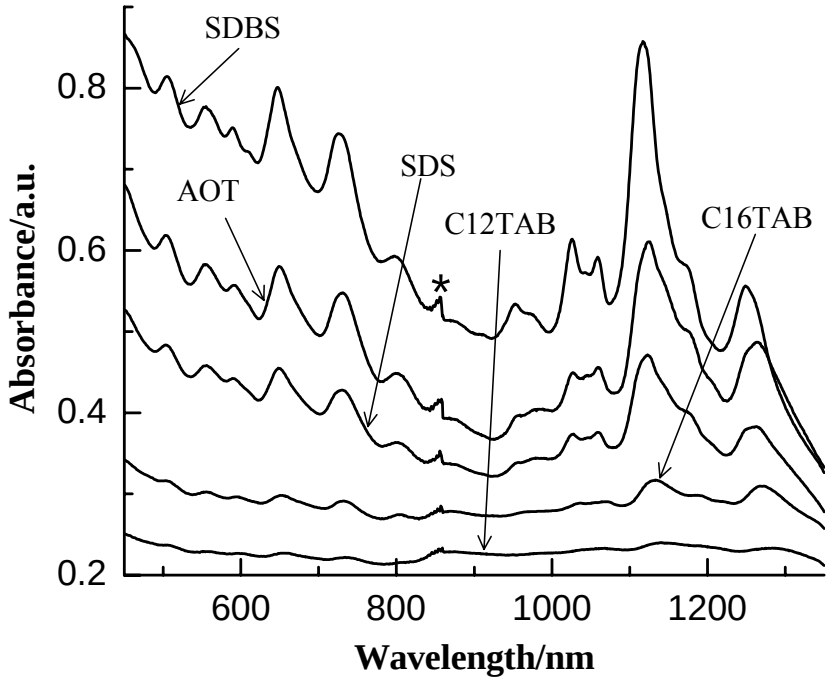

Figure 4-8 Comparison of the solubility of various surfactants. Absorption spectra of 1.0 mg/mL SWNTs dispersed in 0.5 wt% of different surfactants. The anionic surfactants used are AOT, SDBS, and SDS, whereas the cationic surfactants used are C12TAB and C16TAB. The anionic surfactants display better solubility for SWNTs than cationic surfactants from the optical absorption spectra. The asterisk marks the point where the lamp is changed.

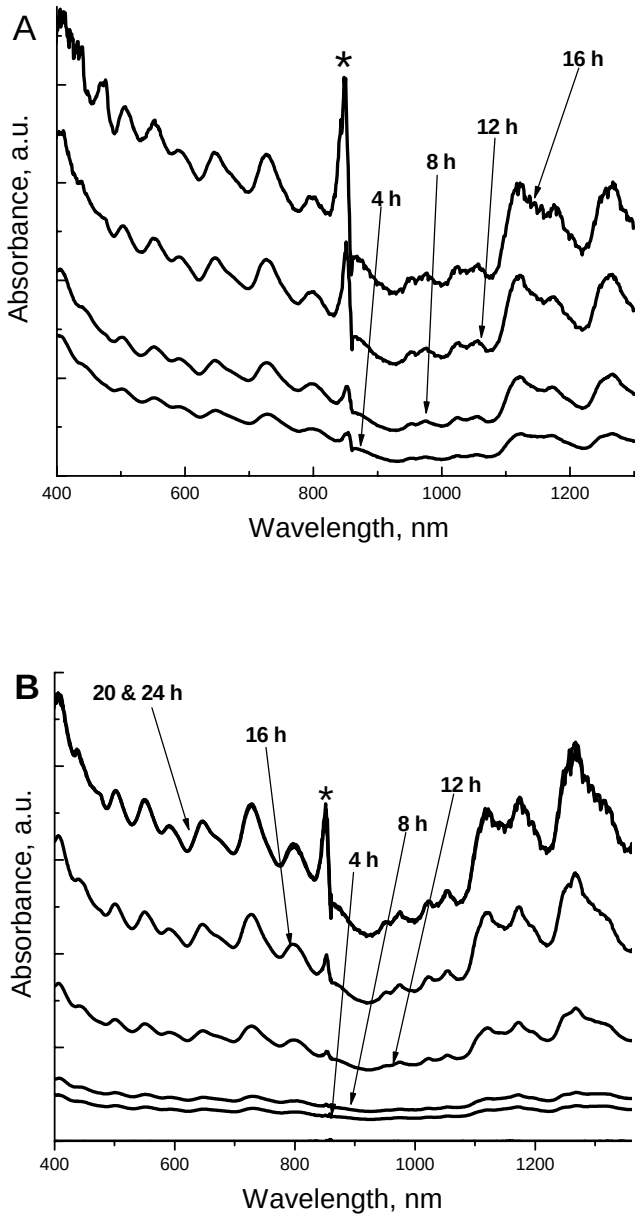

Figure 4-9 Effect of sonication time. Two different HiPco SWNT samples were used. Individual SWNTs are seen after 8h sonication for purified tubes (A), but 16 h sonication is required to individualize raw SWNTs (B). Raw-SWNTs do not show any significant improvement in dispersion upon sonication for 20 h. The asterisk marks the point where the lamp is changed at 860 nm.

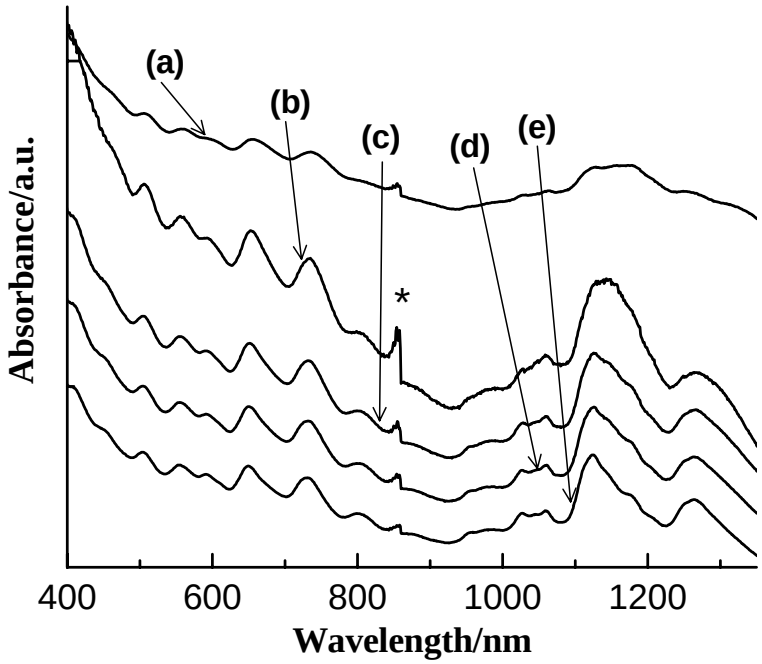

Figure 4-10 Comparison of the centrifugation times. Absorption spectra of (a) 0.1 mg/mL of SWNTS without centrifugation and 1 mg/mL of SWNTs with centrifugation for durations of (b) 1 h, (c) 2 h, (d) 3 h, and (e) 6 h. In all cases, a 0.5 wt% AOT aqueous solution was used. The intensity of absorption spectrum in (a), which corresponds to the smallest amount of SWNTs in solution (as a result of the initial concentration) and for 0 hours centrifugation (i.e., no centrifugation), has been increased for presentation purposes.

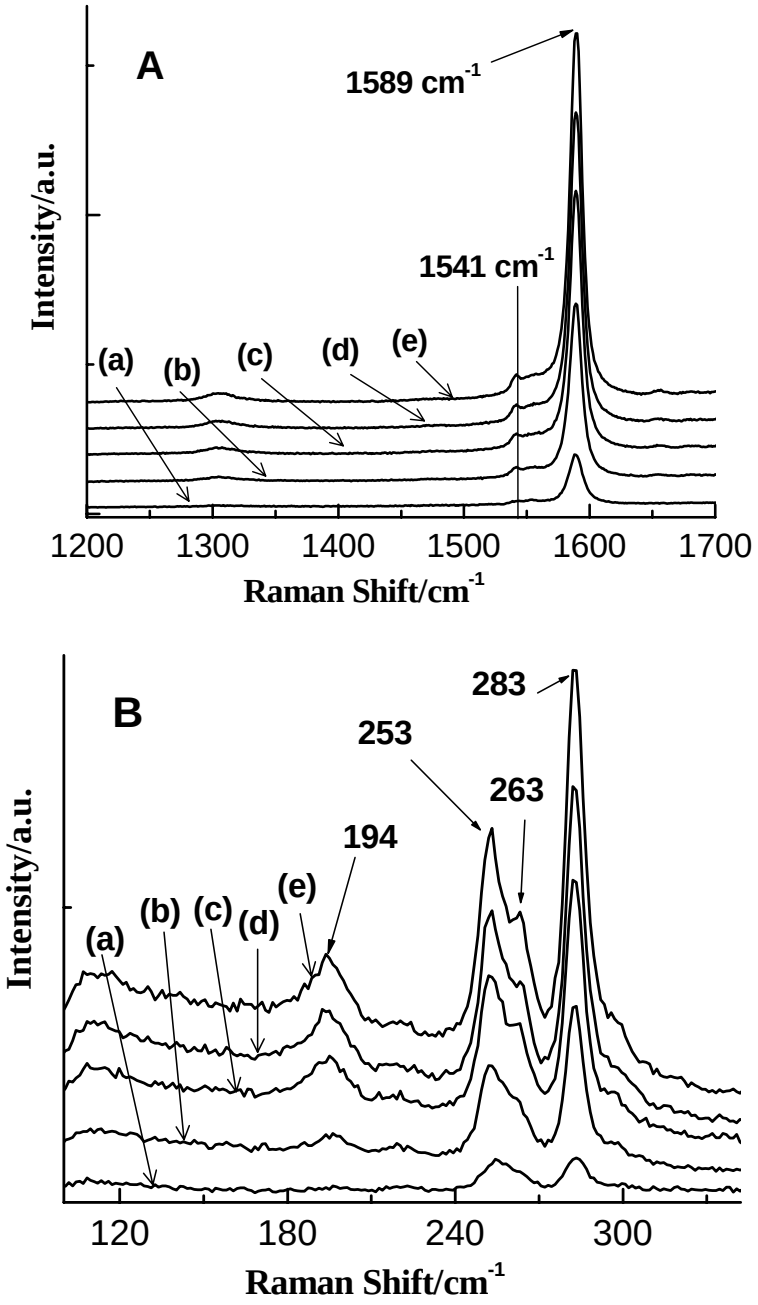

Figure 4-11 Evaluation of the centrifugation time. Raman spectra of dispersions of SWNTs centrifuged for (a) 0, (b) 1, (c) 2, (d) 3, and (e) 6 h at 29 000 g with excitation frequency of 632.8 nm. (A) High-frequency region showing no spectral change for various centrifugation durations. (B) Low-frequency region revealing growth of two vibration bands (ca. 253 and 263 cm^{-1}) with increase in centrifugation duration.

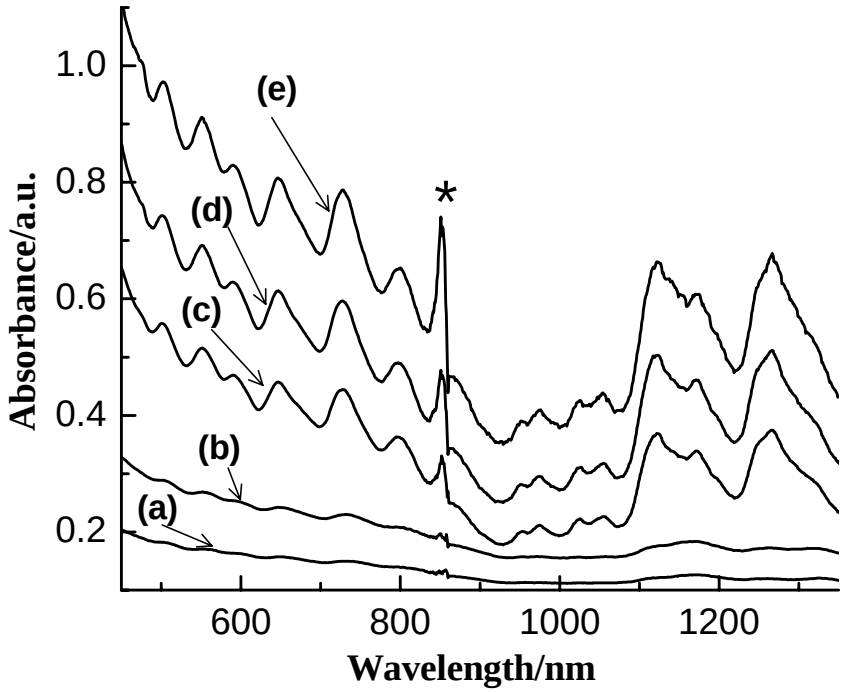

Figure 4-12 Evaluation of critical micelle concentration. Absorption spectra of suspension of HiPco SWNTs in AOT solution as a function of the AOT concentration (a) 0.05, (b) 0.10, (c) 0.20, (d) 0.50, and (e) 1.00 wt%; note the critical micelle concentration (CMC) of AOT is 0.12 wt% in aqueous solutions. The asterisk indicates lamp change upon switching from the visible to the near-IR region.

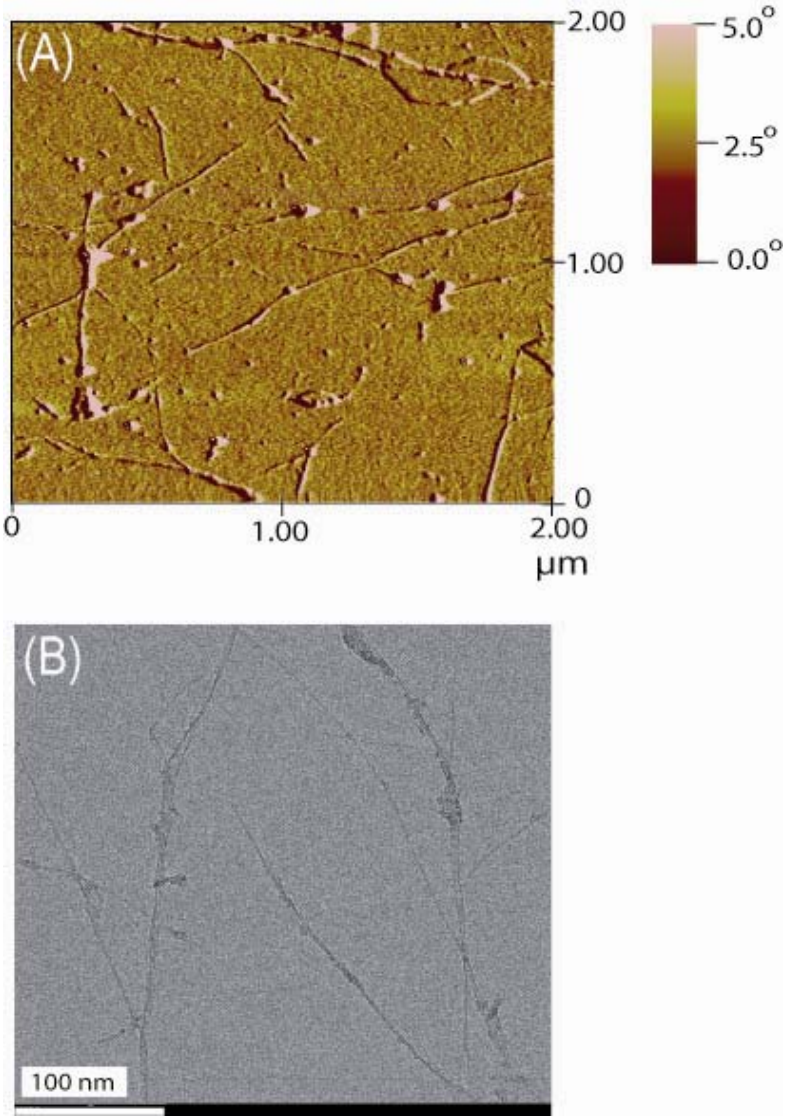

Figure 4-13 (A) Tapping-mode AFM phase image of 1 mg/mL SWNTs dispersed in 0.5 wt% AOT aqueous solution after 6 h centrifugation. (B) TEM image obtained for isolated SWNTs wrapped by AOT surfactant molecules.

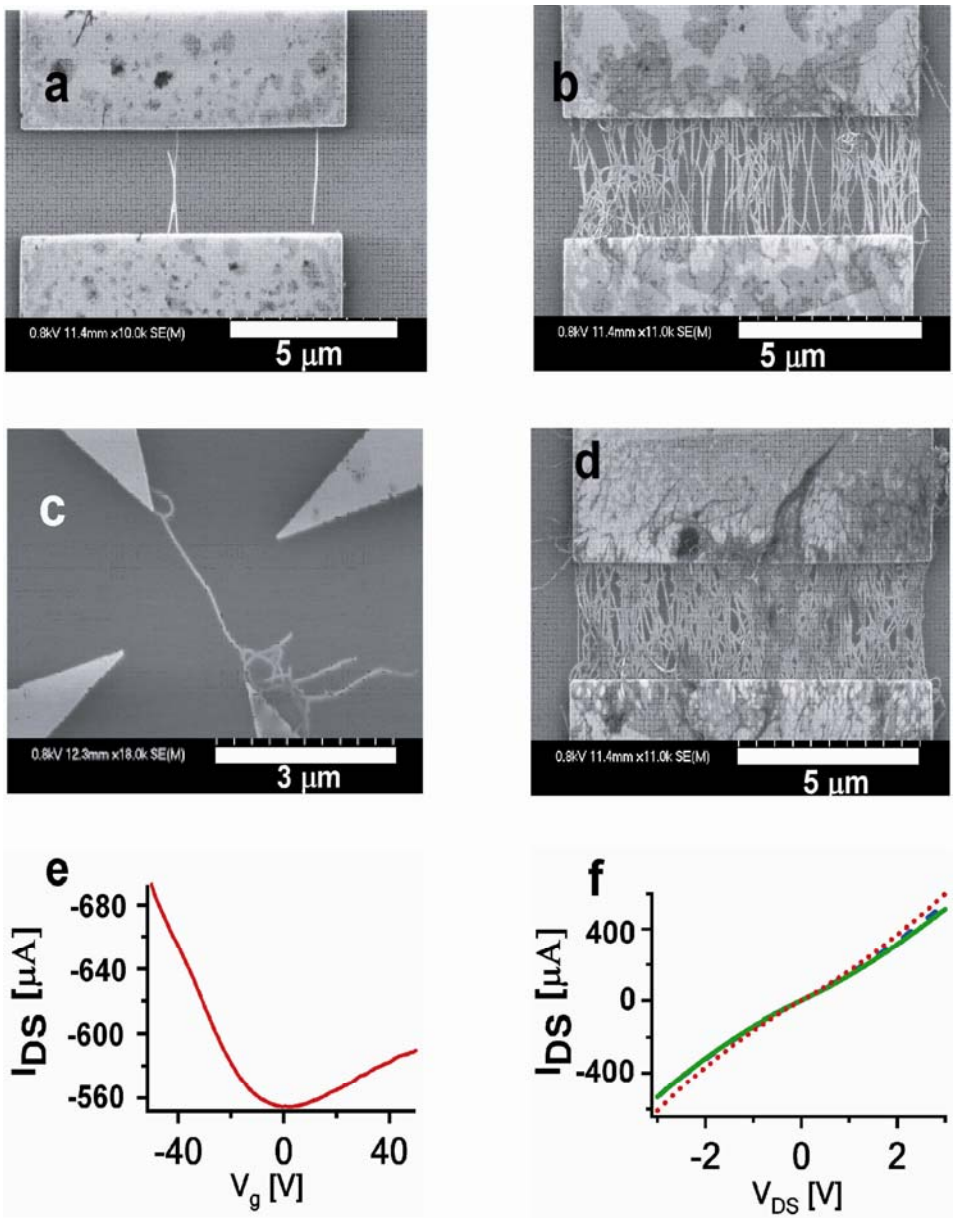

Figure 4-14 (a),(b),(d) SEM images of SWNTs aligned across a 3 µm gap by AC dielectrophoresis. The deposition times are (a) 1 min, (b) 4 min, (d) 5 min. The electrodes are 10 µm wide. (c) SEM image of SWNTs aligned across a 3 µm gap with a pointed geometry. (e) Plot of the drain—source current versus the gate voltage for the device shown in (d). The device shows ambipolar characteristics. The Si substrate is used as a back gate. V_{DS} is kept fixed at 3 V. The sample has been annealed at 300 °C under nitrogen. (f) Plot of the drain—source current versus V_{DS} at three different gate voltages. Red (dotted line): -50 V, Blue (dashed line): 50 V, Green (solid line): 0 V.

References

[1] A. Thess, R. Lee, P. Nikolaev, H. Dai, P. Petit, J. Robert, C. Xu, Y. H. Lee, S. G. Kim, A. G. Rinzler, D. T. Colbert, G. E. Scuseria, D. Tomanek, J. E. Fischer, R. E. Smalley, Crystalline Ropes of Metallic Carbon Nanotubes, Science, 273, 483 (1996).

[2] M.J. O'Connell, S.M. Bachilo, C.B. Huffman, V.C. Moore, M.S. Strano, E.H. Haroz, K.L. Rialon, P.J. Boul, W.H. Noon, C. Kittrell, J. Ma, R.H. Hauge, R.B. Weisman, R.E. Smalley, Band Gap Fluorescence from Individual Single-Walled Carbon Nanotubes, Science, 297, 593 (2002).

[3] S. Iijima, T. Ichihashi, Single-Shell Carbon Nanotubes of 1-nm Diameter, Nature, 363, 603 (1993).

[4] P.M. Ajayan, Nanotubes from Carbon, Chem. Rev., 99, 1787 (1999).

[5] P. Qi, O. Vermesh, M. Grecu, A. Javey, Q. Wang, H. Dai, S. Peng, K.J. Cho, Toward Large Arrays of Multiplex Functionalized Carbon Nanotube Sensors for Highly Sensitive and Selective Molecular Detection, Nano Lett., 3, 347 (2003).

[6] D.E. Milkie, C. Staii, S. Paulson, E. Hindman, A.T. Johnson, J.M. Kikkawa, Controlled Switching of Optical Emission Energies in Semiconducting Single-Walled Carbon Nanotubes, Nano Lett., 5, 1135 (2005).

[7] A. Star, Y. Lu, K. Bradley, G. Gru1ner, Nanotube Optoelectronic Memory Devices, Nano Lett., 4, 1587 (2004).

[8] Q. Lu, J.M. Moore, G. Huang, A.S. Mount, A.M. Rao, L.L. Larcom, P.C. Ke, RNA Polymer Translocation with Single-Walled Carbon Nanotubes, Nano Lett., 4, 2473 (2004).

[9] H-M. So, K. Won, Y.H. Kim, B-K. Kim, B.H. Ryu, P.S. Na, H. Kim, J.-O Lee, Single-Walled Carbon Nanotube Biosensors using Aptamers as Molecular Recognition Elements, J. Am. Chem. Soc., 127, 11906 (2005).

[10] T. Murakami,; K. Ajima,; J. Miyawaki,; M. Yudasaka,; S. Iijima,; K. Shiba, Drug-Loaded Carbon Nanohorns: Adsorption and Release of Dexamethasone in Vitro, Molecular Pharmaceutics, 1, 399 (2004).

[11] B. Zhao, H. Hu, S.K. Mandal, R.C. Haddon, A Bone Mimic Based on the Self-Assembly of Hydroxyapatite on Chemically Functionalized Single-Walled Carbon Nanotubes, Chem. Mater., 17, 3235 (2005).

[12] S. Banerjee, T. Hemraj-Benny, S.S. Wong, Covalent Surface Chemistry of Single-Walled Carbon Nanotubes, Adv. Mater., 17, 17 (2005).

[13] A. Star, Y. Liu, K. Grant, L. Ridvan, J.F. Stoddart, D.W. Steuerman, M.R. Diehl, A. Boukai, J.R. Heath, Noncovalent Side-Wall Functionalization of Single-Walled Carbon Nanotubes, Macromolecules, 36, 553 (2003).

[14] C.A. Dyke, J.M. Tour, Covalent Functionalization of Single-Walled Carbon Nanotubes for Materials Applications, J. Phys. Chem., 108, 1115 (2004).

[15] Y. Lin, S. Taylor, H. Li, K.A. Shiral Fernando, L. Qu, W. Wang, L. Gu, B. Zhou, Y. Sun, Advances Toward Bioaplications of Carbon Nanotubes, J. Mater. Chem., 14, 527 (2004).

[16] C.A. Dyke, M.P. Stewart, J.M. Tour, Separation of Single-Walled Carbon Nanotubes on Silica Gel. Materials Morphology and Raman Excitation Wavelength Affect Data Interpretation, J. Am. Chem. Soc., 127, 4497 (2005).

[17] S. Bandow, A.M. Rao, K.A. Williams, A. Thess, R.E. Smalley, P.C. Eklund, Purification of Single-Walled Carbon Nanotubes by Microfiltration, J. Phys. Chem. B, 101, 8839 (1997).

[18] K.B. Shelimov, R.O. Esenaliev, A.G. Rinzler, C.B. Huffman, R.E. Smalley, Purification of Single-Walled Carbon Nanotubes by Ultrasonicaly Assisted Filtration, Chem. Phys. Lett., 282, 429 (1998).

[19] Y. Xu, H. Peng, R.H. Hauge, R.E. Smalley, Controlled Multistep Purification of Single-Walled Carbon Nanotubes, Nano Lett., 5, 163 (2005).

[20] A.G. Rinzler, J. Liu, H.Dai, P. Nikolaev, C.B. Huffman, F.J. Rodríguez-Macías, P.J. Boul, A.H. Lu, D.Heymann, D.T. Colbert, R.S. Lee, J.E. Fischer, A.M.Rao, P.C. Eklund3 R.E. Smalley, Large-Scale Purification of Single-Walled Carbon Nanotubes: Process, Product, and Characterization, Appl. Phys. A 67, 29 (1998).

[21] Y. Li, X. Zhang, J. Luo, W. Huang, J. Cheng, Z. Luo, T. Li, F. Liu, G. Xu, X. Ke, L. Li, H. J. Geise, Purification of CVD Synthesized Single-Walled Carbon Nanotubes by Different Acid Oxidation Treatments, Nanotechnology, 15, 1645 (2004).

[22] Y. Kim, D.E. Luzzi, Purification of Pulsed Laser Synthesized Single Wall Carbon Nanotubes by Magnetic Filtration, J. Phys. Chem. B, 109, 16636 (2005).

[23] Q. Chen, C. Saltiel, S. Manickavasagam, L.S. Schadler, R.W. Siegel, H. Yang, Aggregation Behavior of Single-Walled Carbon Nanotubes in Dilute Aqueous Suspension, J. of Colloid and Interface Science, 280, 91 (2004).

[24] M. Zhang, M. Yudasaka, S. Iijima, Diameter Enlargement of Single-Wall Carbon Nanotubes by Oxidation, J. Phys. Chem. B, 108, 149 (2004).

[25] J.G. Wiltshire, A.N. Khlobystov, L.J. Li, S.G. Lyapin, G.A.D. Briggs, R.J. Nicholas, Comparative Studies on Acid and Thermal Based Selective Purification of HiPco Produced Single-Walled Carbon Nanotubes, Chem. Phys. Lett., 386, 239 (2004).

[26] T. Ramanathan, F.T. Fisher, R.S. Ruoff, L.C. Brinson, Amino-Functionalized Carbon Nanotubes for Binding to Polymers and Biological Systems, Chem. Mater., 17, 1290 (2005).

[27] M. Shim, A. Javey, N. Wong, S. Kam, H. Dai, Polymer Functionalization for Air-Stable n-Type Carbon Nanotube Field-Effect Transistors, J. Am. Chem. Soc., 123, 11512 (2001).

[28] C. Wu, P. Wang, X. Yao, C. Liu, D. Chen, G.Q. Lu, H. Cheng, Effects of SWNT and Metallic Catalyst on Hydrogen Absorption/Desorption Performance of MgH2, J. Phys. Chem. B, 109, 22217 (2005).

[29] S.S. Wong, E. Joselevich, A.T. Woolley, C.L. Cheung, C.M. Lieber, Covalently Functionalized Nanotubes as Nanometresized Probes in Chemistry and Biology, Nature, 394, 52 (1998).

[30] M. Panhuis, A. Maiti, A.B. Dalton, A. Noort, J.N. Coleman, B. McCarthy, W.J. Blau, Selective Interaction in a Polymer-Single-Walled Carbon Nanotube Composite, J. Phys. Chem. B, 107, 478 (2003).

[31] S.C. Lyu, B.C. Liu, S.H. Lee, C.Y. Park, H.K. Kang, C.W. Yang, C.J. Lee, Large-Scale Synthesis of High-Quality Single-Walled Carbon Nanotubes by Catalytic Decomposition of Ethylene, J. Phys. Chem. B, 108, 1613 (2004).

[32] P. Ramesh, N. Kishi, T. Sugai, H. Shinohara, High-Yield Synthesis of Single-Wall Carbon Nanotubes on MCM41 using Catalytic Chemical Vapor Deposition of Acetylene, J. Phys. Chem. B, 110, 13 (2006).

[33] S. Banerjee, S.S. Wong, Demonstration of Diameter-Selective Reactivity in the Sidewall Ozonation of SWNTs by Resonance Raman Spectroscopy, Nano Lett., 4, 1445 (2004).

[34] X. Zhang, T.V. Sreekumar, T. Liu, S. Kumar, Properties and Structure of Nitric Acid Oxidized Single Wall Carbon Nanotube Films, J. Phys. Chem. B, 108, 16435 (2004).

[35] K.H. An, J.S. Park, C.-M. Yang, S.Y. Jeong, S.C. Lim, C. Kang, J-H. Son, M.S. Jeong, Y.H. Lee, A Diameter-Selective Attack of Metallic Carbon Nanotubes by Nitronium Ions, J. Am. Chem. Soc., 127, 5196 (2005).

[36] D. Chattopadhyay, I. Galeska, F. Papadimitrakopoulos, A Route for Bulk Separation of Semiconducting from Metallic Single-Wall Carbon Nanotubes, J. Am. Chem. Soc., 125, 3370 (2003).

[37] C.A. Dyke, M.P. Stewart, J.M. Tour, Separation of Single-Walled Carbon Nanotubes on Silica Gel. Materials Morphology and Raman Excitation Wavelength Affect Data Interpretation Affect Data Interpretation, J. Am. Chem. Soc., 127, 4497 (2005).

[38] V.V. Didenko, V.C. Moore, D.S. Baskin, R.E. Smalley, Visualization of Individual Single-Walled Carbon Nanotubes by Fluorescent Polymer Wrapping, Nano Lett., 5, 1563 (2005).

[39] S.M. Keogh, T.G. Hedderman, P. Lynch, G.F. Farrell, H.J. Byrne, Bundling and Diameter Selectivity in HiPco SWNTs Poly(P-Phenylene Vinylene-Co-2,5-Dioctyloxy-M-Phenylene Vinylene) Composites, J. Phys. Chem. B, 110, 19369 (2006).

[40] H. Yang, S.C. Wang, P. Mercier, D.L. Akins, Diameter-Selective Dispersion of Single-Walled Carbon Nanotubes using a Water-Soluble, Biocompatible Polymer, Chem. Commun., 1425 (2006).

[41] T.W. Odom, J-L. Huang, P. Kim, C.M. Lieber, Structure and Electronic Properties of Carbon Nanotubes, J. Phys. Chem. B, 104, 2794 (2000).

[42] A. Star, J.F. Stoddart, D. Steuerman, M. Diehl, A. Boukai, E.W. Wong, X. Yang, S-W. Chung, H. Choi, J.R. Heath, S.-W. Chung, H. Choi, J.R. Heath, Preparation and Properties of Polymer-Wrapped Single-Walled Carbon Nanotubes, Angew. Chem. Int. Ed., 40, 1721 (2001).

[43] M.S. Dresselhaus, G. Dresselhaus, R. Saito, A. Jorio, Raman Spectroscopy of Carbon Nanotubes, Phys. Rep., 409, 47 (2005).

[44] S.M. Bachilo, M.S. Strano, C. Kittrell, R.H. Hauge, R.E. Smalley, R.B. Weisman, Structure-Assigned Optical Spectra of Single-Walled Carbon Nanotubes, Science, 298, 2361 (2002).

[45] R. Krupke, F. Hennrich, H. v. Lo¨hneysen, M.M. Kappes, Separation of Metallic from Semiconducting Single-Walled Carbon Nanotubes, Science, 301, 344 (2003).

[46] S.C. Wang, H. Yang, D.L. Akins, Solubilization of Single-Wall Carbon Nanotubes using Aerosol OT, Polymer Preprints, 46(1), 226 (2005).

[47] N. Zhou, Q. Li, J. Wu, J. Chen, S. Weng, G. Xu, Spectroscopic Characterization of Solubilized Water in Reversed Micelles and Microemulsions: Sodium Bis(2-Ethylhexyl) Sulfosuccinate and Sodium Bis(2-Ethylhexyl) Phosphate in n-Heptane, Langmuir, 17, 4505 (2001).

[48] J. Jang, H. Yoon, Facile Fabrication of Polypyrrole Nanotubes using Reverse Microemulsion Polymerization, Chem. Comm., 720 (2003).

[49] S.S. Shankar, S. Chatterjee, M. Sastry, Synthesis of CdS Nanoparticles within Thermally Evaporated Aerosol OT Thin Films, PhysChemComm, 6, 36–39 (2003).

[50] P.T. Callaghan, O.J. Soderman, Examination of the Lamellar Phase of Aerosol OT/Water using Pulsed Field Gradient Nuclear Magnetic Resonance, Phys. Chem., 87, 1737 (1983).

[51] V.C. Moore, M.S. Strano, E.H. Haroz, R.H. Hauge, R.E. Smalley, Individualy Suspended Single-Wall Carbon Nanotubes in Various Surfactants, Nano Lett., 3, 1379 (2003).

[52] M.F. Islam, E. Rojas, D.M. Bergey, A.T. Johnson, A.G. Yodh, High Weight Fraction Surfactant Solubilization of Single-Walled Carbon Nanotubes in Water, Nano Lett., 3, 269 (2003).

[53] B. Benedict, P.E. Pehrsson, W. Zhao, Optically Sensing Additional Sonication Effects on Dispersed HiPco Nanotubes in Aerated Water, J. Phys. Chem. B, 109, 7778 (2005).

[54] H. Jia, Y. Lian, M. O. Ishitsuka, T. Nakahodo, Y. Maeda, T. Tsuchiya, T. Wakahara, T. Akasaka, Centrifugal Purification of Chemically Modified Single-Walled Carbon Nanotubes, Sci. Tech. Adv. Mat., 6, 571 (2005).

[55] A.G. Ryabenko, T.V. Dorofeeva, G.I. Zvereva, UV–VIS–NIR Spectroscopy Study of Sensitivity of Single-Wall Carbon Nanotubes to Chemical Processing and Van-der-Waals SWNT/SWNT Interaction. Verification of the SWNT Content Measurements by Absorption Spectroscopy, Carbon, 42, 1523 (2004).

[56] M.S. Strano, C.A. Dyke, M.L. Usrey, P.W. Barone, M.J. Allen, H. Shan, C. Kittrell, R.H. Huge, J.M. Tour, R.E. Smalley, Electronic Structure Control of Single-Walled Carbon Nanotube Functionalization, Science, 301, 1519 (2003).

[57] V.C. Moore, M.S. Strano, E.H. Haroz, R.H. Hauge, R.E. Smalley, J. Schmidt, Y. Talmon, Individually Suspended Single-Walled Carbon Nanotubes in Various Surfactants, Nano Lett., 3, 1379 (2003).

[58] W. Wenseleers, I.I. Vlasov, E. Goovaerts, E.D. Obraztsova, A.S. Lobach, A. Bouwen, Efficient Isolation and Solubilization of Pristine Single-Walled Nanotubes in Bile Salt Micelles, Adv. Funct. Mater., 14, 1105 (2004).

[59] Y. Lian, Y. Maeda, T. Wakahara, T. Nakahodo, T. Akasaka, S. Kazaoui, N. Minami, T. Shimizu, H. Tokumoto, Spectroscopic Study on the Centrifugal Fractionation of Soluble Single-Walled Carbon Nanotubes, Carbon, 43, 2750 (2005).

[60] R. Saito, G. Dresselhaus, M.S. Dresselhaus, Trigonal Warping Effect of Carbon Nanotubes, Phys. Rev. B, 61, 2981(2000).

[61] F. Hennrich, R. Krupke, S. Lebedkin, K. Arnold, R. Fischer, D.E. Resasco, M.M. Kappes, Raman Spectroscopy of Individual Single-Walled Carbon Nanotubes from Various Sources, J. Phys. Chem. B, 109, 10567 (2005).

[62] B.P. Binks, W-G. Cho, P.D.I. Fletcher, D.N. Petsev, Stability of Oil-in-Water Emulsions in a Low Interfacial Tension System, Langmuir, 16, 1025 (2000).

[63] O. Matarredona, H. Rhoads, Z. Li, J.H. Harwell, L. Balzano, D.E. Resasco, Dispersion of Single-Walled Carbon Nanotubes in Aqueous Solutions of the Anionic Surfactant NaDDBS, J. Phys. Chem. B., 107, 13357 (2003).

[64] S. Banerjee, B. White, L. Huang, B.J. Rego, S. O'Brien, I.P. Herman, Precise Positioning of Single-Walled Carbon Nanotubes by AC Dielectrophoresis, J. Vac. Sci. Technol. B, 24, 3173 (2006).

[65] Y. Kim, S. Hong, S. Jung, M.S. Strano, J. Choi, S. Baik, Dielectrophoresis of Surface Conductance Modulated Single-Walled Carbon Nanotubes using Catanionic Surfactants, J. Phys. Chem. B, 110, 1541 (2006).

[66] S.C. Wang, H. Yang, S. Banerjee, I.P. Herman, D.L. Akins, AOT Dispersed Single-Walled Carbon Nanotubes for Transistor Device Application, Mater. Lett., doi:10.1016/j.matlet.2007.07.001 (2007).

5

Synthesis and Characterization of Nanoparticles

For single-walled carbon nanotubes (SWNTs) to have widespread practical applications, they need to be incorporated into nanocomposites with other materials. One major thrust of our research has been the interaction and/or intercalation of SWNTs with nanoparticles. In this chapter, the conceptual properties of nanoparticles are introduced, and the methods of synthesizing different nanoparticles are discussed. Our overall goal is to develop methods for the manipulation of nanoparticles to facilitate them in carbon nanotube nanocomposites.

Nanoparticles (NPs) have been synthesized for semiconducting, metallic, and magnetic materials. A wide variety of synthesis procedures have been used to produce these particles. Different synthesis methods are likely to be useful for applications in industry. In my project, the primary synthesis method involves the use of reverse micelle microemulsion systems to synthesize metallic (e.g. Au, Fe) or semiconducting NPs (e.g. ZnS, CdS). In the reverse micelle system, control of the particle sizes depends on the molar ratio (ω_o) of water to the surfactant, [W]/[S], in water-in-oil (w/o) microemulsions. Micellization (micelle formation) provides an attractive route for the synthesis of NPs; the micellization approach can be modified to get NPs with a desired size. NPs encapsulated in reverse micelles are also able to interact with polymers and biological species. Core-shell structures are often used where the NPs are coated with an external inorganic or organic layer. The core-shell system is used in my project as a post-synthesis method for surface modification of the NPs. The sol-gel system is common by used to for synthesize metallic magnetic iron NPs (Fe_2O_3).

5.1 Introduction

Over the last decades, much more attention has been focused on the design and synthesis of materials with at least one dimension less than 100 nm. The novel materials are expected to find use in aeronautics, biology, chemistry, electronics, medicine, physics, etc. There are two approaches for synthesizing new materials. One approach is the “top-

down" route. The top-down approach involves the pattering (using lithography) of bulk materials into nanometer-sized structures, as commonly performed in the semiconductor industry to build integrated circuits. This top-down mechanism has greatly benefited from the invention of the scanning tunneling microscope (STM) at the IBM Zurich laboratory in Switzerland, 1981. The STM is capable of higher resolution than the atomic force microscope (AFM). In STM, weak electric currents are detects, allowing for the visualization of high electron density occurs. Hence, STM can be used to observe the position of individual atoms and molecules on the surface of a lattice, and position the individual atoms to create a certain pattern for the electrodevices. Another approach is the "bottom-up" route. The bottom-up approach involves the fabrication of materials atom by atom and then layer by layer in self-assembly methods. In my project, the bottom-up route is used to synthesize NPs of desired diameter sizes.

NPs of different materials tend to exhibit interesting electronic, optical, and magnetic properties. Hence there has been a lot of attention devoted NPs over the past few decades. Many academic and industrial groups have attempted to incorporate different types of NPs with different sizes in commercial products. Especially, in the past decade, the improvements in the preparation techniques and characterization of NPs have facilitated their incorporation in applications such as photodectectors [1], optical devices [2], and drug delivery [3]. NPs can be classified according to the materials which as metals, insulators, and semiconductors [4] based on the electronic properties of solids, illustrated in Figure 5-1A. The NPs display conducting metal property when the lowest conduction band is incompletely filled with electrons or the empty conduction band is overlapped with electrons from the filled valence band such as alkaline earth metals.

When the highest valence band is completely filled, and electrons become immobilized and are not able to be excited to the conduction band with a larger band gap, the NPs become an insulator without conductivity (e.g. diamond). Semiconductors have a character that will allow electrons to jump to the conduction band from the packed valence band when thermal energy is applied [5], and a hole is produced. The character of electron-hole relationship in semiconductor can produce a doping process. The purpose of doping impure materials into intrinsically pure semiconductors is to change its electronic property. It is one of the most important techniques for searching new semiconductor materials. Figure 5-1A shows two types of doping intrinsic semiconductor to n-type or p-type doped semiconductors. Group IV elements (e.g. Silicon) doped with group III elements (e.g. B) will produce p-type semiconductors. Since group III dopant can be treated as positive holes contributor that will excite electrons from pure semiconductor to jump into these mobile holes, hence leaving the hole behind in the valence band of group IV. On the contrary, n-type doping of semiconductors is doping Si with group V elements that contribute extra electrons to elevate the Fermi energy level of Si.

Semiconducting NPs, e.g. ZnS and CdS, have been attached to SWNTs to form novel nanocomposite. The metallic magnetic NPs, containing Fe or Mn, have been extensively investigated. Additionally, metallic Au NPs have been synthesized with distinct plasmon feature in the optical spectra. The different types of NPs are being introduced in the subsequent sections.

5.1.1 Semiconducting Nanoparticles

Semiconducting NPs, compounds of II-IV elements in periodic table, are luminescent nanoparticles with semiconductor properties that can also be called quantum dots (QDs) or Q particles [6]. It is not clear when or who should be credited with the discovery of QDs. The first discoveries of QDs can be traced to the studies of semiconductors at Bell Laboratories starting in 1947. One of the earliest published articles on semiconducting NPs was by Bergstresser and Cohen [7] in 1967, in which they described the electronic structure and optical properties of nanoparticles of Group II-VI compound.

In Figure 5-1A, the small band gap between the highest fully occupied valence band and the lowest empty conduction band in QDs is shown . When crystalline QDs are excited by photons or thermal energy, the electron jumps from the highest occupied valence band (HOMO) to the lowest unoccupied conduction band (LUMO) producing a vacancy or an imaginary positive charge (hole), as illustrated in Figure 5-1B. This phenomenon results in the formation of an electron-hole (e-h) pair. Such an e-h pair is called an “exciton”. The definition of band gap energy in a QD is the energy that is enough to generate an exciton, but at the same time the gap is large enough that the Coulomb force is negligible. An optical property of QD is called quantum size effect [8] or quantum confinement effect, in which Group II-VI QDs exhibit different colors when the particle size is changed, as illustrated in Figure 5-1C. The change of band gap energy (Eg) is related to the inverse of the square of its radius (R^2) for a spherical quantum dot. The lowest interband transition energy of a spherical semiconducting NP has been calculated and reported by Brus [9], as shown in equation 1.

$$\mathrm{Eg} = \mathrm{E_{bulk}} + \frac{\hbar^2\pi^2}{2m_{eh}R^2} - \frac{1.8e^2}{\varepsilon R} + \frac{e^2}{R}\overline{\sum_{n=1}^{\infty}\alpha\left(\frac{S}{R}\right)^{2n}}$$

$$\text{, where} \qquad \frac{1}{m_{eh}} = \frac{1}{m_e} + \frac{1}{m_h} \qquad (1)$$

The E_{bulk} is the band gap energy of the bulk structure. m_e and m_h are denoted as the effective electron mass and hole mass, respectively. The third term of $\frac{1.8e^2}{\varepsilon R}$ corresponds to the Coulomb attraction potential, and the fourth term of $\frac{e^2}{R}\overline{\sum_{n=1}^{\infty}\alpha\left(\frac{S}{R}\right)^{2n}}$ corresponds to the solvation energy loss (polarization energy). The Coulomb attraction and polarization energies are at times negligible. However, the second term, $\frac{\hbar^2\pi^2}{2m_{eh}R^2}$, represents the localization of quantum energy, and implies that when the energy of the band gap increases, the size of the QDs will decrease. Large QDs often contain several excitons under optical excitation, and these e-h pairs will dissociate around room temperature. The quantum size effects have been examined in detail for CdSe quantum dots [10]. In a very small QD, generally only one exciton will be produced, and this e-h pair is subjected to spatial restrictions which will prevent its dissociation. In other words, the one and only one exciton is confined by the small size and shape of the QDs. The negative electron and positive hole are attracted to each other by Coulomb forces. This quantum confinement will cause the kinetic enhancement of the luminescence quantum yield as mentioned by Brus [10]. The high photoluminescence quantum yields are another important reason for the increasing interest in QDs. The quantum yield is a

measure of the extent to which absorbed photons are emitted as electromagnetic radiation. The luminescence quantum yield can be presented as the ratio of the emitted number of fluorescent photons to the absorbed number of incident photons, QY = $photons_{em}/photon_{abs}$.

The goal of our research has been to search for a stable procedure to synthesize CdS nanoparticles, and we have been particularly interested in controlling the size and shape of the CdS QDs. A method for the confinement of CdS NPs in mesoporous materials has been reported by our group [11]. Using materials with hexagonally arranged pores, MCM-41 and SBA-15, it is possible to directly impregnate the QDs inside the surface-modified mesoporous material. The sizes of CdS particles formed within the pores show that the different sizes are dependent on the molding structural magnitude of the pore size of the mesoporous materials. For MCM-41 and SBA-15, the size of the CdS NPs deduced by X-ray diffraction (XRD) using the Scherrer formula is found to be about 2.1 and 3.4 nm, respectively. Although uniform structures are obtained by this method, it is impractical to remove the calcined framework of mesoporous materials to obtain CdS NPs for further applications. To utilize NPs for device applications, thin films can be used to anchor NPs and immobilize them on substrates. A simple thin-film method had been developed using the Langmuir-Blodgett technique [12]. CdS can also be immobilized by using thermal evaporation in sodium bis(2-ethylhexyl) sulfosuccinate (Aerosol OT) thin films with H_2S gas as the sulfide source [13]. However, it is difficult to use thin films to interact with other compounds in solution for the synthesis of future composites. In our group, Xu and Akins have reported the use of reverse micelle microemulsions to encapsulate CdS with thioacetamide (CH_3CSNH_2) as

the sulfide source [14]. The as-synthesized CdS nanocrystals have been investigated by transmission electron microscopy (TEM), which shows the spherical uniformity of CdS quantum dots. However, the reverse micelle microemulsion system is a better method to prepare CdS particles because there is no need to remove supporting mesoporous materials. The preparation of CdS NPs on thin films is a simple method, but is lacking in flexibility for applications that do not require thin-film techniques. Therefore, we have chosen to use the microemulsion system in our research.

The reverse micelle microemulsion system is stable and easy to manipulate in the ambient environment [15]. To form well-dispersed quantum dot nanocrystals, anionic and cationic compounds can be separately used to react with reverse micelles to form separate microemulsion stock solutions. The two stock solutions can then be mixed with each other to form NPs. The method can be employed in synthesizing different types of nanoparticles, including metallic NPs. The mechanism by which NPs are synthesized in this process will be detailed in Section 5.2.

5.1.2 Metallic Nanoparticles

Metallic materials have many potential applications when their size is decreased to the nanometer region. Metallic NPs (Au, Ag, Cu, Fe, etc.) have generated great interest in the field of colloidal science due to their optical properties and their possible use in biomedical device applications. Furthermore, metallic NPs can be used to overcome the disadvantages of fluorescence-based dyes traditionally used in clinical diagnostic immunoassays. The color of fluorescence-based dyes fades away rather quickly, but luminescent colors generated from NPs last much longer. Gold NPs have been used in

many biosensor detection devices such as oral cancer diagnostics [16]. Au NPs can also be coated by silver NPs (Au@Ag) to improve the fluorescence properties for applications in medical diagnostics [17], since metal NPs have a better light scattering ability than traditional fluorophores and also do not suffer from photo-bleaching problems [16].

Recently, magnetic metallic NPs have attracted much interest for biomedical applications because of the unique magnetic and optical properties associated with them [18]. Materials can be classified according to their magnetic properties as diamagnetic (no unpaired electron, very weak magnetic properties), paramagnetic (one or more unpaired electrons,↑↘←↗↓↗→), ferrimagnetic (sublattice moments are not equal, ↑↓↑↓), antiferromagnetic (sublattice moments are equal but opposite, ↑↓↑↓), and ferromagnetic (strongest magnetic moment aligned in the same direction, ↑↑↑↑). Their unique magnetic properties pave the way for applications not possible with other metallic NPs. Many different approaches for preparing [19] and functionalizing [20] magnetic NPs have been developed for drug delivery and medical diagnostics applications [21]. In addition, gold NPs can interact with elemental Fe to form iron/gold core-shell nanocomposites (Fe_2O_3@Au or Fe_3O_4@Au) in which can be used for magnetic resonance imaging (MRI) applications [22, 23].

Metallic NPs have long been of interest to the biomedical community. There is a long history of using colloidal gold in medicine, and German bacteriologist Robert Koch, the recipient of the 1890 Nobel Prize, discovered that compounds mixed with gold can slow down bacterial growth. Much more research is needed to elucidate the properties and potential application enhancements of present diagnostic sensors, for inventing new protocols to detect early stage cancers, and for developing efficient drugs to accurately

deliver to target cells. Here, we discuss the synthesis of magnetic iron oxide NPs. The method of synthesizing iron oxide will be described in the following section.

5.2 Growth Mechanisms of Nanoparticles

Semiconductor nanocrystals with different sizes emit in different regions of the electromagnetic spectrum. The optical absorption spectra exhibit a red-shift with increasing nanoparticle size [24]. It is not difficult to synthesize NPs; nevertheless, it is daunting to find a stable synthesis method to obtain NPs that can be appropriately functionalized with other biological or chemical species for practical applications.

One way to synthesize NPs is through a colloidal system. A colloidal system consists of two main ingredients: (1) solid particles, and (2) dispersing media consisting of liquid solutions. Colloidal systems are essential to life; they exist in paints, ketchups, salad dressings, and many other products that are used in daily life. An important feature of a colloidal system is the surface charge on the particles. Particles with the same-charge repel each other, thus overcoming the tendency to aggregate and enabling the colloids to remain dispersed in the liquid. The smaller the size of each individual particle, the greater the total surface area and charge of the particle will be. The synthesis of colloidal particles incorporating therapeutic reagents is critical for various medical applications [25]. We have primarily used the colloidal reverse micelle microemulsion system to synthesize NPs. The protocol to stabilize the particle sizes has been developed. In addition, core-shell interactions have been used to modify the surfaces of NPs. The sol-gel method has also been explored to form nanocomposites with single-walled carbon nanotubes.

5.2.1 Reverse Micelle System

Micellization is the formation of colloidal clusters in a solution comprising of a surfactant (surface-active agent) dispersed in a liquid solvent. Many surfactants are amphipathic, that is, they possess a polar amphiphilic (or hydrophilic) head and nonpolar amphiphobic (or hydrophobic) tail(s). Surfactants can carry different charges on their head group, and depending on the charge they carry, they are classified as anionic surfactants (with a negative charge), cationic surfactants (with a positive charge), nonionic surfactants (without any charge), or zwitterionic surfactants (with both negative and positive charges). For surfactants to achieve thermodynamic equilibrium in solution, the following sequence of events must occur: (1) dissolution of solid bulk surfactants in a solvent, (2) aggregation of dissolved surfactants into a micellar phase, (3) adsorption of dissolved surfactants at the surface of an interface, or (4) spreading of surfactants from the solid phase directly onto a surface [26].

For surfactants to form micelles, the concentration of the surfactants must be above the critical micelle concentration (CMC), as depicted in Figure 5-2A. The micelle system depicted here is based on an oil-in-water (o/w) arrangement, as shown in Figure 5-2B. When the surfactant concentration is below the CMC, the amphiphobic tail moves away from the polar phase of the solvent, this generates surface tension forces without forming a micelle. It is important to determine the CMC for different species of surfactants since the formation of discrete micelle with controlled size is critical for the synthesis of NPs with controlled size and shape.

The reverse micelle system is an artificial construct that mimics biological systems involved in cell division and certain enzyme mechanisms. In Figure 5-2B, the schematic shows the structure of a bilayer cell membrane with a double tailed protein. In

the reverse micelle, the micro-emulsion system is in the form of water-in-oil (w/o) arrangement. The earliest report of micro-emulsions dates back to 1943 by Hoar and Schulman [27]. They documented the formation of a homogeneous “micro emulsions” solution by the combination of water, oil (long-chain hydrocarbons), surfactant (cetyltrimethylammonium bromide, CTAB), and a co-surfactant (alcohol). CTAB is a cationic surfactant exhibiting an amphiphilic nature with a long hydrocarbon chain. Water-oil-CTAB-alcohol microemulsion system is still widely used [28].

Anionic surfactants constitute the largest group of surfactants that are commercially available; these are the most frequently used surfactants in the drug delivery field. By varying the concentration, the shape of the sac-like structure formed can be changed to rod-shaped [29], spherical [30], cylindrical, hexagonal, or lamellar [26] structures as illustrated in Figure 5-2C.

The double tailed anionic surfactant, aerosol OT or AOT, which is the main capping agent used in our research to control the nanoparticle size, is shown in Figure 5-2D. The reason for selecting this specific anionic surfactant is its structure and the micelles it forms mimic the membranes of living cells. This biocompatibility makes AOT a promising candidate for future applications in the medical field. Furthermore, the size of AOT (ca. 2 nm) is very small, and this structural aspect can be exploited to engineer close range interactions with certain bacteria. The top panel of Figure 5-3 depicts the protocol for obtaining desirable sizes of NPs using AOT reverse micelle microemulsion systems to encapsulate and confine particle sizes.

5.2.2 Core-Shell System

Core-shell structures are composed of a nanoparticle core that is uniformly and continuously surrounded by an inorganic or organic shell. The core-shell system provides additional flexibility in tuning the properties of NPs.

In our research, CdS is confined within the core of a core-shell structure. There are many advantages to coating CdS with a different material. The luminescence properties of CdS can be enhanced by coating it with ZnS [31]. The band gap (E_g) of bulk CdS and ZnS are calculated to be 2.5 and 3.6 eV, respectively [32]. The small band gap material CdS can be coated with varying thicknesses of ZnS, which has a larger band gap; the luminescence properties of the composite structure can be finely tuned by adjusting the core and shell dimensions. There are also many research groups attempting to synthesize magnetic particles with good photoluminescence properties for biosensor development. By coating magnetic particles (core) with luminescent QDs (shell), it may be possible to obtain magnetic/luminescent core/shell biosensors [33].

The core/shell structures also facilitate the interaction of particles with other compounds. For biomedical applications, the surfaces of the NPs need to be appropriately modified. In a recent report by Liu et al. [34], CdSe/CdS core/shell structure are fabricated and functionalized with dendrons; carboxylic acid groups on the dendrons replaced the amine ligands on the surface of the shell. Iron NPs coated with gold will protect the Fe core from oxidization, and also prevent the aggregation of iron NPs [28]. Core/shell structures are manipulated in our research to enhance the solubility and ensure their covalent bonding with single-walled carbon nanotubes, as discussed in the final chapter.

5.2.3 Sol-Gel System

The sol-gel process is a liquid phase synthesis method for producing inorganic NPs. In the Cushing et al. [35] review, the first report of the sol-gel process date back to 1846 by Ebelmen; however, only in the 1930s was this process used for the synthesis of commercial products. The sol-gel process consists of a series of steps [35, 36]. The first step of the sol-gel process involves the formation of the sol by hydrolysis (M-OR + H_2O $\rightarrow$ M-OH + H-OR) and condensation. In water, the condensation reaction can be expressed as M-OH + HO-M $\rightarrow$ M-O-M + H_2O. In alcohol, the condensation reaction can be expressed as M-OR + HO-M $\rightarrow$ M-O-M + R-OH. The hydroxide species (M-OH) continue to yield oxide species (M-O-M) through condensation, and the oxide species link together to form a three-dimensional network. The second step of the sol-gel process is the formation of the gel when the three-dimensional network of the linked oxide (M-O-M) materials obtained from the sol solution extends across to the edge of the container. This kind of a gel can be called an alcogel (wet gel). To stabilize and strengthen the gel network, it is necessary to age the alcogel. Hydrolysis and condensation are allowed to proceed for several more cycles. The gel can be aged by covering the container at room temperature for at least 7 days. Without aging, it is difficult to process the gel without crush it. The third step of the sol-gel process is drying of the alcogel, which comprises the solid oxide network and the liquid solvent. The dried alcogel is called a xerogel when it is dried by evaporation or an aerogel when it is dried by extraction. The fourth step of the sol-gel process is dehydration, which is accomplished by calcining the gel at high temperature ($T \leq 800$ °C) to avoid rehydration of the gel. For ceramics or glass materials,

an additional densification and decomposition step needs to be performed at a temperature, T > 800 °C.

The sol-gel system provides an easy way for preparing NPs. In our group, the sol-gel system is used for the formation of Fe_2O_3 particles [37]. The details will be described in the following section.

5.3 Experiments

The experiments are described and classified according to the different growth mechanisms.

5.3.1 Reverse Micelle encapsulated QDs – CdS

Preparation of CdS: CdS, NPs were prepared in w/o (water-in-oil) reverse micelles using an *n*-heptane/AOT/water microemulsion system. Two identical reverse micelle solutions were prepared separately from a solution of 0.2 M sodium bis(2-ethylhexyl)sulfosuccinate (Aerosol OT or AOT; purchased from Fisher Scientific Co.) in n-heptane. One part of the reverse micelle solution was mixed with a 0.3 M aqueous solution of cadmium acetate, $Cd(CH_3COO)_2 \cdot 2H_2O$, to form a Cd/AOT microemulsion. The other part of the reverse micelle solution was mixed with a 0.3 M aqueous solution of sodium sulfide, $Na_2S \cdot 9H_2$, to form a S/AOT microemulsion. The Cd/AOT microemulsion was added to the S/AOT micro-emulsion with vigorous stirring for 1h. Final ratio of $[Cd^{2+}]/[S^{2-}]$ was 1. The various reverse micelle molar ratios, W_o = $[H_2O]/[AOT]$, were set as 2, 3, 4, 5, and 10.

Preparation of Cd^{2+} rich surface (CdSCd): The surface of CdS was enriched with positive charges using a W_o = 4 reverse micelle. The micro-emulsion system of Cd/AOT was added to the micro-emulsion system of S/AOT maintaining a 1:1 molar ratio of Cd^{2+} and S^{2-} with s vigorous stirring for 1h. Transparent light yellow CdS particles were obtained at the end of the process. Additional Cd/AOT microemulsions were then added to the CdS solution, and stirred for 1h. This resulted in a Cd^{2+}-rich

surface for the CdS NPs. The final molar ratio of $[Cd^{2+}]/[S^{2-}]$ was 1.5, and denoted as CdSCd.

Surface modification with Thiols (-SH): Four different CdS/thiol surface modification agents were used to stabilize the CdSCd surface with different functional groups. The stabilizing agents were sodium 3-mercapto-1-propanesulfonate (MPS, $HSCH_2CH_2CH_2SO_3Na$), 2-aminoethanethiol hydrochloride (AET, $HSCH_2CH_2NH_2 \bullet HCl$), 11-mercaptoundecanoic acid (MUA, $HS(CH_2)_{10}COOH$), and 3-mercaptopropyltrimethoxysilane (MPTS, $SH\text{-}(CH_2)_3\text{-}Si\text{-}(OCH_3)_3$). 100 μL of a 0.3 M solution of each stabilizing agent was added separately to 12 mL aliquots of the CdSCd/AOT solutions and stirred overnight to form CdSCd-SH samples. The solutions were dried under vacuum at 50°C to remove excess solvent. Methanol was added to destroy the AOT reverse micelle structures. Precipitates were obtained after allowing the mixture to stand at room temperature for one day. The supernatant was then decanted. Centrifugation was performed to remove extra micellar structures in the solution by washing several times with methanol. The supernatants were discarded, and the extra solvent left over in the precipitates was removed by drying in vacuum at 50 °C for one day.

5.3.2 Reverse Micelle encapsulated QDs –ZnS

An analogous method of CdS was used to prepare ZnS NPs. Three stock solutions were prepared: 0.2 M AOT in n-heptane, 0.3 M $Na_2S \bullet 9H_2O$ in H_2O, and 0.3M $Zn(CH_3COO)_2$ in H_2O. The reverse micelle molar ratio, $W_o = [H_2O]/[AOT]$, was 4.

5.3.3 Core-Shell NPs – Fe@Au

To prepare gold-coated magnetic NPs, four stock solutions were used. Micelle solutions were prepared using 0.2 M AOT in n-heptane. Three separate aqueous solutions were prepared containing 0.4 M $FeSO_4 \bullet 7H_2O$, 0.4 M $HAuCl_4 \bullet xH_2O$, and 0.4 M $NaBH_4$. Three microemulsion solutions were prepared by adding each individual aqueous solution into the micelle solution with a molar ratio (W_o) of 5. Microemulsion systems containing $FeSO_4$/AOT, $NaBH_4$/AOT, and $HAuCl_4$/AOT are denoted as Msys1, Msys2, and Msys3, respectively. The iron core particles were obtained by mixing Msys1 with Msys2 with a molar ratio of [Fe]/[B]=1:2 under continuous magnetic stirring for 2 h. The gold shells were formed by mixing Msys3 with Msys2 with a molar ratio of [Au]/[B]=1:3 under continuous magnetic stirring for 2 h. The gold solution was added to the iron solution with a molar ratio of [Au]:[Fe] = 2:3 with constant stirring overnight.

5.3.4 Sol-Gel NPs – Fe_2O_3

Fe_2O_3-silica nanocomposite particles containing different amounts of Fe_2O_3 were formed by sol-gel co-precipitation synthesis. The silica source was tetraethoxysilane (TEOS, $Si(OC_2H_5)_4$, Alfa). Pre-stock solutions were prepared by dispersing 0.15, 0.33, 0.9, and 2.0 g of $Fe(NO_3)_3 \bullet 9H_2O$ in 25 mL of ethanol . After vigorous stirring for an hour, 1 mL of TEOS was added slowly into the prepared solutions and stirred continuously for another hour. The proportion of Fe_2O_3/(Fe_2O_3 + SiO_2) in the final sol-gel stock solution is 8.2, 16.4, 33.2, and 52.8 wt.%, respectively, for solutions prepared using 0.15, 0.33, 0.9, and 2.0 g of $Fe(NO_3)_3$. To catalyze the formation of the sols solution, a small amount

of HNO_3 was added into each beaker. Aerogel was formed by heating the four stock solutions at 80 °C on a hotplate to evaporate the solvent. The resultant dark brown solid pallets were washed and heated at 180 °C in air to achieve the complete dehydration of the final product.

5.4 Results and Discussions

The CdS QDs were encapsulated in reverse micelles of AOT in n-heptane solution. Figure 5-3 shows the UV-Vis absorption spectra of a series of CdS NPs with different sizes. The UV-Vis absorption spectra of all the QDs are blue-shifted from that of the bulk form of CdS (ca. 510 nm, E_g 2.5 eV). The molar ratio of $[H_2O]/[AOT]$ can be used to estimate the approximate size of CdS, d (nm) = 0.36 W_0 [38]. The larger the molar ratio, the larger the size of the QDs. In general, size of the QDs follows (W_0=10) > (W_0=5) >… > (W_0=2). From the UV-Vis spectra, the onset of the absorption wavelength can be calculated by the Brus equation (1). Different molar ratios for obtaining different sizes of CdS are labeled in Figure 5-3. Notably, it is possible to tune the color of the QDs by varying the particle size which permits great flexibility for applications in medical diagnostics. For example, the smallest CdS NPs are obtained fro W_0=2, but these NPs are either transparent and/or colorless. Thus, larger NPs, synthesized at higher $[H_2O]/[AOT]$ ratios are used for applications such as biosensoring.

In Figure 5-4, the same molar ratio (W_0 = 4) is used to encapsulate different QDs. It illustrates that the ZnS have a larger band gap ($E_{g,ZnS}$, 3.6 eV) with a smaller diameter (1.70 nm), and the CdS have a smaller band gap ($E_{g,CdS}$, 2.5 eV) with a larger diameter (2.04 nm). A coating of wider band gap ZnS enhances the luminescence properties of the CdS QDs and thus core-shell structures composed of a CdS core and ZnS shell have been fabricated [39].

In order to interact with SWNTs, the surfaces of the CdS QDs have to be modified. To functionalize the CdS QDs in reverse micelles, a surface enhancement reaction was performed. As shown in Figure 5-5, the ratio of [Cd]/[S] was around 1.4 to

ensure the excess of positive charge Cd^{2+} on the surface of the QDs in the reverse micelles. Different thiol containing stabilizing agents were exchanged for the anionic surfactant AOT to passivate the CdS surfaces. Upon surface modification, the only QDs that exhibited a red shift, indicating an increase in the shell thickness, was the one modified by MPTS [40]. In the Fe/Au core-shell process, no usable data were obtained in our experiments.

In the Fe_2O_3/SiO_2 nanocomposite sol-gel system, X-ray diffraction (XRD) can be used to determine the amount of iron oxide trapped within the silica matrix, as shown in Figure 5-6A. For samples a and b (8.6 and 16.4 wt% of iron), the broad peak at around 20° corresponds to the amorphous SiO_2 matrices, whereas peaks from iron particles was absent. For samples c and d, there are two diffraction peaks ($2\theta \approx 33.1°$ and 35.6°) which are associated with α-Fe_2O_3 (i.e. hematite). Figure 5-6B shows the Raman spectrum of the 52.8 wt.% sample. Well-defined bands are observed at approximately 222, 287, 401, and 601 cm^{-1} have indicating the formation of α- Fe_2O_3 particles (antiferromagnetic). FTIR spectra have also been obtained. The peaks in the FTIR spectra shown in Figure 5-7 can be attributed to vibrations of Si-OH and Si-O-Si groups. The asymmetric and symmetric stretching modes of the Si-O-Si bands are seen at ca.1200 and 800 cm^{-1}, respectively. Although a Fe-O mode is observed at about 570 cm^{-1}, the FTIR spectra do not clearly indicate the interaction between Fe_2O_3 and the SiO_2 matrix [37].

5.5 Conclusion

The reverse micelle water-in-oil microemulsion process can be used to define the sizes of NPs. The QD solutions are homogeneous and can be stored for long periods of time with very little change in the absorption bands. The approach thus represents a facile technique for obtaining CdS nanoparticles. Many groups have begun to investigate the potential applications of QDs in medical devices, but toxicity to biological systems remains the first consideration. In recent year, there have been many reports on the toxicity of NPs. For example, titanium dioxide/ zinc oxide NPs used in sunscreens, can act as antioxidants but are also a source of free radicals in the skin, and can cause damage to DNA. The safety issues must be carefully evaluated before commercializing NPs. Careful control of the structure and surface chemistry of NPs will pave the way for their use in practical applications.

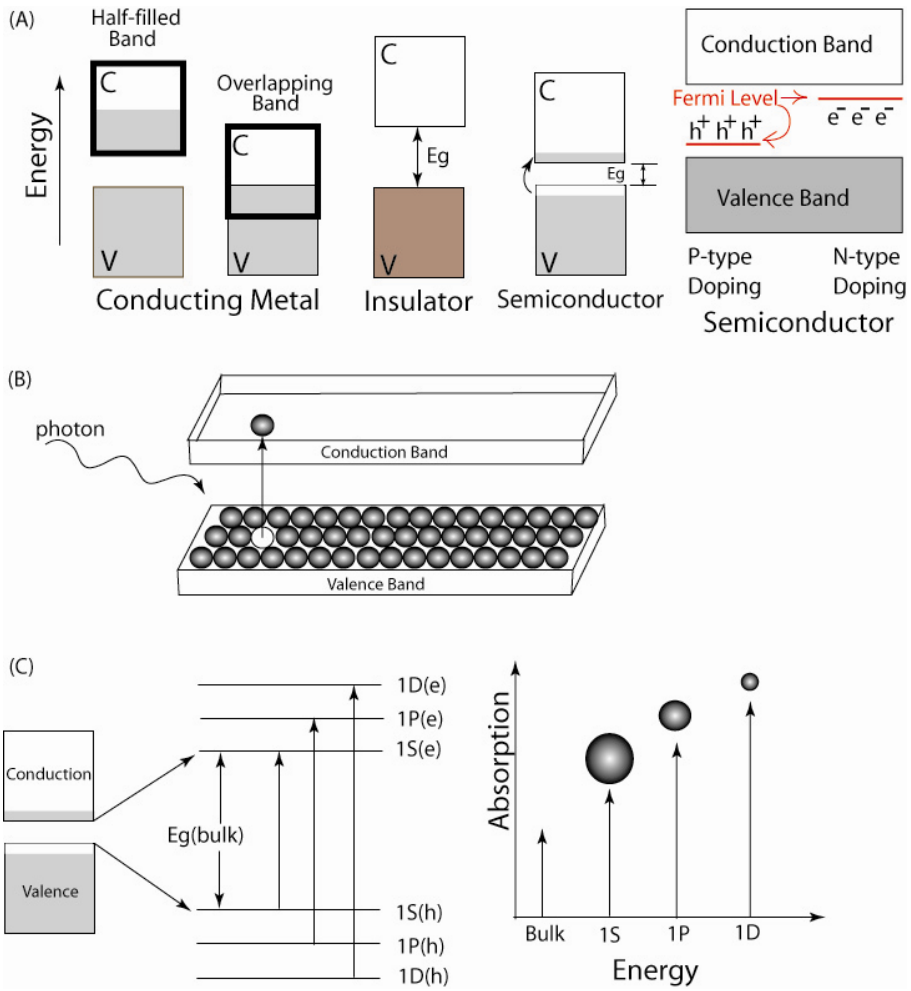

Figure 5-1 Schematic depiction of band gaps. (A) Electronic properties of metals, insulators, semiconductors, and p-type and n-type doped semiconductors. (B) An electron-hole pair. (C) Energy relationship for different sizes of QDs.

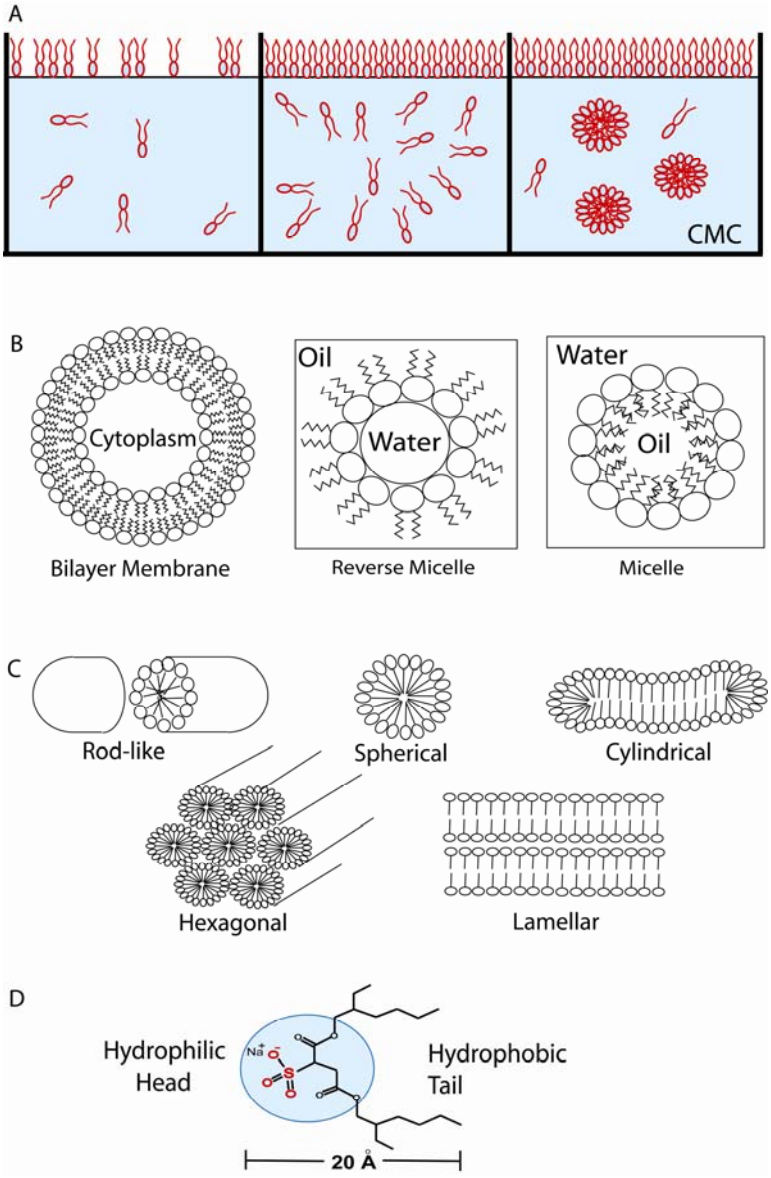

Figure 5-2 Formation and structures of surfactants. (A) Colloidal system formed when the micelle concentration is below (left) and above (right) the critical micelle concentration. (B) Reverse micelles and micelles mimic the structures of bilayer membranes in living cells. (C) Different CMC produce different micelles with different structures [26]. (D) The structure of anionic surfactant aerosol OT (AOT).

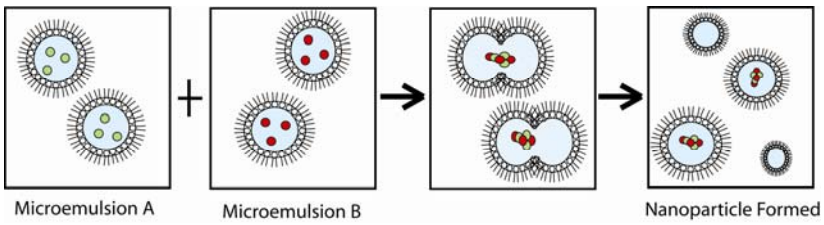

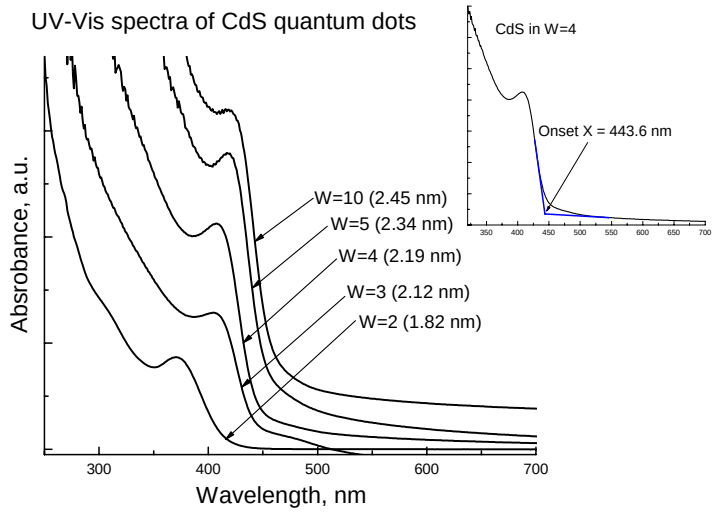

Figure 5-3 The formation of CdS in reverse micelle microemulsions (Top). Absorption spectra of different sizes of CdS NPs (Bottom).

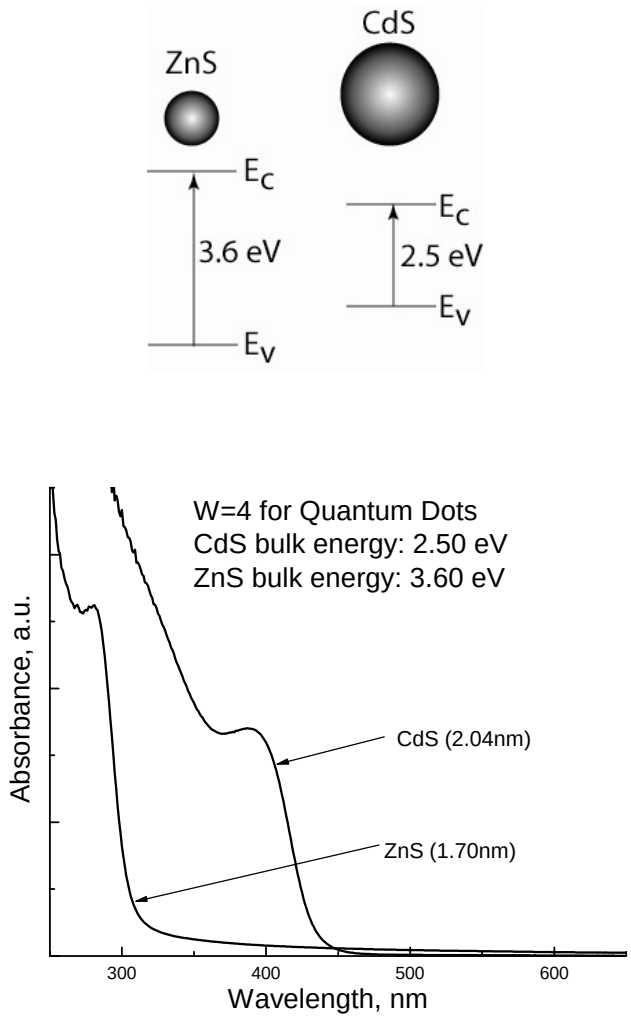

Figure 5-4 Comparison of CdS and ZnS NPs prepared using the same molar ratio ($W_o = [H_2O]/[AOT]$) of 4.

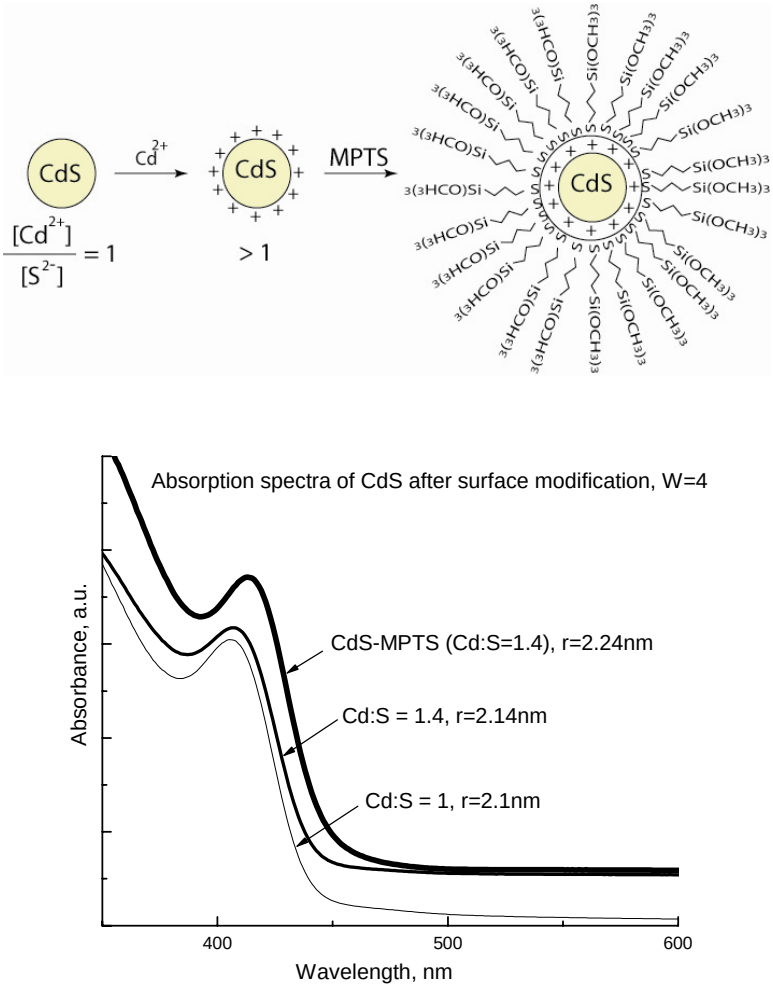

Figure 5-5 Absorption spectra of CdS, CdSCd, and MPTS-modified CdSCd.

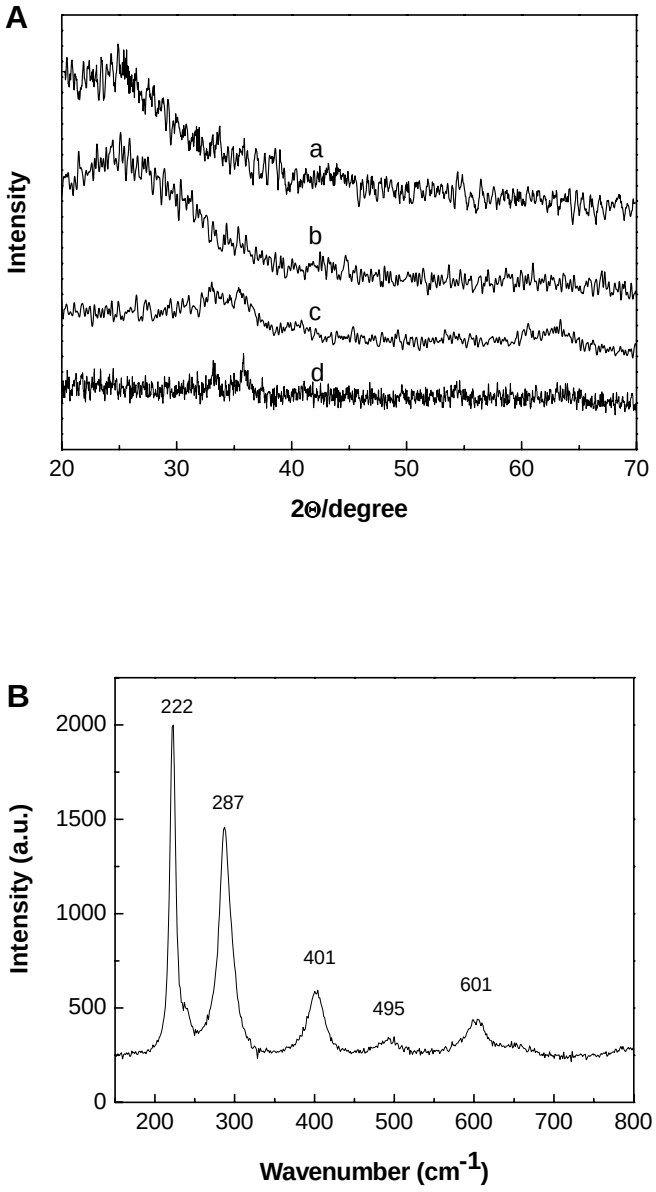

Figure 5-6 X-ray diffraction pattern (A) of Fe_2O_3/SiO_2 nanocomposites dispersed within SiO_2 matrix contained different weight percents of Fe_2O_3 (a) 8.6 wt%, (b) 16.4 wt%, (c) 33.2 wt%, and (d) 52.8 wt%. In addition, 52.8 wt% of Raman spectrum is displayed (B).

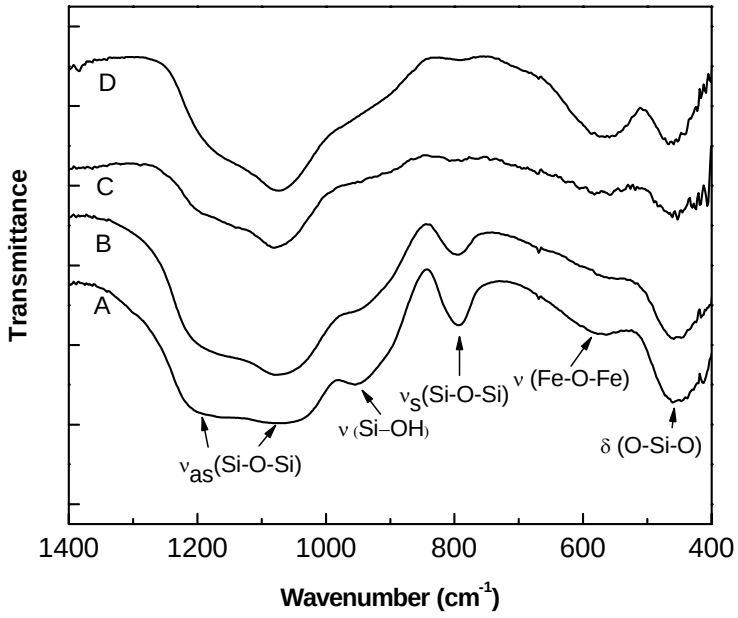

Figure 5-7 FTIR spectra of Fe_2O_3/SiO_2 nanocomposites within SiO_2 matrix containing different amounts of Fe_2O_3 (A) 8.6 wt%, (B) 16.4 wt%, (C) 33.2 wt%, and (D) 52.8 wt%.

References

[1] D. Qi, M. Fischbein, M. Drndić, S. Šelmić, Efficient Polymer-Nanocrystal Quantum-Dot Photodetectors, Appl. Phys. Lett., 86, 093103 (2005).

[2] H.S. Zhou, I. Honma, J.W. Haus, H. Sasabe, H. Komiyama, Synthesis and Optical Properties of Coated Nanoparticle Composites, J. Lumin., 70, 21 (1996).

[3] S.K. Sahoo, T.K. De, P.K. Ghosh, A. Maitra, pH- and Thermo-Sensitive Hydrogel Nanoparticles, J. Colloid interface Sci., 206, 361 (1998).

[4] P. Ball, Designing the Molecular world, Princeton University Press, p192-193 (1994).

[5] hyperphysics.phy-astr.gsu.edu/hbase/solids/fermi.html#c1.

[6] J.D. Holmes, P.A. Bhargava, B.A. Korgel, K.P. Johnston, Synthesis of Cadmium Sulfide Q Particles in Water-in-CO2 Microemulsions, Langmuir, 15, 6613 (1999).

[7] T.K. Bergstresser, M.L. Cohen, Electronic Structure and Optical Properties of Hexagonal CdSe, CdS, and ZnS, Phys. Rev., 164, 1069 (1967).

[8] V.I. Klimov, Nanocrystal Quantum Dots: from Fundamental Photophysics to Multicolor Lasing, Los Alamos Science, 28, 214 (2003).

[9] L.E. Brus, Electron-Electron and Electron-Hole Interactions in Small Semiconductor Crystallites: The Size Dependence of the Lowest Excited Electronic State, J. Chem. Phys., 80, 4403 (1984).

[10] L. Brus, Chemical Approaches to Semiconductor Nanocrystals, J. Phys. Chem. Solids, l59, 459 (1998).

[11] W. Xu, Y. Liao, D.L. Akins, Formation of CdS Nanoparticles within Modified MCM-41 and SBA-15, J. Phys. Chem. B, 106, 11127 (2002).

[12] T. Torimoto, N. Tsumura, M. Miyake, M. Nishizawa, T. Sakata, H. Mori, H. Yoneyama, Preparation and Photoelectrochemical Properties of Two-Dimensionally Organized CdS Nanoparticle Thin Films, Langmuir, 15, 1853 (1999).

[13] S.S. Shankar, S. Chatterjee, M. Sastry, Synthesis of CdS Nanoparticles within Thermally Evaporated Aerosol OT Thin Films, PhysChemComm, 6(9), 36 (2003).

[14] W. Xu, D.L. Akins, Reverse Micellar Synthesis of CdS Nanoparticles and Self-Assembly into a Superlattice, Mat. Lett., 58, 2623 (2004).

[15] D. Zhang, L. Qi, J. Ma, H. Cheng, Formation of Crystalline Nanosized Titania in Reverse Micelles at Room Temperature, J. Mater. Chem., 12, 3677 (2002).

[16] I.H. El-Sayed, X. Huang, M.A. El-Sayed, Surface Plasmon Resonance Scattering and Absorption of Anti-EGFR Antibody Conjugated Gold Nanoparticles in Cancer Diagnostics: Applications In Oral Cancer, Nano Lett., 5(5), 829 (2005).

[17] F. Xie, M.S. Baker, E.M. Goldys, Homogeneous Silver-Coated Nanoparticle Substrates for Enhanced Fluorescence Detection, J. Phys. Chem. B, 110, 23085 (2006).

[18] K. O'Grady, Biomedical Applications of Magnetic Nanoparticles, J. Phys. D: Appl. Phys., Editorial, 36 (2003).

[19] P. Tartaj, M. del Puerto Morales, S. Veintemillas-Verdaguer, T. González-Carreño, C. J Serna, The Preparation of Magnetic Nanoparticles for Applications in Biomedicine, J. Phys. D: Appl. Phys., 36, R182 (2003).

[20] C.C. Berry, A.S.G. Curtis, Functionalisation of Magnetic Nanoparticles for Applications in Biomedicine, J. Phys. D: Appl. Phys., 36, R198 (2003).

[21] Q.A. Pankhurst, J. Connolly, S.K. Jones, J. Dobson, Applications of Magnetic Nanoparticles in Biomedicine, J. Phys. D: Appl. Phys., 36, R167 (2003).

[22] D. Caruntu, B.L. Cushing, G. Caruntu, C.J. O'Connor, Attachment of Gold Nanograins onto Colloidal Magnetite Nanocrystals, Chem. Mater., 17, 3398 (2005).

[23] S.-J. Cho, J.-C. Idrobo, J. Olamit, K. Liu, N.D. Browning, S.M. Kauzlarich, Growth Mechanisms and Oxidation Resistance of Gold-Coated Iron Nanoparticles, Chem. Mater., 17, 3181 (2005).

[24] M.L. Steigerwald, A.P. Alivisatos, J.M. Gibson, T.D. Harris, R. Kortan, A.J. Muller, A.M. Thayer, T.M. Duncan, D.C. Douglass, L.E. Brus, Surface Derivatization and Isolation of Eemiconductor Cluster Molecules, J. Am. Chem. Soc., 110, 3046 (1988).

[25] M. Ozkan, Quantum Dots and Other Nanoparticles: What Can They Offer to Drug Discovery?, Drug Discovery Today, 9, 1065 (2004).

[26] Y. Moroi, Micelles: Theoretical and Applied Aspects, Plenum Press, New York (1992).

[27] T.P. Hoar, J.H. Schulman, Nature, 152, 102 (1943).

[28] S.-J. Cho, B.R. Jarrett, A.Y. Louie, S.M. Kauzlarich, Gold-Coated Iron Nanoparticles: A Novel Magnetic Resonance Agent for T1 and T2 Weighted Imaging, Nanotechnology, 17, 640 (2006).

[29] S. Ikeda, S. Hayashl, T. Imae, Rodlike Micelles of Sodium Dodecyl Sulfate in Concentrated Sodium Halide Solutions, J. Phys. Chem., 85, 106 (1981).

[30] W.L. Courchene, Micellar Properties from Hydrodynamic Data, J. Phys. Chem., 68, 1870 (1964).

[31] A.R. Loukanova, C.D. Dushkina, K.I. Papazovaa, A.V. Kirova, M.V. Abrashevb, E. Adachi, Photoluminescence Depending On the ZnS Shell Thickness of CdS/ZnS Core-Shell Semiconductor Nanoparticles, Colloids Surf. A, 245, 9 (2004).

[32] P.E. Lippens, M. Lannoo, Calculation of the Band Gap for Small Cds and Zns Crystallites, Phys. Rev. B, 39, 39 (1989).

[33] D. Wang, J. He, N. Rosenzweig, Z. Rosenzweig, Superparamagnetic Fe2O3 Beads-CdSe/ZnS Quantum Dots Core-Shell Nanocomposite Particles for Cell Separation, Nano Lett., 4, 409 (2004).

[34] Y. Liu, M. Kim, Y. Wang, Y.A. Wang, X. Peng, Highly Luminescent, Stable, and Water-Soluble CdSe/CdS Core-Shell Dendron Nanocrystals with Carboxylate Anchoring Groups, Langmuir 22, 6341 (2006).

[35] B.L. Cushing, V.L. Kolesnichenko, C.J. O'Connor, Recent Advances in the Liquid-Phase Syntheses of Inorganic Nanoparticles, Chem. Rev., 104, 3893 (2004).

[36] http://eetd.lbl.gov/ECS/aerogels/saprep.htm, How Silica Aerogels Are Made.

[37] X. Zhang, H. Guo, N. Chi, S.C. Wang, N.-L. Yang, D.L. Akins, Self-Aligned Magnetic Dipole Moments of Fe2O3 Formed within Sol–Gel Matrix, Mat. Chem. Phys., 98, 207 (2006).

[38] E. Caponetti, L. Pedone, D. Chillura Martino, V. Pantò , V.T. Liveri, Synthesis, Size Control, and Passivation of CdS Nanoparticles in Water/AOT/n-Heptane Microemulsions, Mat. Sci. Eng. C, 23, 531 (2003).

[39] J.S. Steckel, J.P. Zimmer, S. Coe-Sullivan, N.E. Stott, V. Bulović, M.G. Bawendi, Blue Luminescence from (CdS)ZnS Core–Shell Nanocrystals, Angew. Chem. Int. Ed., 43, 2154 (2004).

[40] K. Iwasaki, T. Torimoto, T. Shibayama, H. Takahashi, B. Ohtani, Preparation and Characterization of Water-Soluble Jingle-Bell-Shaped Silica-Coated Cadmium Sulfide Nanoparticles, J. Phys. Chem. B, 108, 11946 (2004).

6

Nanocomposites of Single-Walled Carbon Nanotubes

Single-walled carbon nanotubes (SWNTs) have many potential applications arising from their unique electronic, mechanical, chemical, and thermal properties. Nanocomposites of SWNTs may have potential applications in many different areas. In this chapter, we discuss several proposed applications of carbon nanotubes. SWNT nanocomposites are still in the early stage of development. These novel materials are expected to be final applications in the next generation of electronic devices and biomedical assays.

6.1 Introduction

The discovery of new materials with enhanced functionalities is a key for the advancement of technology. SWNTs are a remarkable new form of carbon discovered a few decades ago. The extraordinary electronic, optical, and mechanical properties of SWNTs described in Chapters 1 and 2, make them very attractive for incorporation in nanocomposites. The unique properties of carbon nanotubes may lead to applications in optoelectronic and biomedical devices.

As-grown SWNTs are aggregated together in bundles or ropes due to strong tube-tube van der Waals interactions that hinder the dissolution of the tubes. One major challenge in this area has been the solubilization and debundling of nanotubes which was unequivocally resolved only in 2005. It is now possible to dissolve and individualize bundled SWNTs. Isolated individual SWNTs have the potential to be used for the development of biochips, field-emission transistors (FET), batteries, etc.

Another major challenge is the incorporation of SWNTs in nanocomposites. SWNTs nanocomposites can be classified according to their potential applications, such as in fuel cells, field emission, microscopy probes, biosensors, etc. The following sections outline various kinds of SWNT composites.

6.1.1 SWNT/Polymers Nanocomposite

The properties of polymers can be enhanced by incorporating SWNTs to form polymer/SWNT nanocomposites [1]. Purified nanotubes can either be directly mixed with polymeric materials or can be chemically modified by polymers [2]. Polymers can

either be covalently attached to functionalized nanotubes [3] or non-covalently wrapped around nanotubes [4].

The unique properties of SWNTs lead to enhanced properties for nanocomposites. One example is the case with which the percolation threshold is reached in nanocomposites [5]. Percolation is defined as the behavior of the movement or filtering of liquid/gas species through porous materials. When the composites reach a critical threshold for percolation, the electrical and/or thermal conductivities of the materials are significantly improved. Epoxy is one of the polymers that have been used to form composites with SWNTs for lowering the critical percolation threshold. SWNT nanocomposites can also be used to coat biological cellular parts and as coatings for military planes taking advantage of the electronic properties of SWNTs to improve percolation of polymers. The mechanical strength and the light weight of the SWNTs make the SWNT composites promising for applications in transportation, bulletproof vests, space suits, etc. Mylvaganam and Zhang [6] have listed many useful applications of nanotube composites based on a variety of polymers. SWNTs are incorporated into nanocomposites with different polymers equipped with different functionalities. For example, SWNTs can interact with both polyethylene (PE) and poly (4-methyl-1-pentene) or PMP. However, the SWNT/PMP composite exhibits better mechanical, thermal, and optical properties as compared to the SWNT/PE composites, making it appropriate for space vehicles and space shelters. Another composite, of SWNTs and poly(dimethylsiloxane), has been shown to be useful for applications in actuators (mechanical movement) and chemical sensors (e.g. CO detection). There is still much

room for improving the properties of nanocomposites, and there is much that needs to be done to understand the properties of these systems.

6.1.2 SWNT/Biomolecular species Nanocomposite

Biological species are another material used to functionalize SWNTs. Since the unique properties of SWNTs have attracted much attention for biomedical applications, one of the issues being investigated is the interaction between SWNTs and living cells. Carbon nanotubes are usually used as a scaffold or backbone to attach with biomaterials as described below.

Deng et al. [7] have reported the covalent attachment of chitosan to CNTs. Chitosan is a polysaccharide that is extracted and modified from chitin in the shells of shellfish. It is an abundant natural polymer, and is also a fat inhibitor. The development of CNT/Chitosan nanocomposites has also attracted much industrial interests such as for weight loss supplements and cosmetic products. Glucosamine is another supplement that is produced from chitin, and has been prepared in vitro to interact with SWNTs for the study of biocompatibility in living systems [8].

In the tissue engineering field, research groups are looking for new seeding materials to reconstruct damaged cells. The attachment of living tissues (e.g. collagen) [9] to acid purified SWNTs will give rise to SWNT/biomaterial composites which may be able to repair, enhance the strength, and add better flexibility to tissues.

The incorporation of SWNTs into polymer matrices leads to improve mechanical properties; the SWNTs essentially act as reinforcing filters. To ascertain the degree of dispersion of the tubes, single tube fluorescence in the matrix needs to be studied.

Aggregated SWNTs and metallic tubes do not fluoresce due to energy transfer to adjacent tubes with lower band gap energy. Proteins (concanavalin-A) have been used to disperse SWNTs to achieve the goal of preventing, quenching, and energy transfer [10]. Concanavalin-A (con-A) is a lectin protein which plays an important role in the human immune system. Con-A is extracted from jackbean or Chickasaw lima bean. Individual SWNT has been successfully isolated from dispersed bundles of SWNTs using con-A. SWNT/con-A composites may be useful for enhancing the immune system as a daily dietary supplement.

Peptides are another biomolecular species often used to interact with carbon nanotubes [11]. Poly-L-lysine (PLL, a polymeric peptide) is often used for the biological coating of slides, and PLL can stabilize the SWNTs/peptide for further observation [12].

6.1.3 SWNT/Nanoparticles Nanocomposite

Nanoparticles (NPs) have been used to interact with SWNTs due to their quantum size effect. Different sizes of NPs exhibit different color and electronic properties as mentioned in Chapter 5. Recently, there has been a report of a nanocomposite composed of NPs and carbon nanotubes exhibiting flame retarding properties [13].

In recent year, there has been a lot of progress in developing materials for the solubilization and functionalization of SWNTs. One interesting approach to manipulate SWNTs and change their electronic properties as desired is to functionalize them with semiconducting NPs [14]. The formation of SWNT/NP composites holds promise for the development of optoelectronic devices, field emitters, and memory storage media.

There have been many attempts to find suitable protocols to make SWNT/NP nanocomposites, and it has been met with some success. SWNTs have be covalently attached to rare earth oxide [15], CdTe [16], CdSe [17], and Ti [18] nanoparticles. The resulting materials are characterized by SEM, HR-TEM, and Raman spectroscopy. Composites of SWNTs with CdS quantum dots show increased individualization of SWNTs [19]. Fluorescent QDs can be used to label the SWNTs [20]. Composites of SWNT/QDs with fluorescent properties can pave the way for implantable biosensors in the future [21].

6.2 Potential Applications of SWNTs Nanocomposites

In the previous sections we detail the functionalization of SWNTs with polymers, biomolecules, and NPs composites. Here, we focus on specific applications where SWNTs may be useful.

6.2.1 Fuel Cell

A fuel cell (FC) is an electrochemical energy conversion device that coverts the chemical energy of a fuel (e.g., hydrogen, which is oxidized) and oxidant (e.g., oxygen, which is reduced) into electricity as shown in Figure 6-1. FCs are being developed as alternatives to traditional batteries. Traditional batteries die when the chemicals inside the compartment are consumed. In contract, FCs are based on a design that will allow a continuous source of energy. In the report by Budevski [22], SWNTs have been used as catalyst carriers and gas transport channels. The small diameter of SWNTs allows only hydrogen gas (an oxidation fuel source in Budevski report) to penetrate inside the tubes, and this phenomenon may lead to improvement in gas production and gas consumption. Carbon nanotubes can also reduce the amount of catalysts needed in proton exchange membrane fuel cells (PEMFC) [23]. The long length of the tubes minimizes the catalyst loading amount required and improves the utilization efficiency of the catalyst, and the long tubes also ensure the delivery of electronic pathway to the destination electrode. In commercialized PEMFC, metal Pt is used as a catalyst which is expensive. Nanocomposites of carbon nanotubes, Nafion, and a metallic catalyst (M) have been

produced experimentally, and the CNT/Nafion/M composite boosts the efficiency of the PEMFC with a reduction in cost by reducing the amount of metallic catalyst needed. The challenge is that one single fuel cell can only carry 0.7 V. A stack of fuel cells may be required to increase the amount of available power, but the problem of electron leakage between the contacting surfaces of each fuel cell has to be addressed. In the effort of developing PEMFC technology, NEC corporation has reported the first laptop using nanohorns (one end of the nanotube is sealed and the other end is opened) based fuel cell as the power supply at WPC EXPO in September 2003, as displayed in Figure 6-1.

6.2.2 Electronics – Field-Effect Transistor

There have been many reports about the potential applications of SWNTs in electronic. More specifically, these materials will be useful for applications in nanoelectronics devices. To integrate SWNTs into nanoelectronics, their electronic transport properties have been studied in field-effect transistor (FET) geometries.

FETs have components of source, drain, gate, and substrate, as illustrated in Figure 6-1. FET conduction is controlled by the electric field produced by the voltage applied to the gate electrode. Depending on the charge carrier, the FETs can be n-channel (conduction by electrons) and p-channel (conduction by holes) [24]. There are various types of FET. For example, the JFET is a form of a semiconductor junction. Another type of FET is called metal oxide semiconductor FET (MOSFET) which has an insulating gate. SWNTs have distinctive electronic (semiconducting or metallic) properties as discussed in Chapter 1, are good candidates as active channels in semiconducting devices. The structure of a back-gate FET is shown in Figure 6-1. The gate SiO_2 is usually used as

dielectric. Section 4.4.2 describes the dielectrophoretic alignment of SWNTs in FET structures. The electrodes in these devices are made of 5 nm Cr and 50 nm Au. The application of using SWNT in FET is not only in searching for more efficient current flow and as an effective electron carrier, but SWNT/FET is also promising in the enhancement of sensor fields.

6.2.3 Sensors

SWNTs can be used as physical, chemical, and biological sensors. Ghosh et al. [25] have reported the use of SWNT devices as current and voltage sensors. The excellent mechanical properties of SWNTs make them useful as actuators [26].

Kong et al. [27] were the first to report the use of SWNT FETs to sense low concentrations of nitrogen dioxide (NO_2) and ammonia (NH_3) gas. The device comprises a single semiconducting SWNT connecting gold source/drain electrodes pattered on a Si/SO_2 substrate. The transport properties of the SWNT FETs have been studied in sealed chambers by introducing very low concentration of NO_2 and NH_3. The conductance of the SWNTs is significantly modified by the introduction of NO_2 and NH_3. The modified conductance likely originates from changes in the Schottky barriers at the contact between the SWNT and the electrodes. The barrier heights and the nanotube Fermi level at the contacts may be changed by the adsorption of gas molecules.

SWNTs FETs have also been used as biosensors. SWNT FET platforms based on non-covalent functionalized SWNTs have been used to detect different biomaterials [28]. SWNTs/FET is able to detect the interaction between antibodies and specific antigens. Raman spectroscopy has been used to differentiate the interaction of functionalized

SWNTs electrodes with different DNA sequences [29]. SWNTs can also be used as AFM probe tips to probe biological species without damaging the samples. SWNT sensors offer improved sensitivity and potential for miniaturization.

6.3 Experiments

The experiments were conducted using nanoparticles prepared as described in the previous chapter. Three different nanocomposites have been prepared.

6.3.1 SWNT-CdS

As-prepared quantum dots, CdS, synthesized using a molar ratio (W_o = $[H_2O]/[AOT]$) of 2, were mixed with AOT functionalized SWNTs. The SWNT dispersion was prepared using 1 mg SWNTs dissolved in 1 mL of 0.5 wt% AOT aqueous solution without further centrifugation. The SWNT/CdS composite is formed by dispersing CdS nanoparticles in a SWNT/AOT solution with SWNT/CdS ratio of 1, 3, 5, 7, and 10 (w/w). The final concentration of SWNTs was set at 0.1 mg/mL, and a final volume of 10 mL was used. After sonication for 2 hours, the solvent was dried in vacuum. 10 mL of distilled water was then added, and the dispersion sonicated again. The final products were stored in a refrigerator for further analysis.

6.3.2 SWNT-surface-modified-CdS

Nanocomposite of SWNT with silane modified CdS (SWNT/CdS-Si-OH). Cd^{2+} enriched fluorescent quantum dots, CdS, were prepared using the structure defining agent, AOT, in heptane and are denoted as CdSCd as described in Chapter 5. The microemulsion system of CdSCd was prepared using a molar ratio, W_o = 4. 200 mL of CdSCd was vacuum dried at a temperature of about 50 ±5°C to remove the AOT/heptane micelles. Toluene and 0.1 mL MPTS (3-mercaptopropyltrimethoxysilane, $SH-(CH_2)_3-Si-(OCH_3)_3$, were added to replace AOT on the surface of CdSCd. CdSCd-MTPS was

hydrolyzed by refluxing with H_2O. CdS-S---Si-OH was formed after vacuum drying, and redispersed in 10 mL ethanol. Nanocomposites of SWNT/CdS-S---Si-OH are formed by adding 1.6 mL CdS-S-Si-OH into 8 mL of 1 mg/mL SWNT/AOT. After sonicating for 1 h, the sample was vacuum dried. The resulting nanocomposite was redispersed into distilled water.

Nanocomposite of SWNTs with SH-COOH surface-modified CdS (SWNT/CdS-COOH). Cd^{2+} enriched fluorescent quantum dots were prepared as described above. MUA (11-mercaptoundecanoic acid, HS-$(CH_2)_{10}$-COOH) was dissolved in methanol to modify the CdSCd surface with a 20:0.1 ratio of CdS:MUA (v/v). The nanocomposite of SWNT/CdS-S-COOH was formed by adding 4 mL of CdS-S-COOH into 4 mL of 1 mg/mL of the SWNT/AOT dispersion. The mixture was vacuum dried after sonication for 1 h. The resultant nanocomposite was re-dispersed into distilled water.

Acid purified SWNTs (pSWNT) were also used to interact with surface-modified CdS.

6.3.3 SWNT-Poly-L-Lysine

Poly-L-lysine hydrobrominde (PLL•HBr, MW 14,400, CAS#25988-63-0) was prepared by dispersing 1 mg PLL•HBr into 10 mL DI water. Poly-L-lysine hydrobrominde is thereafter also referred as PLL. 9 mL of a 1 mg/mL aqueous solution of AOT-functionalized SWNTs was dried at 150 °C in an autoclave. 18 mL of heptane was added to eliminate AOT from the wrapped SWNTs, and the mixture was further sonicated for 10 minutes to completely remove AOT. The heptane phase was carefully removed by centrifugation and discarded. The precipitate was allowed to sit at room

temperature in the fume hood until it completely dried. 9 mL of 0.1 mg/mL PLL(aq) was added to dry SWNTs-AOT, and the mixture was stirred for 3 days using a magnetic stirrer. The formed SWNT/PLL precipitate was stored in a refrigerator.

The same procedure was also performed with purified SWNTs (pSWNTs) to form pSWNT/PLL nanocomposites, i.e., the as-received nanotubes were replaced by purified nanotubes. The procedure for purifying tubes is discussed in Chapter 4. Briefly, 18 mg of HiPco SWNTs were dispersed in 0.6 mL H_2SO_4 and 0.2 mL HNO_3 (3:1 v/v of H_2SO_4 to HNO_3), and sonicated for 1 hour. The acid purified SWNTs (pSWNT) were then centrifuged and washed with distilled water several times. The pSWNT sample was then dried at 150 °C in an autoclave. 1 mg/mL pSWNT/AOT was formed by adding 16.53 mL of the 0.2 wt.% AOT aqueous solution and sonicated for 3 h at room temperature. The procedure described above is then used to form the pSWNT/PLL nanocomposite.

6.4 Results and Discussion

We were unable to attach many of the NPs discussed in the previous sections to SWNTs. This section describes the SWNT nanocomposites that could be unequivocally characterized.

6.4.1 Nanocomposite of SWNTs Intercalation with QDs

Figure 6-2 shows preliminary results for the formation of SWNT/CdS nanocomposites. A 0.5 mg/mL solution of SWNTs was obtained by dispersing the SWNT in DI H_2O using AOT(aq) without any centrifugation. A better dispersion was obtained when the SWNT to CdS ratio was increased, as shown in Figure 6-2A. Better dispersion was produced by less CdS particles in the solution. The presence of more CdS particles in the mixture may lead to interactions between the excess anionic AOT (SO_3^-) from the SWNT solution and the positively charged CdS NPs (Cd^{2+}). The intercalation/interaction of CdS dramatically improves the individualization of SWNTs as confirmed by the Raman spectra shown in Figure 6-2B. The low frequency of RBM mode is shifted from 253 cm^{-1} in the SWNT dispersion to 259 cm^{-1} in the SWNT/CdS nanocomposite. The best result is obtained for a SWNT/CdS with a 10:1 w/w ratio of SWNT/CdS. This optimal ratio can presumably be due to the availability of more free space for CdS (ca. 2 nm) to wobble into the bundled tubes and enhance the separation of the aggregated tubes. It can also be deduced that CdS particles are only intercalated with SWNTs since no interacting new peaks appeared in Raman spectra.

Figure 6-3 and Figure 6-4 compare the UV-Vis and Raman spectra of dispersed SWNT, CdS, and the SWNT/CdS nanocomposite. The cartoon in Figure 6-3

schematically illustrates the probable reactions of the SWNT/AOT dispersion with non-surface-modified and surface-modified QDs. After the formation of the composite, SWNTs will not aggregate again after removal of the anionic surfactant AOT from the surface of the tubes. In previous reports, functional groups produced by the acid purification of nanotubes were used to covalently bond QDs with SWNTs [14, 30]. Ozkan et al. have shown the intercalation of SWNT/SDS with core/shell QDs arising from the formation of covalent bonds with sulfonate (SO_3^-) functional groups of the surfactant [20]. In the UV-Vis spectra of the SWNT/CdS composite, clear transition between the van Hove singularities (vHs) for both the metallic first transition ($^{M}E_{11}$, 400-600 nm range) and the semiconducting second transition ($^{S}E_{22}$, 600-800 nm range) are in Figure 6-3. Figure 6-4 shows the Raman spectra where the RBM region of the SWNT/CdS composite shows two new peaks and one additional shoulder indicating the formation of the composite. The peak position of the five peaks can be used to determine the diameter of the SWNTs using the equation: $\nu_{RBM} = (223.5/d_t) + 12.5$. Therefore, the diameters of the peaks labeled a, b, c, d, and e can be calculated as 1.2, 1.1, 0.9, 0.8, and 0.77 nm, respectively. The higher frequency modes correspond to smaller diameter SWNTs. The acoustic mode (M mode) is also observed in the spectra. The M mode represents the overtone of the out-of-plane transverse acoustic mode at about 1750 cm^{-1}. Another new peak corresponding to the in-plane transverse optic mode is also seen (in almost the same location as the disorder band), the longitudinal acoustic mode, iTOLA is located at around 1950 cm^{-1}. Thus, the intercalation/interaction of SWNTs with CdS can improve the separation of bundled nanotubes, and enhance the optical and acoustic properties.

6.4.2 Nanocomposite of SWNTs with thiol-modified CdS

The surface modification of CdS was achieved by replacing the thiol functional group with AOT surfactant. This type of thiol end group (i.e. R-SH) is called stabilizer agents [31, 32], and the thiols can passivate the surface of the CdS particles. The reverse micelle (AOT) encapsulated Cd^{2+}-enriched CdS particles can be modified by thiol (-SH) groups. The surface modification of these particles has been described in detail Chapter 5. However, we have been successful at fabricating SWNT/CdS nanocomposite only with the MPTS and MUA modified CdS particles, as corroborated by spectroscopy experiments. Figure 6-5 shows that the optical and acoustic properties of the nanocomposite are enhanced when CdS-MPTS-OH particles are attached to purified SWNTs. Indeed, the fluorescent signal of acidic p-SWNTs is reduced, and it may cause by neutralized from Cd-MPTS-OH particles. In Figure 6-6A, the composite of CdS-thiol surface-modified NPs and SWNTs does not display any enhancement. In contrast, the composite formed between CdS particles modified by thiol acid stabilizer, CdS-S-$(CH_2)_{10}$-COOH, and p-SWNTs does exhibit enhancement in dispersion, as shown in Figure 6-6B. Therefore, the surface modification of quantum dots with thiol groups leads to better dispersion of p-SWNTs than unpurified SWNTs.

6.4.3 Nanocomposite of SWNTs/poly-L-lysine

Polymeric nanocomposites (PNC) containing SWNTs have been extensively investigated for biomedical applications. The covalent attachment of PLL to SWNTs has been reported in the literature [12]. PLL is commonly used to modify substrates for

stabilizing DNA, and can also be used to wrap around SWNT/surfactant composites [33]. In Figure 6-7A, the nanocomposite of SWNT/PLL displays an impressive enhancement in the acoustic M mode and optical modes of the Raman spectrum [34]. An unusual enhancement of the intermediate frequency modes (IFM) between the RBM and D band in 600 to 1100 cm^{-1} region is also seen due to double resonance process. IFM is a combination of acoustic and optic modes, the details of these modes are beyond the scope of this discussion.

The possible composites of pSWNTs and NPs or polymers are schematically illustrated in Figure 6-7B. The Raman spectrum of the composite displays reduced fluorescence from pSWNTs due to interaction with PLL. PLL also enhances the RBM peaks which indicate the improved individualization of SWNTs. The results show that there is less damage to the side walls of carbon nanotubes when sonication is used instead of refluxing to purify narrow diameter HiPco SWNTs (0.7-1.3nm).

6.5 Conclusion

The remarkable properties of SWNTs make them promising for applications in many different areas. There is a lot of effort being devoted to the use of SWNTs as drug delivery systems [35] and sensing platforms for the detection of cancers [36]. As reported in Chapter 4, the dispersion of SWNTs by AOT adds a protective layer and helps to individualize and dissolve SWNTs. We have used SWNT-AOT dispersions to assemble SWNTs in FET geometries. SWNT-FET may be useful as sensors to detect desirable DNA, RNA, or proteins based on changes in conductance [37].

Here, we report the attachment of poly-L-lysine and QDs to SWNTs. These novel nanocomposites show interesting optical properties and may be useful for biomedical applications.

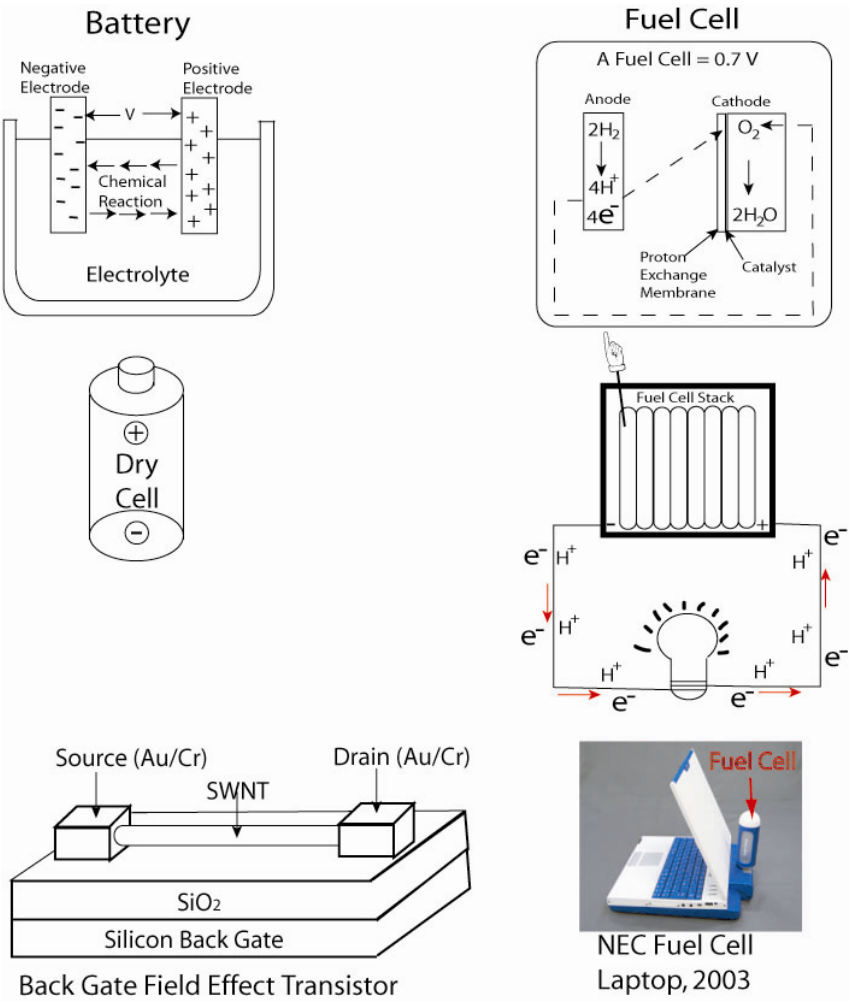

Figure 6-1 Diagram of traditional battery (left/top) vs. Fuel Cell (right/top). A NEC laptop (right/bottom) using a carbon nanotube fuel cell as the power supply. Bottom left, SWNT-FET constructed using Cr/Au source and drain electrodes and a silicon back gate.

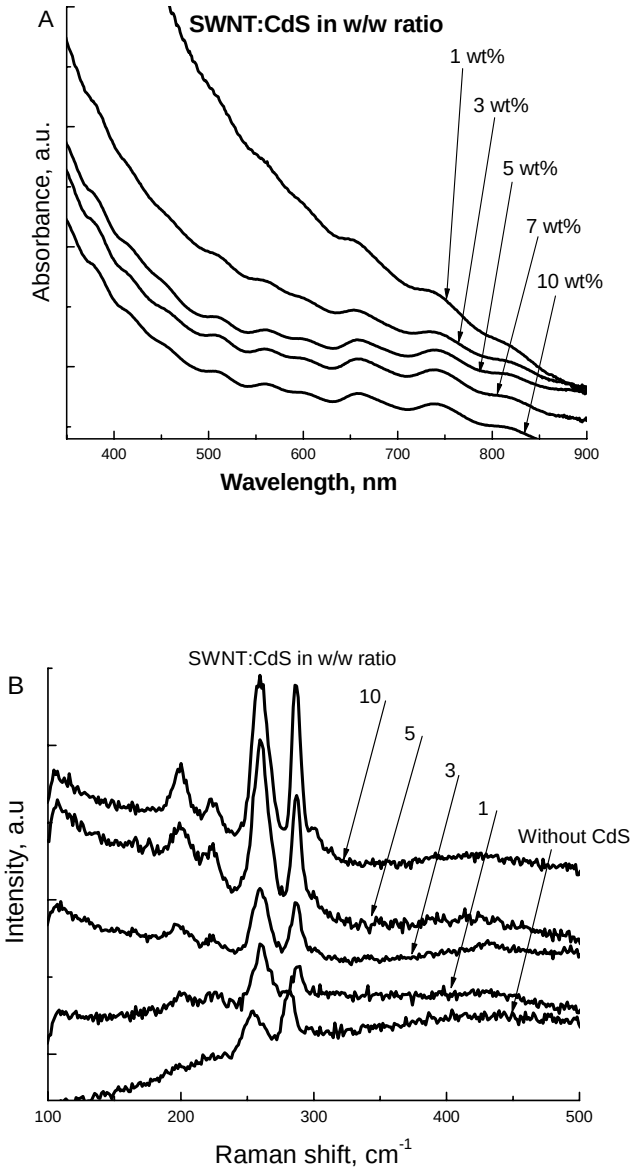

Figure 6-2 Comparison of different w/w ratios of SWNT/CdS composite in UV-Vis (A) and Raman (B) spectra. Concentration of SWNTs is 0.1 mg/mL, and the molar ratio of CdS is $W_o = 2$. In the RBM region of the Raman spectra, the peaks of the composite are shifted from the peaks seen for unfunctionalized SWNTs.

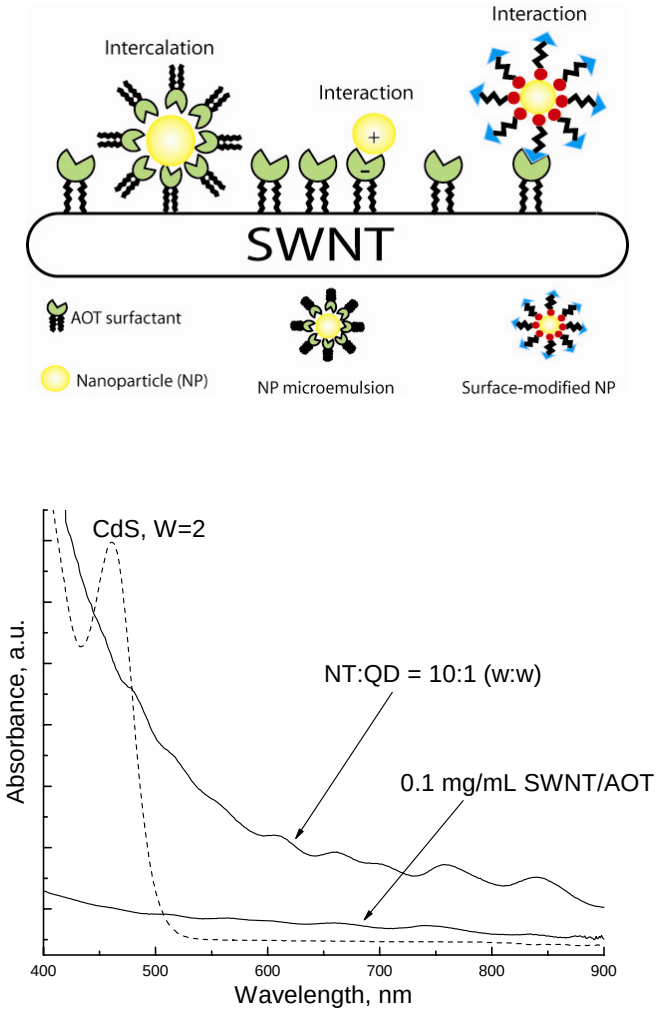

Figure 6-3 Illustration of interaction/intercalation of SWNTs and QDs (Above). (Below) Absorption spectra display the comparison among SWNTs dispersion, CdS particles, and SWNTs/CdS composites.

	a	b	c	d	e
d_t (nm)	1.2	1.1	0.9	0.8	0.77

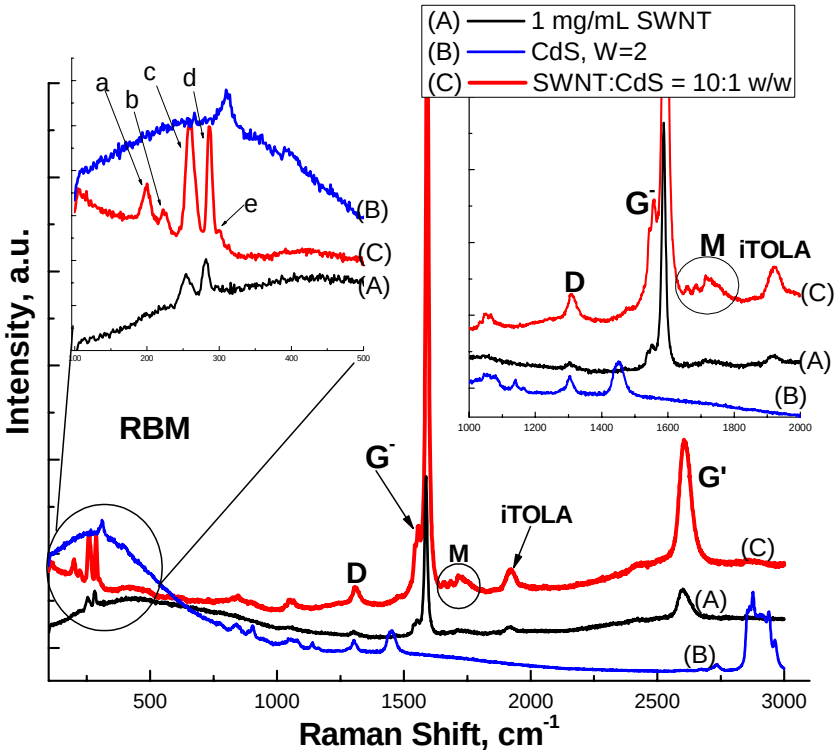

Figure 6-4 Raman spectra of (A) a SWNT dispersion, (B) CdS particles, and (C) SWNT/CdS composites. Insets show spectra of RBM with corresponding diameters (table) and D- /G-band regions.

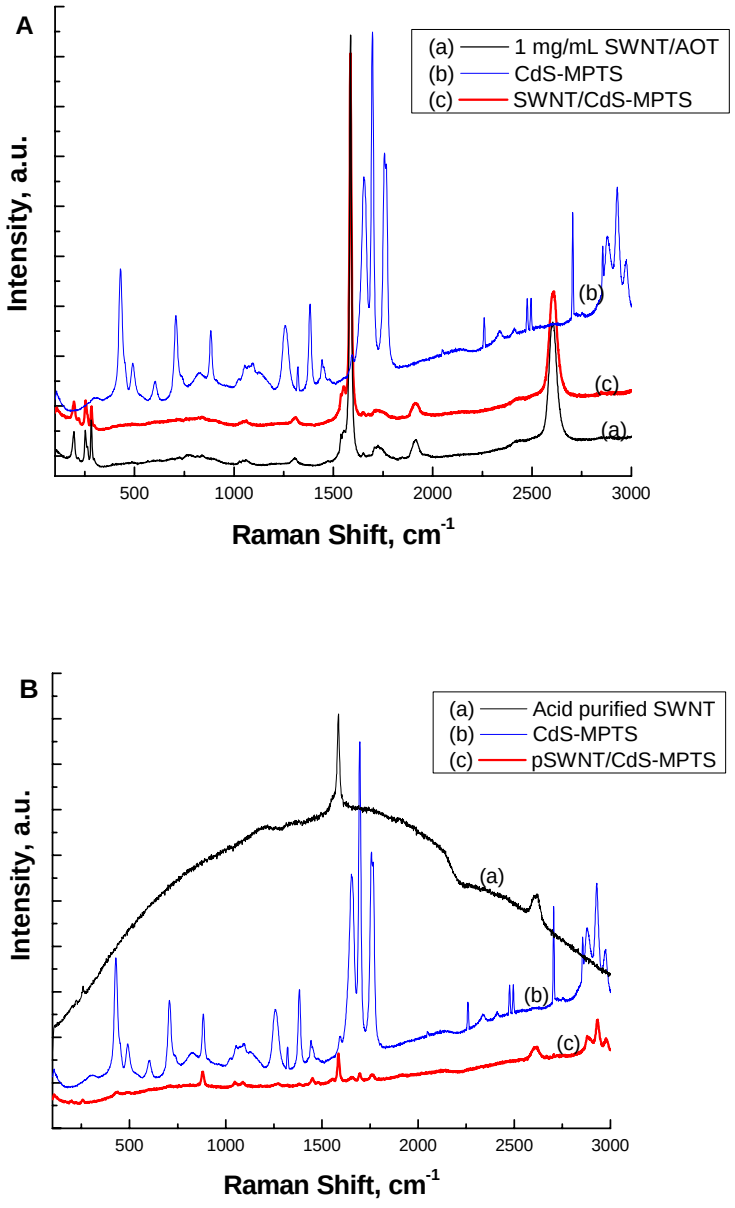

Figure 6-5 Comparison among (a) SWNTs, (b) CdS-MPTS, and (c) SWNT/CdS-MPTS composites, where nanotubes in (A) are as-prepared SWNTs wrapped with AOT, and those in (B) are acid purified SWNTs.

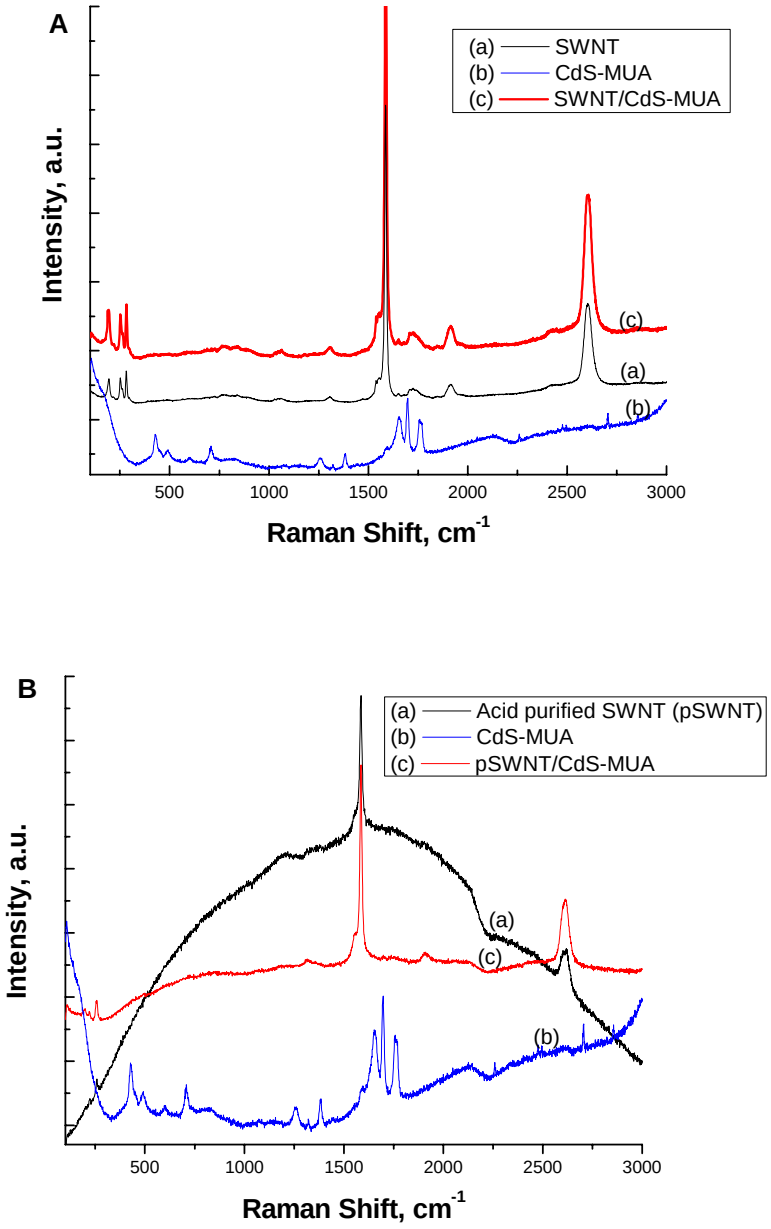

Figure 6-6 Comparison among (a) SWNTs, (b) CdS-MUA, and (c) SWNT/CdS-MUA composites, where nanotubes in (A) are as-prepared SWNTs wrapped with AOT, and those in (B) are acid purified SWNTs.

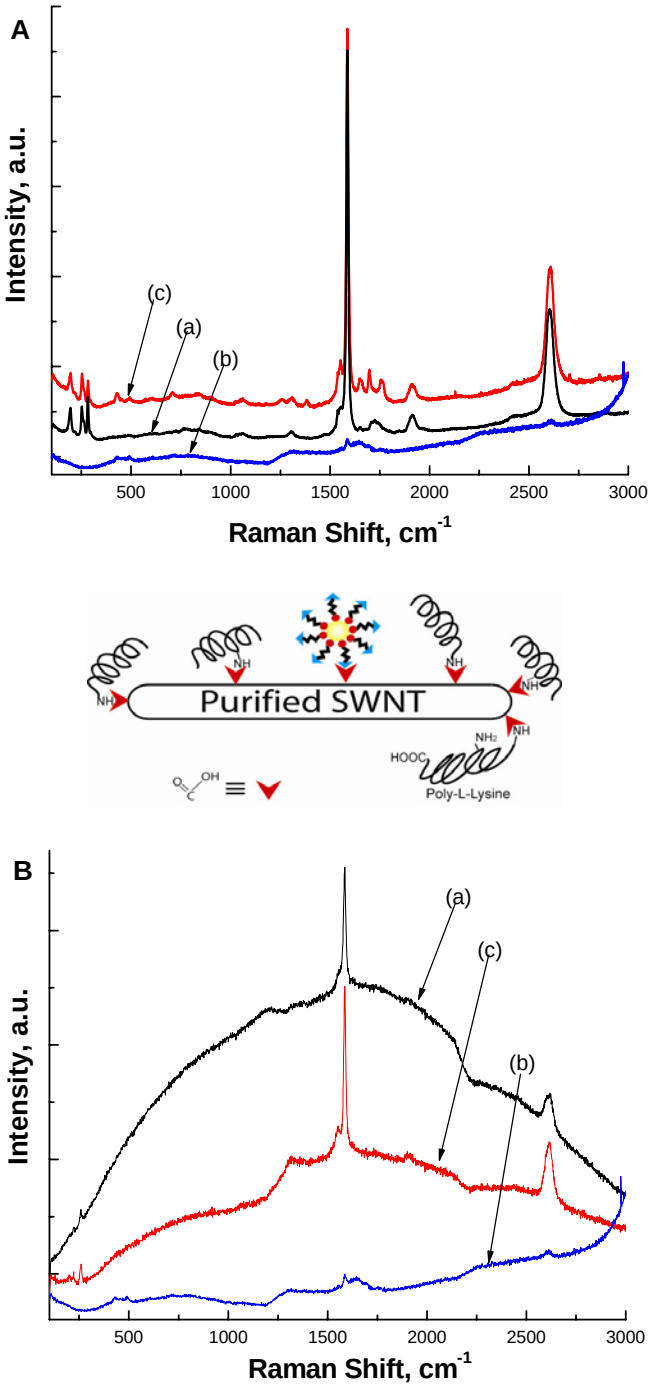

Figure 6-7 Comparison among (a) SWNTs, (b) PLL, and (c) SWNT/PLL composites, where nanotubes in (A) are as-prepared SWNTs wrapped with AOT, and those in (B) are acid purified SWNTs.

References

[1] F. Du, R.C. Scogna, W. Zhou, S. Brand, J.E. Fischer, K.I. Winey, Nanotube Networks in Polymer Nanocomposites: Rheology and Electrical Conductivity, Macromolecules, 37, 9048 (2004).

[2] N. Grossiord, J. Loos, O. Regev, C. E. Koning, Toolbox for Dispersing Carbon Nanotubes into Polymers To Get Conductive Nanocomposites, Chem. Mater., 18, 1089 (2006).

[3] C.A. Dyke, J.M. Tour, Covalent Functionalization of Single-Walled Carbon Nanotubes for Materials Applications, J. Phys. Chem. A, 108, 11151 (2004).

[4] D. Baskaran, J.W. Mays, M.S. Bratcher, Noncovalent and Nonspecific Molecular Interactions of Polymers with Multiwalled Carbon Nanotubes, Chem. Mater., 17, 3389 (2005).

[5] F. Du, J.E. Fischer, K.I. Winey, Effect of Nanotube Alignment on Percolation Conductivity in Carbon Nanotube/Polymer Composites, Phys. Rev. B 72, 121404 R (2005).

[6] K. Mylvaganam, L.C. Zhang, Fabrication and Application of Polymer Composites Comprising Carbon Nanotubes, Recent Patents on Nanotechnology, 1, 59 (2007).

[7] G. Ke, W. Guan, C. Tang, W. Guan, D. Zeng, F. Deng, Covalent Functionalization of Multiwalled Carbon Nanotubes with a Low Molecular Weight Chitosan, Biomacromolecules, ASAP (2007).

[8] A. Nimmagadda, K. Thurston, M.U. Nollert, P.S. McFetridge, Chemical Modification of SWNT Alters in Vitro Cell-SWNT Interactions, J. Biomed. Mat. Res. A, 76A, 614 (2005).

[9] R.A. MacDonald, B.F. Laurenzi, G. Viswanathan, P.M. Ajayan, J.P. Stegemann, Collagen–Carbon Nanotube Composite Materials as Scaffolds in Tissue Engineering, J. Biomed. Mat. Res. A, 74A, 489 (2005).

[10] R.A. Graff, J.P. Swanson, P.W. Barone, S. Baik, D.A. Heller, M.S. Strano, Achieving Individual-Nanotube Dispersion at High Loading in Single-Walled Carbon Nanotube Composites, Adv. Mater. 17, 980 (2005).

[11] M.J. Pender, L.A. Sowards, J.D. Hartgerink, M.O. Stone, R.R. Naik, Peptide-Mediated Formation of Single-Wall Carbon Nanotube Composites, Nano Lett., 6, 40 (2006).

[12] Y. Zhang, J. Li, Y. Shen, M. Wang, J. Li, Poly-L-lysine Functionalization of Single-Walled Carbon Nanotubes, J. Phys. Chem. B, 108, 15343 (2004).

[13] T. Kashiwagi, F. Du, J.F. Douglas, K.I. Winey, R.H. Harris Jr, J.R. Shields, Nanoparticle Networks Reduce the Flammability of Polymer Nanocomposites, Nat. Mater., 4, 928 (2005).

[14] M. Nath, P.V. Teredesai, D.V.S. Muthu, A.K. Sood, C.N.R. Rao, Single-Walled Carbon Nanotubes Intercalated with Semiconductor Nanoparticles. Current Sci., 85, 956 (2003).

[15] S. Banerjee, S.S. Wong, Coating Carbon Nanotubes with Rare Earth Oxide Multiwalled Nanotubes, Adv. Mater., 16, 34 (2004).

[16] L. Fu, Z. Liu, Y. Liu, B. Han, J. Wang, P. Hu, L. Cao, D. Zhu, In-Situ Growth of "Fused", Ozonized Single-Walled Carbon Nanotube - CdTe Quantum Dot Junctions, Adv. Mater., 16, 350 (2004).

[17] S. Banerjee, S.S. Wong, Formation of CdSe Nanocrystals onto Oxidized, Ozonized Single-Walled Carbon Nanotube Surfaces, Chem. Comm., 1866 (2004).

[18] J. Sun, M. Iwasa, L. Gao, Q. Zhang, Single-Walled Carbon Nanotubes Coated with Titania Nanoparticles, Carbon, 42, 893 (2004).

[19] S.C. Wang, H. Yang, D.L. Akins, AOT as Spacing Agent for Single-Walled Carbon Nanotubes Nanocomposite, Polymer Preprints 47, 469 (2006).

[20] S. Chaudhary, J.H. Kim, K.V. Singh, M. Ozkan, Fluorescence Microsocopy Visualization of Single-Walled Carbon Nanotubes Using Semiconductor Nanocrystals, Nano Lett., 4, 2415 (2004).

[21] K.J. Ziegler, Developing Implantable Optical Biosensors, TRENDS in Biotechnology, 23, 440 (2005).

[22] E. Budevski, Structural Aspects of Fuel Cell Electrodes, J. Optoelectronics and Advanced Materials, 5, 1319 (2003).

[23] C. Wang, M. Waje, X. Wang, J.M. Tang, R.C. Haddon, Y. Yan, Proton Exchange Membrane Fuel Cells with Carbon Nanotube Based Electrodes, Nano Lett., 4, 345 (2004).

[24] A. Javey, M. Shim, H. Dai, Electrical Properties and Devices of Large-Diameter Single-Walled Carbon Nanotubes, Appl. Phys. Lett., 80, 1064 (2002).

[25] S. Ghosh, A.K. Sood, N. Kumar, Carbon Nanotube Flow Sensors, Science, 299, 1042 (2003).

[26] R.H. Baughman, C. Cui, A.A. Zakhidov, Z. Iqbal, J.N. Barisci, G.M. Spinks, G.G. Wallace, A. Mazzoldi, D.D Rossi, A.G. Rinzler, O. Jaschinski, S. Roth, M. Kertesz, Carbon Nanotube Actuators, Science, 284, 1340 (1999).

[27] J. Kong, N.R. Franklin, C. Zhou, M.G. Chapline, S. Peng, K. Cho, H. Dai, Nanotube Molecular Wires as Chemical Sensors, Science, 287, 622 (2000).

[28] R.J. Chen, S. Bangsaruntip, K.A. Drouvalakis, N.W.S. Kam, M. Shim, Y.Li, W. Kim, P.J. Utz, H. Dai, Noncovalent Functionalization of Carbon Nanotubes for Highly Specific Electronic Biosensors, PNAS, 100, 4984 (2003).

[29] C.-S. Lee, S.E. Baker, M.S. Marcus, W. Yang, M.A. Eriksson, R.J. Hamers, Electrically Addressable Biomolecular Functionalization of Carbon Nanotube and Carbon Nanofiber Electrodes, Nano Lett., 4, 1713 (2004).

[30] S. Banerjee, S.S. Wong, Synthesis and Characterization of Carbon Nanotube-Nanocrystal Heterostructures, Nano Lett., 2, 195 (2002).

[31] M. Miyake, H. Matsumoto, M. Nishizawa, T. Sakata, H. Mori, S. Kuwabata, H. Yoneyama, Characterization of Covalently Immobilized Q-CdS Particles on Au(111) by Scanning Tunneling Microscopy and Tunneling Spectroscopy with High Reproducibility, Langmuir 13, 742 (1997).

[32] B. Huang, D.A. Tomalia, Dendronization of Gold and CdSe/CdS (Core–Shell) Quantum Dots with Tomalia Type, Thiol Core, Functionalized Poly(Amidoamine) (PAMAM) Dendrons, J. Lumin., 111, 215 (2005).

[33] H. Xin, A. Twoolley, High-Yield DNA-Templated Assembly of Surfactant-Wrapped Carbon Nanotubes, Nanotechnology 16, 2238 (2005).

[34] M.S. Dresselhaus, G. Dresselhaus, R. Saito, A. Jorio, Raman Spectroscopy of Carbon Nanotubes, Physics Reports 409, 47 (2005).

[35] D. Pantarotto, J.-P Briand, M. Prato, A. Bianco, Translocation of Bioactive Peptides Across Cell Membranes by Carbon Nanotubes, Chem. Commun., 16 (2004).

[36] Q. Lu, J.M. Moore, G. Huang, A.S. Mount, A.M. Rao, L.L. Larcom, P.C. Ke, RNA Polymer Translocation with Single-Walled Carbon Nanotubes, Nano Lett., 4, 2473 (2004).

[37] H.-M. So, K. Won, Y.H. Kim, B.-K. Kim, B.H. Ryu, P.S. Na, H. Kim, J.-O Lee, Single-Walled Carbon Nanotube Biosensors Using Aptamers as Molecular Recognition Elements, J. Am. Chem. Soc., 127, 11906 (2005).